

**Galaxy Cluster Studies  
with Weak Lensing Magnification & Shear**

by

JES FORD

B.Sc. Physics, The University of Nevada Reno, 2008

A THESIS SUBMITTED IN PARTIAL FULFILLMENT  
OF THE REQUIREMENTS FOR THE DEGREE OF

**DOCTOR OF PHILOSOPHY**

in

THE FACULTY OF GRADUATE AND POSTDOCTORAL STUDIES  
(Physics)

THE UNIVERSITY OF BRITISH COLUMBIA  
(Vancouver)

August 2015

© JES FORD, 2015

# Abstract

Clusters of galaxies offer a unique window for studying the universe on the largest scales. As the most massive gravitationally bound systems to have formed, they serve as probes of the large scale distributions of dark matter, the underlying cosmology, and the complicated intracluster physics that characterizes the evolution of these massive systems. Gravitational lensing is the deflection of light coming from distant sources, by gravitational potentials along its path. Being sensitive to all mass regardless of type or dynamical state, lensing is a valuable tool for studying dark matter and characterizing galaxy clusters. In the weak lensing regime, the very slight apparent distortion of galaxy shapes is referred to as the shear, while the focusing and amplification of light is referred to as the magnification. The former has become a well-developed and robust technique in astronomy over the past decade, but the latter has been largely overlooked until now.

The work embodied in this thesis includes the first-ever significant detection of magnification by galaxy clusters, and the first comparison between masses measured with weak lensing magnification and shear (Chapter 2). This is followed by an application to an enormous sample of galaxy clusters yielding groundbreaking signal-to-noise for magnification and an analysis of redshift-dependent systematic effects,. This project also provided measurements of the cluster mass-richness scaling relation, and was a milestone in moving from magnification detection to useful science (Chapter 3). Finally, a comprehensive gravitational lensing shear analysis was performed on the previous cluster sample, allowing for a critical comparison between cluster masses measured with the independent techniques, as a function of both richness and redshift. These shear measurements also allowed for important constraints on a new sample of galaxy clusters, including the distribution of cluster centroid offsets, the mass-richness relation, and cluster redshift evolution (Chapter 4).

This thesis details unprecedented measurements using a new technique – weak lensing magnification – and comparisons with the well-studied shear approach. The final product both exemplifies the promise of the new method for measuring galaxy cluster masses, and also points to likely issues that will need to be addressed in future experiments.

Limit of 350 words; is currently at 349.

# Preface

Chapter 2 is an adaptation of a published article – *Magnification by Galaxy Group Dark Matter Halos* by J. Ford, H. Hildebrandt, L. Van Waerbeke, A. Leauthaud, P. Capak, A. Finoguenov, M. Tanaka, M. R. George, and J. Rhodes, published in *The Astrophysical Journal*, Volume 754, Issue 2, article id. 143, 6 pp. (2012). The author of this thesis led the analysis, performed all calculations, wrote all code used in the work, and drafted the published manuscript. H. Hildebrandt and L. Van Waerbeke (thesis advisor) provided regular discussions and guidance that shaped the formulation of the research. A. Leauthaud and P. Capak provided data and astronomical catalogues for analysis. All authors gave comments and edits on the final manuscript.

Chapter 3 is also adapted from published work – *Cluster Magnification and the Mass-Richness Relation in CFHTLenS* by J. Ford, H. Hildebrandt, L. Van Waerbeke, T. Erben, C. Laigle, M. Milkeraitis, and C. B. Morrison, published in *Monthly Notices of the Royal Astronomical Society*, Volume 439, Issue 4, p.3755-3764 (2014). The author of this thesis led the analysis, performed all calculations, wrote or heavily modified all code used in the work, and drafted the published manuscript. H. Hildebrandt and L. Van Waerbeke (thesis advisor) provided regular discussions and guidance that shaped the formulation of the research. T. Erben was heavily involved in producing the CFHTLenS data products used in this work. C. Laigle wrote the first version of the code for calculating cluster richness, which was later adapted by the thesis author for this work. M. Milkeraitis compiled the 3D-Matched-Filter galaxy cluster catalogue which was analyzed. C. B. Morrison performed a study of Lyman-break galaxy low-redshift contamination, upon which this manuscript relied. All authors gave comments and edits on the final manuscript.

Chapter 4 is also adapted from a published article – *CFHTLenS: A Weak Lensing Shear Analysis of the 3D-Matched-Filter Galaxy Clusters* by J. Ford, L. Van Waerbeke, M. Milkeraitis, C. Laigle, H. Hildebrandt, T. Erben, C. Heymans, H. Hoekstra, T. Kitching, Y. Mellier, L. Miller, A. Choi, J. Coupon, L. Fu, M. J. Hudson, K. Kuijken, N. Robertson, B. Rowe, T. Schrabback, and M. Velander, published in *Monthly Notices of the Royal Astronomical Society*, Volume 447, Issue 2, p.1304-1318 (2015). The author of this thesis led the analysis, performed all calculations, wrote or heavily modified all code used in the work, and drafted the published manuscript. The authorship list reflects the lead authors of this paper followed by two alphabetical groups. L. Van Waerbeke (thesis advisor) and H. Hildebrandt provided regular discussions and guidance that shaped the formulation of the research. M. Milkeraitis compiled the 3D-Matched-Filter galaxy cluster catalogue which was analyzed. C. Laigle wrote the first version of the code for calculating cluster richness, which was later adapted by the thesis author for this work. The next group includes key contributors to the science analysis and interpretation in this paper, the founding core team and those whose long-term significant effort produced the final CFHTLenS data product. The final group covers members of the CFHTLenS team who made a significant contribution to the project and/or this paper. All authors gave comments and edits on the final manuscript.

# Table of Contents

<b>Abstract</b>	<b>ii</b>
<b>Preface</b>	<b>iii</b>
<b>Table of Contents</b>	<b>iv</b>
<b>List of Tables</b>	<b>vii</b>
<b>List of Figures</b>	<b>viii</b>
<b>Glossary</b>	<b>ix</b>
<b>1 Introduction</b>	<b>1</b>
1.1 Cosmology	1
1.1.1 Our Universe	1
1.1.2 Dark Matter	3
1.1.3 Dark Energy	3
1.1.4 Cosmic Dynamics	4
1.1.5 Distances in Cosmology	6
1.2 Gravitational Lensing	7
1.2.1 Weak Lensing Shear	9
1.2.2 Weak Lensing Magnification	12
1.2.3 Magnification vs. Shear	14
1.3 Galaxy Clusters	15
1.3.1 Clusters as Cosmological Probes	15
1.3.2 Intracluster Physics	15
1.4 Impact of this Thesis	15
1.5 Thesis Overview	16
<b>2 Magnification by Galaxy Group Dark Matter Halos</b>	<b>17</b>
2.1 Introduction	17
2.2 Theory	18
2.3 Data	19
2.3.1 Lenses	19

2.3.2	Sources . . . . .	20
2.4	Analysis and Results . . . . .	22
2.4.1	Measuring $\alpha(m)$ . . . . .	22
2.4.2	Optimally-Weighted Cross-Correlation . . . . .	22
2.4.3	Halo Mass Profiles . . . . .	23
2.5	Summary and Conclusions . . . . .	24
<b>3</b>	<b>Cluster Magnification and the Mass-Richness Relation in CFHTLenS . . . . .</b>	<b>27</b>
3.1	Introduction . . . . .	27
3.2	Data . . . . .	28
3.2.1	3D-MF Galaxy Clusters . . . . .	28
3.2.2	Sources . . . . .	32
3.3	Magnification Methodology . . . . .	32
3.3.1	The Measurement . . . . .	32
3.3.2	The Modeling . . . . .	33
3.4	Results . . . . .	37
3.4.1	The Mass-Richness Relation . . . . .	39
3.4.2	Redshift Binning . . . . .	42
3.5	Conclusions . . . . .	43
<b>4</b>	<b>CFHTLenS: A Weak Lensing Shear Analysis of the 3D-Matched-Filter Galaxy Clusters . . . . .</b>	<b>45</b>
4.1	Introduction . . . . .	45
4.2	Data . . . . .	46
4.2.1	The Canada-France-Hawaii Telescope Legacy Survey Wide . . . . .	46
4.2.2	CFHTLenS Shear Catalogue . . . . .	47
4.2.3	3D-MF Clusters . . . . .	47
4.3	Method . . . . .	50
4.3.1	Stacking Galaxy Clusters . . . . .	50
4.3.2	Measuring $\Delta\Sigma$ . . . . .	51
4.3.3	Miscentring Formalism . . . . .	53
4.3.4	The Halo Model . . . . .	55
4.4	Galaxy Cluster Weak Lensing Shear Results . . . . .	55
4.4.1	Fits to $\Delta\Sigma$ . . . . .	59
4.4.2	The Mass-Richness Relation . . . . .	60
4.4.3	Results of Binning Clusters in Redshift . . . . .	61
4.5	Discussion . . . . .	63
4.5.1	Interpretation of the Results . . . . .	63
4.5.2	Comparisons of Cluster Catalogue Volume . . . . .	63
4.5.3	Comparison with other Mass-Richness Relations . . . . .	64
4.5.4	Comparisons with other Cluster Centroid Analyses . . . . .	65
4.5.5	Comparison with Magnification Results . . . . .	66
4.6	Conclusions . . . . .	68

<b>5</b>	<b>Conclusions . . . . .</b>	<b>70</b>
5.1	Summary and Conclusions . . . . .	70
5.2	Future Work . . . . .	70
	<b>Bibliography . . . . .</b>	<b>71</b>
<b>A</b>	<b>Supporting Materials . . . . .</b>	<b>82</b>

# List of Tables

Table 1.1	Cosmological Constants . . . . .	6
Table 2.1	Luminosity Function Parameters . . . . .	23
Table 3.1	Centroid Offset Fit Parameters . . . . .	30
Table 3.2	Magnification Results for Richness-Binned Clusters . . . . .	41
Table 3.3	Magnification Results for Redshift-Binned Clusters . . . . .	41
Table 4.1	Shear Results for Richness-Binned Clusters (Full Model) . . . . .	57
Table 4.2	Shear Results for Richness-Binned Clusters (Perfectly Centred Model) . . . . .	57
Table 4.3	Shear Results for Redshift-Binned Clusters (Full Model) . . . . .	58
Table 4.4	Shear Results for Redshift-Binned Clusters (Perfectly Centred Model) . . . . .	58

# List of Figures

Figure 1.1	Gravitational Lensing Diagram . . . . .	8
Figure 1.2	$\kappa$ and $\gamma$ Diagram . . . . .	10
Figure 1.3	Magnification Illustration . . . . .	14
Figure 2.1	Masses and Redshifts of COSMOS Groups . . . . .	20
Figure 2.2	Magnitude-Binned Cross-Correlation . . . . .	21
Figure 2.3	Optimally-Weighted Cross-Correlation . . . . .	25
Figure 3.1	Centroid Offset Model . . . . .	29
Figure 3.2	3D-MF Cluster Richness Distribution . . . . .	31
Figure 3.3	Redshift Distributions of Clusters and Sources . . . . .	35
Figure 3.4	Magnification for all Stacked 3D-MF Clusters . . . . .	37
Figure 3.5	Magnification for Richness-Binned Clusters . . . . .	38
Figure 3.6	Mass-Richness Relation from Magnification . . . . .	39
Figure 3.7	Richness Distributions in Redshift Bins . . . . .	42
Figure 3.8	Magnification for Redshift-Binned Clusters . . . . .	43
Figure 4.1	Mass-Significance Relation . . . . .	48
Figure 4.2	Richness and Redshift Distributions of 3D-MF Clusters . . . . .	49
Figure 4.3	Richness-Significance Scaling . . . . .	50
Figure 4.4	Example of Miscentering Effect on Shear Profile . . . . .	53
Figure 4.5	Shear for Richness-Binned Clusters . . . . .	56
Figure 4.6	Cluster Mass Distributions for each Richness Bin . . . . .	56
Figure 4.7	Mass-Richness Relation from Shear . . . . .	59
Figure 4.8	Shear for Redshift-Binned Clusters . . . . .	60
Figure 4.9	Redshift Dependence of Mass-Richness Normalization . . . . .	62
Figure 4.10	Comparison of Magnification and Shear Masses . . . . .	66



# Glossary

**CFHTLENS** Canada-France-Hawaii-Telescope Lensing Survey

**COSMOS** Cosmological Evolution Survey

**SDSS** Sloan Digital Sky Survey

**MPC** megaparsec

**CMB** Cosmic Microwave Background

**WMAP** Wilkinson Microwave Anisotropy Probe

**WIMP** Weakly Interacting Massive Particle

**COBE** COsmic Background Explorer

**MACHO** MAssive Compact Halo Object

# Chapter 1

## Introduction

This thesis is concerned with weak gravitational lensing studies of galaxy clusters, using two complementary approaches, shear and magnification. This introductory chapter provides the necessary background and context for understanding the novel research presented in the subsequent chapters. The basics of cosmology, which is the larger field within which this thesis research resides, is given in Section 1.1, with a particular focus on distances, which will be important for the presentation of gravitational lensing in Section 1.2. Galaxy clusters are discussed in Section 1.3, from the cosmological as well as the intracluster physics perspective. Section 1.4 outlines the novelty and importance of the research contained in this thesis. A brief overview of the body of work which is presented in the main chapters of this thesis is given in Section 1.5.

### 1.1 Cosmology

Cosmology is the study of our universe as a whole. It can be easy to take for granted the simple fact that we, as scientists, can even do cosmology at all – that is, we can make quantitative and testable predictions about the physical nature of the vast universe we inhabit. At the same time, as we cosmologists forge ahead, caught up in the day-to-day struggles that concern some minute detail of a model, a prediction, or an idea, it is easy to overlook the sheer beauty of what we are so deeply invested in. The introduction of this thesis serves both to lay the requisite theoretical foundation, upon which the thesis research relies, while also giving an honest depiction of the big picture ideas for which this work strives to be relevant.

”The Cosmos is all that is or was or ever will be. Our feeblest contemplations of the Cosmos stir us – there is a tingling in the spine, a catch in the voice, a faint sensation, as if a distant memory, of falling from a height. We know we are approaching the greatest of mysteries” (Sagan, 1980).

#### 1.1.1 Our Universe

Looking out into the night sky from our vantage point on planet earth, the universe appears full of structure on many scales. Planets orbiting stars; stars bound into star clusters and galaxies; galaxies themselves organized into clusters ranging from small associations like our local group, to enormous conglomerates of many thousands of galaxies. But if we adopt a holistic mindset on the scale of around 100 megaparsec (MPC), and ignore the smaller scale density fluctuations which are so crucial to our own existence, we observe two remarkable apparent realities of our universe (Ryden, 2003):

1. **Isotropy.** On large scales, the universe is the same in all locations. There are no special or unique locations.
2. **Homogeneity.** On large scales, the universe is the same in all directions. There are no preferred directions.

These two postulates, which are supported by observations, form the foundation of the current standard cosmological model (Bartelmann and Schneider, 2001).

A third important fact about our universe on large scales, is that it is expanding. Galaxies are moving away from all other galaxies, at a rate proportional to their distance.<sup>1</sup> This simple relationship was discovered by Hubble (1929), and can be expressed as

$$v \approx H_0 r, \quad (1.1)$$

where  $v$  is recessional velocity,  $r$  is distance, and  $H_0$  is known as the Hubble constant (Ryden, 2003). Our current best estimate is  $H_0 = 67.8 \pm 0.77$  km/s/Mpc (Planck Collaboration et al., 2014); this and other cosmological constants are listed in Table 1.1. The discovery of the expansion of the universe simultaneously abolished any notion that our universe was static, while also giving rise to the idea of a Big Bang origin. Extrapolating back in time, it seems that the universe was once much smaller, denser, and hotter.

Several pieces of evidence, including the remarkable success of Cosmic Microwave Background (CMB) experiments such as the COsmic Background Explorer (COBE) (Fixsen et al., 1996), the Wilkinson Microwave Anisotropy Probe (WMAP) (Hinshaw et al., 2013) and Planck (Planck Collaboration et al., 2014), provide very strong support for the Big Bang theory. First detected by Penzias and Wilson (1965), the CMB is an isotropic background of microwave photons that have been essentially free-streaming since the universe was a dense opaque cloud. At around 380,000 years of age, the density had dropped sufficiently, and the universe had cooled enough for neutral atoms to form, freeing the photons from constant Thomson scattering. The CMB photons match a blackbody spectrum with temperature  $2.73K$  and have a number density of  $4.11 \times 10^8/m^3$ . The tiny fluctuations in CMB temperature on the sky, which are of order 1 part in  $10^5$ , are the seeds of structure formation in the universe (Ryden, 2003). Measurements of these anisotropies by WMAP and Planck have provided cosmological parameter constraints of incredible precision (see Table 1.1).

One consequence of the expansion of the universe (and also the way it was first discovered) is that light from distant objects is redshifted as it travels to us. This shifts the spectrum of light emitted by galaxies, so that known absorption lines will appear at different wavelengths than they are observed in laboratories on earth. This cosmological redshift can be expressed in terms of the observed and the emitted wavelengths (Ryden, 2003):

$$z \equiv \frac{\lambda_{\text{obs}} - \lambda_{\text{em}}}{\lambda_{\text{em}}}. \quad (1.2)$$

Redshift is often a convenient means of indicating cosmological distances, and will be used frequently throughout this thesis. Since the universe is expanding, it is convenient to express its growth in terms of a scale factor  $a(t)$ . We define  $a$  to be unity today ( $a(t_0) = 1$ ), and say that  $a(t) < 1$  in the past. In this framework we can directly convert the cosmological redshift of an object to the scale factor when its light was emitted (Ryden, 2003):

$$1 + z = \frac{a(t_0)}{a(t_e)} = \frac{1}{a(t_e)}. \quad (1.3)$$

---

<sup>1</sup>Note: the linear Hubble relation only holds for relatively small cosmic distances, below a few hundred MPC (Ryden, 2003).

The expansion history, given by the scale factor  $a(t)$ , depends upon the constituents of the energy density of the universe. Numerous studies show that, in addition to obvious stuff like normal matter<sup>2</sup> and radiation, the universe also contains copious amounts of cold dark matter and some form of dark energy, possibly a cosmological constant (Dodelson, 2003). These components will be discussed in more detail below. This dark sector actually makes up the majority of the present energy density of the universe, but that was not always the case because of the way the density of each component evolves differently with the scale factor.

### 1.1.2 Dark Matter

The notion of an invisible dark matter has been around for a surprisingly long time. The idea was first proposed by Zwicky (1933) to explain the fact that the mass of the Coma Cluster estimated from radial velocities of member galaxies greatly exceeded the mass estimated from luminosity (see also Zwicky, 1937). Several years later a similar mismatch was observed between the rotation curves of individual galaxies and the amount of visible matter they contained (Babcock, 1939), indicating that an enormous amount of invisible mass must extend far beyond the visible range of the galaxies. This gave rise to the concept of the dark matter halo, a much larger spherical halo of invisible dark matter existing around every galaxy and galaxy cluster (see van den Bergh, 1999, for a review of dark matter’s discovery).

Current measurements confirm the existence of dark matter, refining its abundance to around 30% of the energy content of the entire universe – an order of magnitude greater average density than ordinary matter. For much of the latter part of the 20th century it was thought that the dark matter could simply be normal matter that was not giving off light. Faint stars, brown dwarfs, black holes, rocky bodies, and an abundance of light weight neutrinos, were all candidates for the non-luminous material (van den Bergh, 1999). The now mainstream idea of a non-baryonic cold dark matter was first introduced in 1983 by Bond et al. at the Third Moriond Astrophysics Meeting Audouze and Tran Thanh Van (1984). Cold dark matter is supported by requirements for structure formation in the universe (Bartelmann and Schneider, 2001), as well as more “direct” evidence of the non-interaction of dark matter studied in several merging galaxy cluster systems, including the well-known Bullet Cluster (Clowe et al., 2006).

Dark matter seems to interact only through gravity, and certainly not via the electromagnetic force (it does not emit, absorb, or reflect light). The most plausible contender for the actual dark matter particle is called a Weakly Interacting Massive Particle (WIMP), which, as the name implies, is a massive particle that interacts only through gravity and the weak nuclear force. Common supersymmetric extensions to the Standard Model of particle physics include particles that could be candidates for WIMPs (Dodelson, 2003). Unfortunately, direct detection of these particles has proved extremely difficult, despite the fact that numerous groups are pursuing detection using a variety of approaches. One group has claimed a WIMP detection (this is the DAMA/LIBRA experiment which has observed an annual signal modulation), but it remains controversial and seems to be ruled out by other experiments (particularly the XENON-100 experiment) (Cushman et al., 2013).

### 1.1.3 Dark Energy

Probably the biggest mystery in all of physics is the nature of dark energy. Like dark matter, the idea has been around for many decades, but unlike dark matter it was not initially based upon observations, but rather

---

<sup>2</sup>Normal matter consists of atoms and other standard model particles, which, in cosmology, are typically all lumped together under the label “baryonic matter” despite the fact that they are not all strictly baryons in the particle physics sense (Ryden, 2003).

a preconceived bias. Since this was before Hubble had discovered the expansion of space, Einstein (and many others) assumed the universe was static. But a matter dominated universe described by Einstein's theory of relativity couldn't be static – it would contract and fall back on itself due to the gravitational potential of all the mass in it (Ryden, 2003).

Einstein added a term to his field equations known as the cosmological constant, which was supposed to be a repulsive term that perfectly balanced the universe against gravitational collapse. These equations described how the geometry (left-hand-side) was related to the energy content (right-hand-side) of the universe:

$$R_{\mu\nu} - \frac{1}{2}g_{\mu\nu}R = -\frac{8\pi G}{c^4}T_{\mu\nu} + \Lambda g_{\mu\nu} \quad (1.4)$$

Here  $R_{\mu\nu}$  and  $R$  are the Ricci tensor and scalar.  $G$  is Newton's gravitational constant and  $c$  is the speed of light in a vacuum. The metric tensor is given by  $g_{\mu\nu}$ , and the energy-momentum tensor is  $T_{\mu\nu}$  (Bertone et al., 2005). When the Hubble expansion was discovered, Einstein famously abandoned the cosmological constant term,  $\Lambda g_{\mu\nu}$ , but it has since reappeared (Ryden, 2003).

In the late 1990s, two teams of astronomers were trying to measure the deceleration of the universe, since the current expansion was expected to be slowing under the gravitational attraction of all the matter. Both the High- $z$  Supernovae Search Team (Riess et al., 1998) and the Supernovae Cosmology Project (Perlmutter et al., 1999) used type Ia supernovae as standard candles, relating the peak luminosity to the width of the light-curve, and found evidence for a non-zero cosmological constant. The universe's expansion was actually accelerating. This nobel-prize-winning discovery has been a paradigm shift for the field of cosmology.

The name dark energy refers to the unknown force causing the universe to accelerate. The simplest possibility would be a cosmological constant, perhaps a vacuum energy that is uniform throughout space.<sup>3</sup> Other more complicated theories have been invented to explain the acceleration, so dark energy is the more general term encompassing them all, but currently the data are consistent with a cosmological constant making up almost 70% of the energy-density of the universe (Planck Collaboration et al., 2014).

### 1.1.4 Cosmic Dynamics

General Relativity stipulates that space and time are part of a single fabric, known as space-time. Events separated in this 4-dimension space-time can be described using the Robertson-Walker metric. This particular form of the metric is a direct consequence of the assumptions of homogeneity and isotropy of the universe (Bertone et al., 2005):

$$ds^2 = -c^2 dt^2 + a(t)^2 [dr^2 + S_k(r)^2 d\Omega^2]. \quad (1.5)$$

Here  $dt$  is an interval of proper time,  $d\Omega^2 = d\theta^2 + \sin^2\theta d\phi^2$ , and  $(r, \theta, \phi)$  are the set of comoving position coordinates (comoving coordinates grow along with the Hubble expansion – see Section 1.1.5).

The  $S_k(r)$  term is specified by the curvature of the universe, which can be *flat* (zero curvature, Euclidean), *closed* (positively curved, analogous to the surface of a sphere in 2-dimensions), or *open* (negatively curved, like

---

<sup>3</sup>Unfortunately, calculating the expected energy density of the vacuum from particle physics gives a value 124 orders of magnitude higher than observed. This is a major unsolved issue in theoretical physics and cosmology (Ryden, 2003).

the surface of a saddle in 2-dimensions). Explicitly,

$$S_k(r) = \begin{cases} \mathcal{R}\sin(r/\mathcal{R}), & \text{for positive curvature} \\ r, & \text{for zero curvature} \\ \mathcal{R}\sinh(r/\mathcal{R}), & \text{for negative curvature.} \end{cases} \quad (1.6)$$

If curvature is non-zero, then  $\mathcal{R}$  gives the radius of curvature (Ryden, 2003). Strong limits have been placed on curvature, and it turns out our universe is flat, or extremely close to flat. The fraction of the energy density of the universe contained in curvature is less than about one part in 1000 and is consistent with zero (Planck Collaboration et al., 2014).

Applying the Robertson-Walker metric (Equation 1.5) to the Einstein field equations (Equation 1.4), we obtain the Friedmann Equation:

$$\left(\frac{\dot{a}}{a}\right)^2 = \frac{8\pi G}{3}\rho_{\text{total}}. \quad (1.7)$$

Here  $a = a(t)$  is the scale factor, and  $\dot{a}$  is its first order derivative with respect to time. The total energy density of the universe  $\rho_{\text{total}}$  appears to be equal to the critical energy density  $\rho_{\text{crit}}$ , which is exactly the case if the universe has zero curvature. The critical density is given by (Dodelson, 2003):

$$\rho_{\text{crit}} \equiv \frac{3H_0^2}{8\pi G} \approx 1.88h^2 \times 10^{-29} \frac{\text{g}}{\text{cm}^3}. \quad (1.8)$$

Cosmologists frequently express the density of each component of the universe as a fraction of the total or critical energy density, using the notation  $\Omega_i = \rho_i/\rho_{\text{crit}}$ .  $\Omega_\Lambda$  represents dark energy,  $\Omega_c$  is the cold dark matter,  $\Omega_b$  is the baryonic matter, and  $\Omega_r$  is for radiation. Since the universe is flat  $\sum \Omega_i = \Omega_\Lambda + \Omega_c + \Omega_b + \Omega_r = 1$ . Each of these components evolves differently with the scale factor (i.e. with time, or redshift). The present values of these density parameters are given in Table 1.1, along with other cosmological constants relevant to this thesis.

The evolution of matter (both normal matter and dark matter) is the most intuitive, as its energy density is simply inversely proportional to the volume of space,  $\rho_m(t) \propto a(t)^{-3} = (1+z)^3$ . The energy density of radiation (massless particles such as photons) scales as  $\rho_r(t) \propto a(t)^{-4} = (1+z)^4$  because the energy of the particles drops off as the cosmological expansion increases their wavelength, yielding an extra factor of  $a(t)^{-1}$  over the case for matter. Dark energy appears to be consistent with a cosmological constant, which, as the name implies, would have constant energy density  $\rho_\Lambda \propto a(t)^0 = (1+z)^0$ .

It is useful to introduce the Hubble rate  $H(t) \equiv \dot{a}/a$ , which, at the present time  $t_0$ , is equal to the Hubble constant  $H_0$ . Thus we can re-write the Friedmann Equation, describing the evolution of the universe, in this form:

$$H(z)^2 = H_0^2 [\Omega_\Lambda + \Omega_m(1+z)^3 + \Omega_r(1+z)^4]. \quad (1.9)$$

The curvature term, which is so close to zero to be negligible, is ignored.<sup>4</sup> In weak lensing, it is usually practical to ignore  $\Omega_r$  as well, and approximate the universe as being flat and composed of only matter and a cosmological constant. That will be the case in most of this thesis, and we will use the matter density  $\Omega_m \approx \Omega_c + \Omega_b$ , absorbing the tiny fraction of the universe's baryon fraction into the cold dark matter term, and use a single term for the fractional energy density that is contributed by matter,  $\Omega_m$ .

<sup>4</sup>If included, the curvature term would scale proportionally to  $(1+z)^2$ .

Symbol	Value	Description
$\Omega_b h^2$	$0.02205 \pm 0.00028$	Fraction of the present day energy density of the universe that is composed of baryons (times $h^2$ ).
$\Omega_c h^2$	$0.1199 \pm 0.0027$	Fraction of the present day energy density of the universe that is composed of cold dark matter (times $h^2$ ).
$\tau$	$0.089^{+0.012}_{-0.014}$	Optical depth due to reionization.
$n_s$	$0.9603 \pm 0.0073$	Scalar spectrum power-law index.
$\ln(10^{10} A_s)$	$3.089^{+0.024}_{-0.027}$	Log power of the primordial curvature perturbations.
$100\theta_{MC}$	$1.04131 \pm 0.00063$	$\theta_{MC} \approx \theta_*$ , the ratio of the comoving size of the sound horizon at $\tau = 1$ to the angular diameter distance of the redshift at $\tau = 1$ .
$H_0$	$67.3 \pm 1.2$ km/s/Mpc	Present day value of the Hubble constant, the ratio of recessional velocity to distance.
$\Omega_m$	$0.315^{+0.016}_{-0.018}$	Fraction of the present day energy density of the universe that is composed of pressureless matter.
$\Omega_\Lambda$	$0.685^{+0.018}_{-0.016}$	Fraction of the present day energy density of the universe that is composed of dark energy.
$\sigma_8$	$0.829 \pm 0.012$	Normalization of the matter power spectrum.
$t_0$	$13.817 \pm 0.048$ Gyr	The age of the universe.

**Table 1.1:** Current best values of the Cosmological Constants using a combination of CMB data from the Planck and WMAP missions (Planck Collaboration et al., 2014). It is quite remarkable that our entire model for the current state and evolution of the universe can be fully encapsulated by a mere 6 parameters – the top 6 rows. The constants in the lower portion of the table are derived from these top 6 values, and are more relevant for the topics explored in this thesis. *Note:* The dimensionless Hubble parameter “little  $h$ ” is just the Hubble Constant in units of 100 km/s/Mpc.  $h \approx 0.7$  is used throughout this thesis.

### 1.1.5 Distances in Cosmology

Describing distances between objects in an expanding and accelerating universe is no simple task. Since physical distances are growing with the universe’s expansion, a natural coordinate system to use is that of comoving coordinates, which grow along with the universe. The *comoving distance* between two galaxies is a constant, as long as they have no velocity relative to the Hubble expansion, while the physical distance between them grows. This physical distance is usually called the *proper distance*, and is simply given by

$$d_p(t) = a(t)r, \quad (1.10)$$

where  $r$  is the comoving radial distance, the same  $r$  used in the Robertson-Walker metric (Equation 1.5) (Ryden, 2003). Since actually measuring a cosmological scale proper distance would require us to pause the universe’s expansion while we extend an enormous tape measurer, we have to rely on other forms of distance, discussed below.

Frequently we want to relate the apparent brightness of a distant astronomical object to its distance. This is especially crucial for objects of known intrinsic luminosity (often called standard candles), such as the type Ia supernovae discussed in Section 1.1.3. For everyday distances here on Earth, we observe that the flux  $f$  of an object with luminosity  $L$  falls off as  $1/(\text{distance})^2$ . We can therefore define an analogous *luminosity distance* in

cosmology as

$$d_L \equiv \sqrt{\frac{L}{4\pi f}}, \quad (1.11)$$

with the understanding that this is different than proper or comoving distance because the universe has been expanding during the time it took for the light to travel to us. In fact, this implies the relationship

$$d_L = (1+z)r = (1+z)d_p(t_0). \quad (1.12)$$

Similar to the notion of a standard candle, we can imagine a standard ruler of a fixed physical length  $\ell$ . We can define the *angular diameter distance* to be the distance at which this object would have to be, in order to conform to our everyday experience of the relationship between distance, length, and angle subtended ( $\theta$  [radians]):

$$d_A \equiv \frac{\ell}{\theta}. \quad (1.13)$$

Here we have invoked the small angle approximation, and the angular diameter distance  $d_A$  is simply related to the other distance definitions (Ryden, 2003):

$$d_A = \frac{r}{(1+z)} = \frac{d_L}{(1+z)^2}. \quad (1.14)$$

Angular diameter distance is the distance measure relevant for gravitational lensing, which will be discussed in Section 1.2.

## 1.2 Gravitational Lensing

As light from distance objects in the universe makes the journey from its source to our telescopes, it is deflected by mass inhomogeneities along its path. In particular, large overdensities, such as galaxies and galaxy clusters, will cause light rays to be bent and focused, altering the images of the background objects. Einstein's theory of General Relativity predicts this effect, and specifically requires the angle of deflection to be twice that of in Newtonian gravity. During a solar eclipse in 1919, Sir Arthur Eddington measured the shifted apparent positions of stars being gravitationally lensed by the sun, providing experimental evidence for the new theory of gravity and paving the way for the future of gravitational lensing as a field (Bartelmann and Schneider, 2001).

The lensing geometry is displayed (not to scale) in Figure 1.1. For most lensing studies the distances between astronomical objects involved is far greater than the size of the gravitational lens itself. It is therefore reasonable to approximate the path of the light ray as being bent at a sharp angle (as opposed to gradually arcing through the gravitational potential) (Bartelmann and Schneider, 2001). In analogy to refraction of light by an optical lens, this is known as the “thin lens approximation.” When light passes nearby an object of mass  $M$ , at impact parameter  $b$ , its path will be bent by the angle  $\hat{\alpha}_L$  (Ryden, 2003):<sup>5</sup>

$$\hat{\alpha}_L = \frac{4GM}{c^2 b}. \quad (1.15)$$

This causes the background light source to appear as if it is at an angle  $\theta$ , when it is really at angular position

---

<sup>5</sup>Note that this thesis uses a similar notation to lensing reviews such as Bartelmann and Schneider (2001) and Schneider (2006b), but we add the subscript “L” to some symbols in this chapter, pertaining to the lensing equations, to avoid confusion with the use of the same symbols in later sections of the thesis (e.g.  $\beta$  will be the slope of the cluster mass-richness relation in Chapter 3 and Chapter 4).



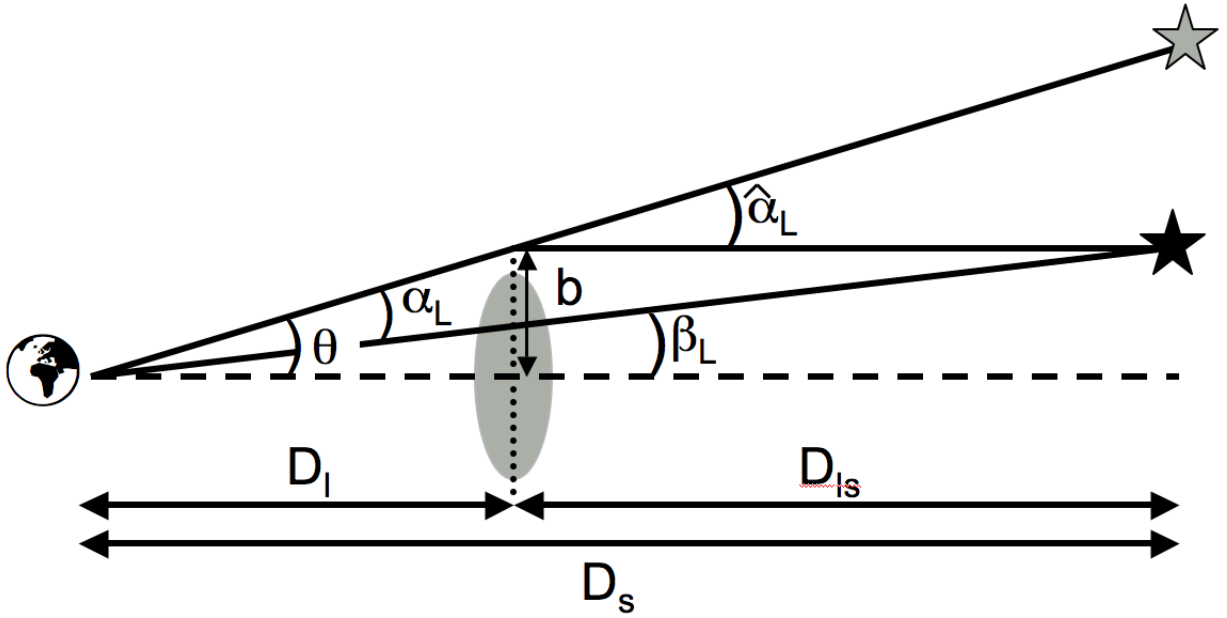


**Figure 1.1:** Diagram showing the geometry of gravitational lensing. Light from the background source is bent by an angle  $\hat{\alpha}_L$  when it passes near the gravitational lens (gray oval) on its way to the earth. While the actual source (black star) is at an angle  $\beta_L$  relative to the horizontal, its image (gray star) appears to be at an angle  $\theta$ . The angular diameter distances to the lens ( $D_l$ ), to the source ( $D_s$ ) and between the lens and source ( $D_{ls}$ ) are labeled.

$\beta_L$ , as shown in Figure 1.1.

The fact that gravitational lensing directly probes the underlying density field along the line of sight is what makes the technique extremely valuable. All other methods for probing the matter distribution of the universe do not probe the mass itself (which is mostly dark matter), but rather the baryonic component of the mass – stars, and interstellar gas and dust. While we expect the baryons to trace the underlying density of dark matter, there are many complicating factors (see Section 1.3) that render the analogy lacking. Additionally, other means of measuring masses (such as using radial velocities) rely on assumptions about the virial equilibrium of a system which may not be satisfied.

Gravitational lensing is broadly divided into several branches depending upon the strength of the lensing effect. Strong lensing refers to the rarest and most obvious distortions, leading to images of giant arcs, Einstein rings, and multiple images of the same source. Strong lensing features are generally apparent to the eye, whereas weak lensing and microlensing are not. The first observation of gravitational lensing producing multiple images was made by Walsh et al. (1979) using a lensed quasar. The first gravitationally lensed arcs were discovered nearly a decade later by Lynds and Petrosian (1986) and Soucaill et al. (1987, 1988). Currently, over one hundred strong gravitational lenses are known (Browne et al., 2003; Bolton et al., 2008). Strong lensing is very useful for accurately probing the dark matter halo mass profiles of galaxies and clusters of galaxies, often yielding detailed information on lens concentration (Auger et al., 2010) and substructure (Mao and Schneider, 1998; Dalal and Kochanek, 2002).

Weak lensing, just as the name implies, leads to much less significant distortions. The hallmark of weak lensing is that it is a statistical effect, only measurable using ensembles of many background sources and foreground lenses. Unlike the rarity of a strong lensing event, however, weak lensing is everywhere. Essentially all

light rays are distorted at least a bit while traveling to us through the inhomogeneous gravitational fields of the universe. Weak lensing itself, and different methods of measuring it, will be discussed in much more detail in Section 1.2.1 and Section 1.2.2 below.

Finally, microlensing is the even weaker signature of gravitational lensing, wherein stars are lensed by low mass compact objects like black holes, brown dwarfs, and planets. Probably the most important use of microlensing has been the search for a significant MAssive Compact Halo Object (MACHO) population in the Milky Way. MACHOs were once considered a serious dark matter candidate until various microlensing experiments demonstrated that the mass density of MACHOs was strongly insufficient to explain the missing mass in our galaxy (Paczynski, 1996; Wyrzykowski et al., 2011; Sumi et al., 2013).

### 1.2.1 Weak Lensing Shear

Weak lensing shear is the component of weak lensing that deals with shape distortion of galaxy images. If all galaxies were intrinsically circular, or of known shape, then each individual background source would provide information on the gravitational field through which its light had propagated. Instead, however, galaxies take on a variety of shapes and orientations, and their unlensed representations are impossible to know. In order to proceed, weak lensing astronomers make two critical assumptions: (1) galaxy shapes can be approximated as elliptical, and (2) the orientation of these ellipses are random in the absence of gravitational lensing (Bartelmann and Schneider, 2001). The second point follows from the isotropy of the universe. Though only a few percent effect, characterization of these intrinsic alignments is an active area of research (see e.g. Hirata and Seljak, 2004; Heymans et al., 2013).

As illustrated in Figure 1.1, the lens equation is given by

$$\boldsymbol{\beta}_L = \boldsymbol{\theta} - \boldsymbol{\alpha}_L, \quad (1.16)$$

where we now use bold face to indicate angular positions with two components on the sky. The reduced deflection angle  $\boldsymbol{\alpha}_L$  is related to the deflection angle of Equation 1.15 by  $\boldsymbol{\alpha}_L = (D_{ls}/D_s)\hat{\boldsymbol{\alpha}}_L$ . The reduced deflection angle  $\boldsymbol{\alpha}_L$  can be expressed as the gradient of the lensing (or deflection) potential  $\boldsymbol{\alpha}_L = \nabla\psi$ . The lensing potential  $\psi(\boldsymbol{\theta})$  is the two-dimensional analogue to the Newtonian gravitational potential  $\Phi$ , and is given by (Narayan and Bartelmann, 1996):

$$\psi(\boldsymbol{\theta}) = \frac{2}{c^2} \frac{D_{ls}}{D_l D_s} \int \Phi(D_l \boldsymbol{\theta}, z) dz = \frac{1}{\pi} \int_{\mathbb{R}^2} \kappa(\boldsymbol{\theta}') \ln|\boldsymbol{\theta} - \boldsymbol{\theta}'| d^2\theta'. \quad (1.17)$$

Here  $\kappa$  is known as the convergence, which encapsulates the magnification information to be described in Section 1.2.2 below. Explicitly, the convergence is given by

$$\kappa(\boldsymbol{\theta}) = \frac{1}{2} \left( \frac{\partial^2 \psi(\boldsymbol{\theta})}{\partial \theta_1^2} + \frac{\partial^2 \psi(\boldsymbol{\theta})}{\partial \theta_2^2} \right), \quad (1.18)$$

and another useful expression is the ratio

$$\kappa(\boldsymbol{\theta}) = \frac{\Sigma(\boldsymbol{\theta})}{\Sigma_{\text{crit}}}. \quad (1.19)$$

Here  $\Sigma(\boldsymbol{\theta})$  is the two-dimensional surface mass density (with units of mass per area on the sky), and  $\Sigma_{\text{crit}}$  is the critical surface mass density of the lens (Wright and Brainerd, 2000). The latter demarcates the separation

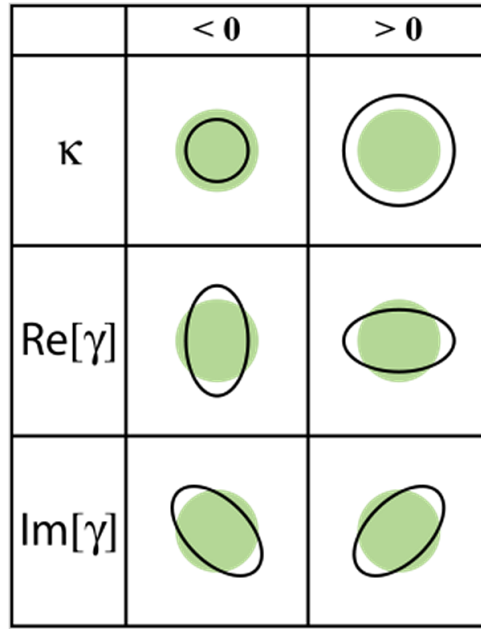


**Figure 1.2:** Demonstration of the effect of convergence  $\kappa$  and shear  $\gamma$  on a circular source. Diagram shows the unlensed source (green circle) and the final lensed image (black outline) for positive and negative values of both  $\kappa$  and the real and imaginary components of  $\gamma$ . [Source: TallJimbo/Wikimedia Commons/CC-BY-SA-3.0].

between strong and weak gravitational lenses, depending critically on the geometry of the angular diameter distances between objects, given by

$$\Sigma_{\text{crit}} = \frac{c^2}{4\pi G} \frac{D_s}{D_l D_{ls}}. \quad (1.20)$$

Strong lenses (i.e. capable of forming multiple images) must have  $\Sigma \geq \Sigma_{\text{crit}}$  (Schneider, 2006a).

The transformation of background objects from source (unlensed) to image (lensed) is described by the Jacobian (or amplification) matrix  $\mathcal{A}$  (Dodelson, 2003):

$$\mathcal{A}(\boldsymbol{\theta}) = \frac{\partial \boldsymbol{\beta}_L}{\partial \boldsymbol{\theta}} = \left( \delta_{ij} - \frac{\partial^2 \psi(\boldsymbol{\theta})}{\partial \theta_i \partial \theta_j} \right) = \begin{pmatrix} 1 - \kappa - \gamma_1 & -\gamma_2 \\ -\gamma_2 & 1 - \kappa + \gamma_1 \end{pmatrix}. \quad (1.21)$$

The two components of the shear  $\gamma(\boldsymbol{\theta})$  can be expressed as derivatives of the lensing potential:

$$\gamma_1 = \frac{1}{2} \left( \frac{\partial^2 \psi(\boldsymbol{\theta})}{\partial \theta_1^2} - \frac{\partial^2 \psi(\boldsymbol{\theta})}{\partial \theta_2^2} \right), \quad (1.22)$$

$$\gamma_2 = \frac{\partial^2 \psi(\boldsymbol{\theta})}{\partial \theta_1 \partial \theta_2}. \quad (1.23)$$

The shear is often written as a complex number,  $\gamma \equiv \gamma_1 + i\gamma_2 = |\gamma|e^{2i\varphi}$ . Here  $|\gamma|$  and  $\varphi$  indicate the amplitude and direction of distortion, respectively, which is unchanged when rotated by  $180^\circ$ .

We do not observe the true shear, but rather the reduced shear  $g(\boldsymbol{\theta}) = \gamma(\boldsymbol{\theta}) [1 - \kappa(\boldsymbol{\theta})]^{-1}$ . We can thus rewrite

the Jacobian matrix as:

$$\mathcal{A}(\boldsymbol{\theta}) = (1 - \kappa) \begin{pmatrix} 1 - g_1 & -g_2 \\ -g_2 & 1 + g_1 \end{pmatrix}. \quad (1.24)$$

In the regime of weak lensing, the convergence and shear are small,  $\kappa \ll 1$  and  $|\gamma| \ll 1$ . Therefore it is often safe to assume that  $\gamma \approx g$  (Schneider, 2006b).

The observed brightness distribution of a galaxy image  $I(\boldsymbol{\theta})$  is not in general perfectly elliptical, but we can approximate it as an ellipse in the following manner. The center of the brightness distribution of the image is

$$\bar{\boldsymbol{\theta}} \equiv \frac{\int d^2\boldsymbol{\theta} I(\boldsymbol{\theta}) q_I(I(\boldsymbol{\theta})) \boldsymbol{\theta}}{\int d^2\boldsymbol{\theta} I(\boldsymbol{\theta}) q_I(I(\boldsymbol{\theta}))}, \quad (1.25)$$

where  $q_I(I(\boldsymbol{\theta}))$  is some weight function, and we assume that the galaxy image of interest is isolated on the sky. To describe ellipticity we will be interested in the second brightness moments of the source, contained in the tensor

$$Q_{ij} = \frac{\int d^2\boldsymbol{\theta} I(\boldsymbol{\theta}) q_I(I(\boldsymbol{\theta})) (\theta_i - \bar{\theta}_i)(\theta_j - \bar{\theta}_j)}{\int d^2\boldsymbol{\theta} I(\boldsymbol{\theta}) q_I(I(\boldsymbol{\theta}))}, \quad (1.26)$$

where  $i, j \in (1, 2)$  (Schneider, 2006b). The size  $\omega$  of the galaxy image is just a function of the diagonal components of this matrix,

$$\omega = (Q_{11}Q_{22} - Q_{12}^2)^{1/2}, \quad (1.27)$$

while the shape, or ellipticity, of the image involves the off-diagonal elements:

$$\chi \equiv \frac{Q_{11} - Q_{22} + 2iQ_{12}}{Q_{11} + Q_{22}}, \quad (1.28)$$

$$\varepsilon \equiv \frac{Q_{11} - Q_{22} + 2iQ_{12}}{Q_{11} + Q_{22} + 2(Q_{11}Q_{22} - Q_{12}^2)^{1/2}}. \quad (1.29)$$

The complex ellipticity can be characterized by either of  $\chi$  or  $\varepsilon$ , which are simply related and interchangeable (in different situations one may be easier to work with) (Bartelmann and Schneider, 2001).

In analogy with the image center  $\bar{\boldsymbol{\theta}}$  and tensor of second brightness moments  $Q_{ij}$ , one can define the same quantities for the unlensed source center  $\bar{\boldsymbol{\beta}}$  and tensor of second brightness moments  $Q_{ij}^{(s)}$ . The relation between the source and image tensors is

$$Q^{(s)} = \mathcal{A} Q \mathcal{A}^T = \mathcal{A} Q \mathcal{A}, \quad (1.30)$$

where  $\mathcal{A} \equiv \mathcal{A}(\boldsymbol{\theta})$  is the Jacobian defined in Equation 1.21 and Equation 1.24. The observed source ellipticity  $\varepsilon$  is related both to the shear caused by weak lensing, and to the intrinsic ellipticity  $\varepsilon^{(s)}$  of the unlensed background source:

$$\varepsilon^{(s)} = \begin{cases} \frac{\varepsilon - g}{1 - g^* \varepsilon}, & \text{for } |g| \leq 1 \\ \frac{1 - g \varepsilon^*}{\varepsilon^* - g^*}, & \text{for } |g| > 1. \end{cases} \quad (1.31)$$

If we average over many background sources that are randomly oriented, then the average intrinsic ellipticity  $\langle \varepsilon^{(s)} \rangle = 0$  and we can apply the weak lensing approximation to conclude that  $\gamma \approx g \approx \langle \varepsilon \rangle \approx \langle \chi \rangle / 2$  (Bartelmann and Schneider, 2001).

In this thesis we are concerned with a particular manifestation of gravitational lensing – lensing by galaxy clusters. If we consider an circularly symmetric mass density on the sky (an idealized galaxy cluster), then we

expect the shear distortion to be oriented tangential to the center of the lens. It is therefore useful in cluster lensing (and also in galaxy-galaxy lensing) to express the shear in terms of tangential and rotated (or cross) components:

$$\gamma_t = -\text{Re} [\gamma e^{-2i\phi}], \quad (1.32)$$

$$\gamma_r = -\text{Im} [\gamma e^{-2i\phi}]. \quad (1.33)$$

Here the angle  $\phi$  is the azimuthal angle measured about the center of the lens (Schneider, 2006b). The rotated shear (which would represent a curl component) should be consistent with zero, and is often used as a check of systematic effects. Even though any single galaxy cluster (or other lens) is likely not perfectly azimuthally symmetric, we expect a stack of many galaxy clusters to yield a symmetric profile on average.

Similar to the surface mass density representation of the convergence (Equation 1.19), we can then relate the tangential shear to the differential surface mass density of the lens:

$$\gamma(\theta) = \frac{\Delta\Sigma(\theta)}{\Sigma_{\text{crit}}}, \quad (1.34)$$

where  $\theta$  now specifies the radial angle of separation between the lens center and the source image. The differential surface mass density is defined to equal the difference between the average surface mass density interior to  $\theta$  and the surface mass density at  $\theta$  (Wright and Brainerd, 2000):

$$\Delta\Sigma(\theta) \equiv \bar{\Sigma}(<\theta) - \Sigma(\theta). \quad (1.35)$$

Given an expression for the mass density profile of a gravitational lens, and angular diameter distances involved, the expected tangential shear profile can be derived. Useful models for galaxy cluster masses, and the resulting  $\gamma(\theta)$  and  $\Delta\Sigma(\theta)$  profiles, will be given in Section 1.3.

### 1.2.2 Weak Lensing Magnification

Gravitational lensing causes the magnification of background galaxies due to the isotropic focusing of the lensed light rays (whereas shear arises from the anisotropic component). Magnification  $\mu(\theta)$  is related to the determinant of the Jacobian,

$$\mu = \frac{1}{\det \mathcal{A}} = \frac{1}{(1 - \kappa)^2 - |\gamma|^2}. \quad (1.36)$$

In the weak lensing limit ( $|\gamma| \ll 1$ ), the magnification is simply a measure of the convergence of a lensing mass,  $\mu \approx 1 + 2\kappa$ , where  $\kappa$  is defined in Equation 1.18 and Equation 1.19 (Schneider, 2006a). For the case of circularly symmetric sources we can write  $\mu = (\theta/\beta_L)(d\theta/d\beta_L)$  (Narayan and Bartelmann, 1996). Conceptually, magnification can be understood as the stretching of solid angle on the sky, which causes the amplification of source flux, since lensing conserves surface brightness. This directly leads to a change in source size  $\omega = \mu(\theta)\omega^{(s)}$ , where size is defined in Equation 1.27 (Bartelmann and Schneider, 2001).

In general, two different approaches can be taken to measure magnification: (1) quantifying sizes of galaxies behind lenses and measuring lensing-induced changes, or (2) detecting the effect on background source number density that ensues as a result of amplification in a flux-limited survey. This thesis focuses on the latter approach. The former method suffers from many of the limitations facing shear analysis, and will be discussed briefly in

Section 1.2.3 below.

Define  $n_0(f, z)dfdz$  to be the intrinsic (unlensed) number of galaxies per solid angle within  $df$  of flux  $f$  and  $dz$  of redshift  $z$ . The cumulative lensed number density detectable (i.e. brighter than  $f$ ) in an astronomical survey will then be:

$$n(>f, \theta, z) = \frac{1}{\mu(\theta, z)} n_0\left(\frac{>f}{\mu(\theta, z)}, z\right). \quad (1.37)$$

In this equation we can see that magnification affects the source number densities in two ways. The prefactor  $1/\mu$  represents the stretching of apparent solid angle, and decreases the number density on the sky. Meanwhile, the denominator in the argument of  $n_0$  implies that sources will be detectable to a fainter intrinsic magnitude, effectively increasing the observed source number density if there exist sources fainter than the detection limit of the survey (Schneider, 2006b).

Since magnification affects the background source number densities in these two opposing ways, we require knowledge of the intrinsic source number densities as a function of brightness, in order to predict or interpret our magnification observations. Typically, astronomical sources such as galaxies contain relatively few very bright members and are much more numerous towards the faint end. If we approximate the slope of the number density in a narrow flux bin as a power law  $n_0(f) \propto f^{-\alpha}$ , then we have

$$\frac{n(>f)}{n_0(>f)} = \mu^{\alpha-1}. \quad (1.38)$$

Unfortunately, instead of using flux, astronomers frequently characterize source brightness using the ancient-Greek-inspired system of magnitudes. The apparent (observed) magnitude of an object with flux  $S$  is

$$m \equiv -2.5 \log_{10}(f/f_x), \quad (1.39)$$

where  $f_x = 2.53 \times 10^{-8} \text{ W/m}^2$  is a reference flux (Ryden, 2003). Bright sources have smaller apparent magnitudes. **An absolute magnitude can be defined... necessary?** In terms of apparent magnitudes we can relate the lensed and intrinsic number densities using the equation

$$n(m, z)dm = \mu^{\alpha-1} n_0(m, z)dm, \quad (1.40)$$

where we now define  $\alpha$  explicitly according to

$$\alpha \equiv \alpha(m, z) = 2.5 \frac{d}{dm} \log n_0(m, z). \quad (1.41)$$

The form of Equation 1.40 was first demonstrated by Narayan (1989), who applied it to lensed quasar number densities, but it can be generalized to any galaxy type as long as one has a means of obtaining the slope of the number counts  $\alpha$ .

Returning to the question of whether gravitational lensing magnification will cause an increase or decrease in observed number densities of background sources, we find that the answer depends precisely on the value of  $\alpha$ . Sources for which  $\alpha - 1 > 0$  will appear to be correlated on the sky with a lens position, while sources with  $\alpha - 1 < 0$  will be anti-correlated, as a dearth of objects will be observed in the vicinity of a lens. The number density of galaxies for which the intrinsic number count slope gives  $\alpha - 1 \approx 0$  will essentially be unaffected by lensing magnification, as the dilution and amplification effects will cancel, and no correlation signal will

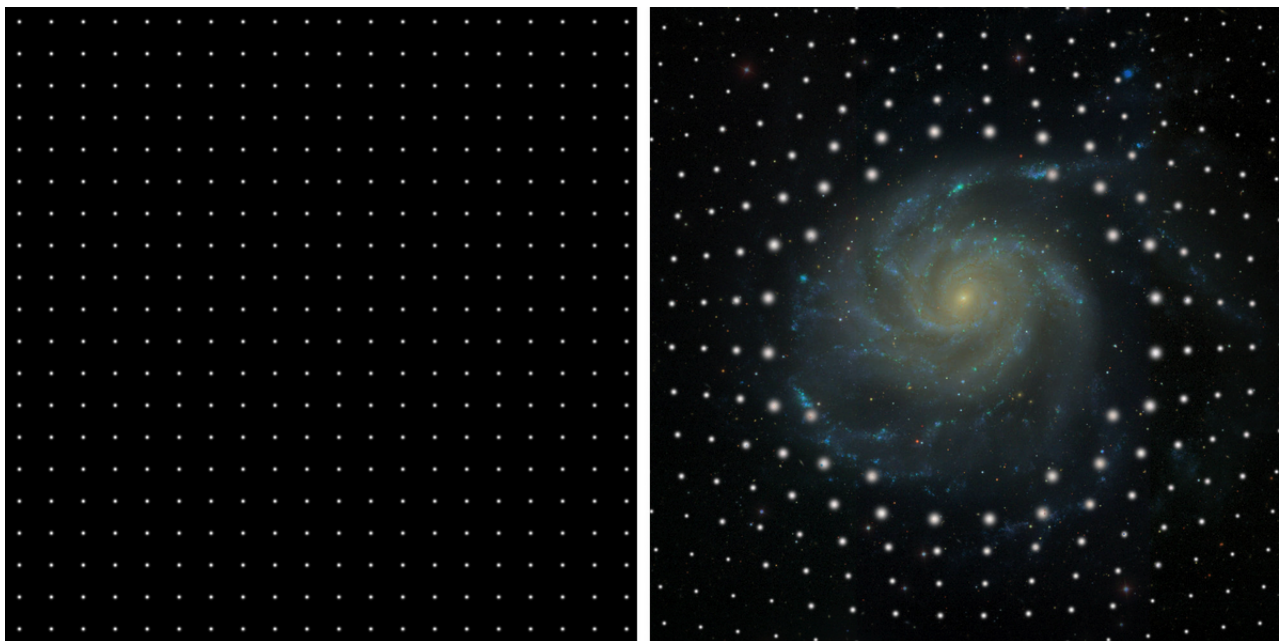


**Figure 1.3:** Highly exaggerated illustration of the two effects of magnification (dilution and amplification) by a massive foreground galaxy. The left panel shows an idealized set of unlensed sources, the right panel shows the effect of gravitational lensing. Dilution refers to the stretching of solid angle on the sky, which reduces background source number density. Since lensing conserves surface brightness, a consequence is that source flux is amplified. [Source: Joerg Colberg, Ryan Scranton, Robert Lupton, SDSS].

be observed for these objects (Scranton et al., 2005). The brightest sources, which usually have steep number counts, will exhibit an *increase* in number density when lensed, as the amplification allows more objects to be detected, while the number density of the faintest sources, having relatively shallow number counts, will *decrease* (Narayan, 1989).

The first measurement? or calculation? was by Broadhurst et al. (1995) Important early lensing calculations by Kaiser and Squires (1993) First description of lensing for measuring mass was by Tyson et al. (1984). first realization that quasar excess around galaxies was due to lensing was by Narayan (1989).

### 1.2.3 Magnification vs. Shear

Compared to shear measurements, magnification exhibits a slightly lower signal-to-noise ( $S/N$ ) ratio, the reason it has been largely ignored until recently. However, what magnification lacks in signal strength, it makes up for in terms of its ability to be applied to lenses at higher redshift and to poorly resolved sources (van Waerbeke, 2010). Since shear studies require measurements of galaxy shapes, in order for a source to be used it must necessarily be well resolved. This is in stark contrast to magnification studies using source number densities, which have no such requirement for the sources to be resolved at all. In principle only source magnitudes, redshifts, and positions relative to a lens must be known. This simple fact makes it possible to extend weak lensing magnification analyses to a much higher redshift than possible for shear, and allows a much higher source density to be included in the analysis.

Because the constraint on source resolution is considerably relaxed, ground-based observations can be in-

incorporated to a greater degree with magnification than for shear, as we are not concerned with correcting for the smearing of the image due to the Point Spread Function. From the financial perspective, magnification studies are therefore extremely cheap to carry out, since the excellent resolution of space-based telescopes is not required. See van Waerbeke (2010), Rozo and Schmidt (2010), and Umetsu et al. (2011), for more detailed discussions of the benefits of combining magnification with shear in gravitational lensing studies.

size measurements more difficult than shapes, bottom pg 12 of Schneider ecopy. comparison pg 349 BS01

## 1.3 Galaxy Clusters

NFW on pg 76 of Schneider hardcopy.

### 1.3.1 Clusters as Cosmological Probes

### 1.3.2 Intracluster Physics

## 1.4 Impact of this Thesis

This work contained in this thesis has pushed the boundaries of what knowledge can be extracted from weak lensing surveys. By including intrinsically smaller and fainter background sources, which cannot be used in conventional weak lensing studies, we pave the way for a more optimal use of survey data. These gravitationally-lensed sources, which are too small for reliable shape or size measurements, can still be included in a lensing analysis by using the flux magnification formalism described in Section 1.2.2. The author of this thesis has proven the utility of measuring magnification, through several key publications which appear as chapters in this work, and carried out thorough studies of the systematic effects which provide limitations.

Prior to this thesis research, weak lensing was dominated by the shear method. This was originally motivated by some early work showing that the signal-to-noise for shear was several times larger than for magnification (Schneider et al., 2000). While it is true that, for a fixed sample of galaxies, there is less scatter in galaxy shapes than in galaxy positions, the latter is far easier to measure. This simple fact has motivated the research herein. As lensing studies push to higher redshift, and increasingly rely on blurry ground-based data, we have elevated confidence in our measurements of source positions over difficult shape determinations.

When this thesis work began, only a handful of magnification studies had been completed. The first groundbreaking theoretical formulation of how number densities of sources could be used to measure masses of clusters was laid out in 1995 by Broadhurst et al. (1995), but it took another 20 years before the first convincing observational detection was made (Scranton et al., 2005). Following this significant  $8\sigma$  detection of galaxy-magnified quasars in the Sloan Digital Sky Survey (SDSS), several studies followed, achieving magnification detections for lensing of normal galaxies (Hildebrandt et al., 2009b), and of blue galaxies behind strong lensing clusters (Umetsu et al., 2011). These studies all stopped short of deriving scientifically useful results from the magnification measurements – they either represented proof-of-concept studies for a new technique, or they demonstrated consistency with a lensing interpretation of the signal.

The work in this thesis made major steps forward in the area of lensing magnification. The author performed the first-ever measurement of magnification by stacked galaxy groups in 2012 (See Chapter 2). This particular work was also the first time that shear and magnification mass estimates and signal-to-noise had been compared (Ford et al., 2012). Following this influential work in the Cosmological Evolution Survey (COSMOS) survey, the



thesis author transitioned focus to the much larger astronomical survey known as the Canada-France-Hawaii-Telescope Lensing Survey (CFHTLENS).

Two important studies resulted from magnification analyses of the CFHTLENS for this thesis (See Chapter 3 and Chapter 4). First of all, the most significant magnification detection thus far (at  $9.7\sigma$ ) was published in Ford et al. (2014). More importantly, however, that work moved beyond simple magnification-detection to actual science. The thesis author measured masses of stacked galaxy clusters binned as a function of different attributes (redshift and richness), and the dependence of a magnification signal on these parameters was seen for the first time. A mass-richness scaling relation was determined solely from the magnification results, which is a useful tool for making cosmological inferences from optical cluster surveys, as discussed in Section 1.3.

This work contained the important inclusion of a means of accounting for one of the dominant systematic effects for magnification, the contamination of the background sources with low-redshift objects. The formalism was extended from earlier work by Hildebrandt et al. (2013), but allowing for different contamination fractions and models for the halo occupation distribution of the galaxy contaminants. This was the first time that galaxy cluster lenses could be used for magnification in a redshift range where there was known source contamination. Prior to this work, the redshift ranges of overlap had to be avoided because the physically-induced cross-correlations of lens and source objects overwhelmed, and could not be separated from, the magnification signal.

Arguably the most important magnification result in all the literature to date is contained in Chapter 4 of this thesis. After the semi-blind magnification analysis of Ford et al. (2014), Ford et al. (2015) followed suit with an identical treatment of the same cluster sample, but this time using the weak lensing shear approach. This study contained a detailed comparison between cluster masses measured with the two independent techniques, as a function of different cluster attributes, and contained valuable insights regarding systematic effects that are still important to resolve for magnification. Moving forward, this work frames the case for including magnification, and also pin-points some important issues that must be addressed in future work (see Chapter 5).

## 1.5 Thesis Overview

The body of this thesis is composed of three published studies that develop the weak gravitational lensing magnification technique, particularly for the study of galaxy clusters, and compare with results using the complementary and much more ubiquitous weak lensing shear approach:

- Chapter 2 contains the first magnification study of galaxy groups and first comparison with shear for stacked lens samples. The data are X-ray selected groups, and high-redshift Lyman-break galaxies in the acCOSMOS field.
- Chapter 3 represents the highest-significance magnification detection, and the first magnification study that could be binned as a function of cluster parameters. The data are optically-selected galaxy clusters and high-redshift Lyman-break galaxies in the acCFHTLenS field.
- Chapter 4 is the follow-up shear analysis of the same cluster sample presented in the previous chapter, using the acCFHTLenS shear catalog for background source shape measurements.

Finally, Chapter 5 wraps up with conclusions on the topic of cluster studies using both magnification and shear, and briefly outlines future directions for progress within the field.

## Chapter 2

# Magnification by Galaxy Group Dark Matter Halos

We report on the detection of gravitational lensing magnification by a population of low-mass galaxy groups, at a significance level of  $4.8\sigma$ . Using X-ray selected groups in the COSMOS  $1.64 \text{ deg}^2$  field, and high-redshift Lyman-break galaxies as sources, we measure a lensing induced angular cross-correlation between the samples. After satisfying consistency checks that demonstrate we have indeed detected a magnification signal, and are not suffering from contamination by physical overlap of samples, we proceed to implement an optimally-weighted cross-correlation function to further boost the signal-to-noise of the measurement. Interpreting this optimally weighted measurement allows us to study properties of the lensing groups. We find that the group mass profiles are well fit by the Singular Isothermal Sphere (SIS) model, and we implement a multi-SIS fit that recovers a distribution of lens masses consistent with the values that have already been well measured using the weak lensing shear technique. We argue that future weak lensing studies will need to incorporate magnification along with shear, both to reduce residual systematics and to make full use of all available source information, in an effort to maximize scientific yield of the observations.

### 2.1 Introduction

Weak gravitational lensing is a unique tool for probing the mass distribution of the universe and for constraining dark matter halo properties of galaxies and clusters. In contrast to alternative mass estimate methods (employing e.g. X-ray temperatures, radial velocities, or mass-to-light ratios), weak lensing does not rely on any assumptions about virial equilibrium and is sensitive to all mass along the line of sight, making no distinction between luminous and dark matter.

Over the past decade, an enormous international effort has been invested in improving the reliability of weak lensing analysis (Heymans et al., 2006; Massey et al., 2007a; Bridle et al., 2009; Kitching et al., 2010), seeking to remove biases and systematic effects that limit the accuracy of the method. By far most of the work has been focused on measuring the shear signal, the coherent stretching and distortion of distant galaxy shapes by a foreground lensing mass, but recently the magnification signal has begun to attract attention as well (Scranton et al., 2005; Hildebrandt et al., 2009b, 2011; Van Waerbeke et al., 2010; Umetsu et al., 2011).

Weak lensing magnification is, to first order, a measure of the convergence of a lensing mass. It can be detected through the stretching of solid angle on the sky, which leads to the amplification of source flux, since

lensing conserves surface brightness (i.e. photons are neither created nor destroyed in purely lensing processes). In general, two different approaches can be taken to measure magnification. The method we employ here involves observing the effects on source number densities; an interesting alternative method is being explored by Schmidt et al. (2012), which makes use of source size and flux information, and employs the same COSMOS X-ray groups used in this study.

Magnification affects the source number densities in two ways, and the one that dominates is determined by the intrinsic magnitude number counts of the sources in question. Simply put, the brightest sources, which usually have steep number counts, will exhibit an *increase* in number density when lensed, as the amplification allows more objects to be detected, while the number density of the faintest sources, having relatively shallow number counts, will *decrease* (Narayan, 1989).

Compared to shear measurements, magnification exhibits a slightly lower signal-to-noise ( $S/N$ ) ratio, the reason it has been largely ignored until recently. However, what magnification lacks in signal strength, it makes up for in terms of its ability to be applied to lenses at higher redshift and to poorly resolved sources (van Waerbeke, 2010). Since shear studies require measurements of galaxy shapes, in order for a source to be used it must necessarily be well resolved. This is in stark contrast to magnification studies using source number densities, which have no such requirement for the sources to be resolved at all! In principle only source magnitudes, redshifts, and positions relative to a lens must be known. This simple fact makes it possible to extend weak lensing magnification analyses to a much higher redshift than possible for shear, and allows a much higher source density to be included in the analysis. See van Waerbeke (2010), Rozo and Schmidt (2010), and Umetsu et al. (2011), for more detailed discussions of the benefits of combining magnification with shear in gravitational lensing studies.

In Section 2.2 we review the equations describing the effects of weak lensing magnification on source number densities. Section 4.2 gives the properties of the X-ray groups and Lyman-break galaxies that are used in this study. Then Section 3.4 describes the steps of our analysis, and results of the Singular Isothermal Sphere (SIS) model fitting. We summarize the results in Section 2.5, and compare with weak lensing shear measurements that have previously been made on populations of galaxy groups. We use the WMAP7  $\Lambda$ CDM cosmological parameters  $H_0 = 71 \text{ km s}^{-1} \text{ Mpc}^{-1}$  and  $\Omega_\Lambda = 0.734$  (Larson et al., 2011), and set  $\Omega_M = 1 - \Omega_\Lambda$ .

## 2.2 Theory

The amplification matrix  $\mathcal{A}$  maps the image deformation from the source to observer frame, and describes the first order effects of gravitational lensing.

$$\mathcal{A} = \begin{pmatrix} 1 - \kappa - \gamma_1 & -\gamma_2 \\ -\gamma_2 & 1 - \kappa + \gamma_1 \end{pmatrix} \quad (2.1)$$

It is a function of the convergence  $\kappa$ , and the shear  $\gamma$ , which define the isotropic and anisotropic focusing of light rays, respectively. The magnification factor  $\mu$  is the inverse determinant of this matrix, so that

$$\mu = \frac{1}{\det \mathcal{A}} = \frac{1}{(1 - \kappa)^2 - |\gamma|^2} \quad (2.2)$$

(Bartelmann and Schneider, 2001).

The cumulative number counts of distant *unlensed* sources  $N_0$  are related to the observed *lensed* number

counts  $N$ , up to some flux  $f$ , by the equation

$$N(> f) = \frac{1}{\mu} N_0 \left( > \frac{f}{\mu} \right). \quad (2.3)$$

Here the two distinct effects of weak lensing magnification, on source number counts, are made explicit. The prefactor of  $1/\mu$  is the dilution of source density, as the observed solid angle on the sky is stretched by a foreground massive lens. The modification to the flux  $f/\mu$  inside the argument of  $N_0$  represents the effect of source amplification by a lens, such that one is able to detect intrinsically fainter objects due to gravitational lensing.

Switching from working in fluxes to magnitudes  $m$ , the differential number count relationship was demonstrated by Narayan (1989) to be

$$n(m)dm = \mu^{\alpha-1} n_0(m)dm, \quad (2.4)$$

where  $\alpha$  is defined according to

$$\alpha \equiv \alpha(m) = 2.5 \frac{d}{dm} \log n_0(m). \quad (2.5)$$

Thus distant source galaxies, lensed by an intervening concentration of mass, may have their observed number counts increased *or* decreased depending on the sign of the quantity  $\alpha - 1$ . Sources for which  $\alpha - 1 > 0$  will appear to be correlated on the sky with a lens position, while sources with  $\alpha - 1 < 0$  will be anti-correlated, as a dearth of objects will be observed in the vicinity of a lens. The number density of galaxies for which the intrinsic number count slope gives  $\alpha - 1 \approx 0$  will essentially be unaffected by lensing magnification, as the dilution and amplification effects will cancel, and no correlation signal will be observed for these objects (Scranton et al., 2005).

## 2.3 Data

### 2.3.1 Lenses

The lenses in this study consist of X-ray selected galaxy groups in the COSMOS Field. See Leauthaud et al. (2010) for the detailed properties of these groups. From the full sample of 206 groups investigated in the aforementioned study, we use the shear-calibrated mass estimates to construct the most massive subsample of groups for this magnification study. Here masses are characterized by the parameter  $M_{200}$ , the total mass interior to a sphere of radius  $R_{200}$ , within which the average density is 200 times the critical.

Any groups that have less than 4 member galaxies, that appear to be undergoing mergers, that have uncertain centroids, or that raise concerns about projection effects, are excluded from the analysis. These restrictions follow from the group catalog requirement `FLAG_INCLUDE=1`, discussed in George et al. (2011). The remaining 44 most massive groups have shear determined masses in the range  $3.56 \times 10^{13} \leq M_{200}/M_{\odot} \leq 1.70 \times 10^{14}$ , and we employ stacking to increase the  $S/N$  of the magnification measurement. The redshift range of the groups is  $0.32 \leq z \leq 0.98$ . Figure 2.1 displays these lens properties.

Choosing an optimal lens centroid about which to construct angular bins is an area of ongoing research, and common choices include the brightest central galaxy or the X-ray emission peak. If the location of the dark matter density peak were known *a priori*, then it would obviously be the ideal choice, but instead we must rely upon some combination of observables to approximate this position. In this paper, we define lensing mass centers

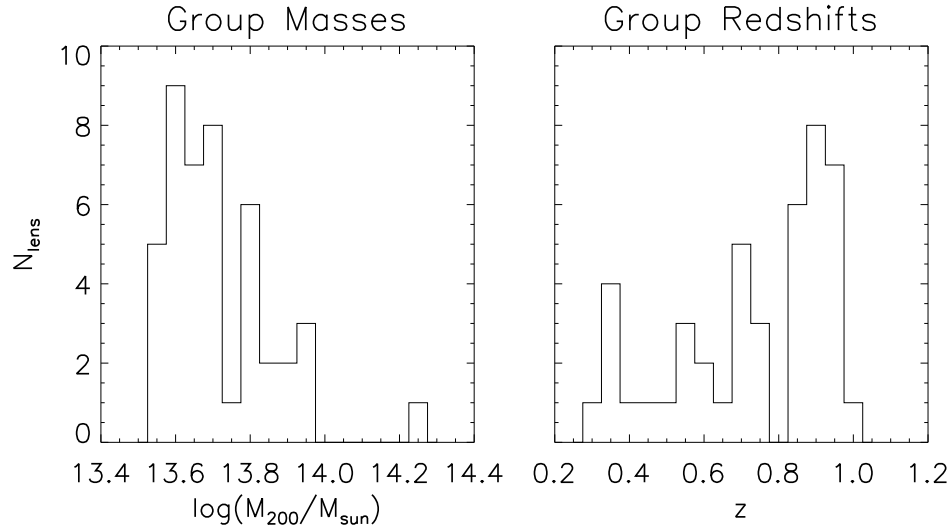


**Figure 2.1:** Masses and photometric redshifts of the groups in this study. We select the most massive groups in our sample,  $M_{200}/M_{\odot} \geq 3.56 \times 10^{13}$ . Using only the cleanest groups (characterized by having  $\geq 4$  members, well-defined centroids, and no flags on possible mergers or projection effects), and applying appropriate masking, we are left with a sample of 44 groups for this lensing magnification analysis.

by the location of the group galaxy with highest stellar mass ( $\text{MMGG}_{\text{scale}}$ ) lying within a distance ( $R_s + \sigma_x$ ) of the X-ray center, where  $R_s$  is the group scale radius and  $\sigma_x$  is the uncertainty in the X-ray center position (George et al., 2011). In order to be very confident about the locations of group centers, we exclude groups for which this galaxy is not the most massive member of the group. This choice of centroid has been shown to optimally boost the measured shear signal for this group sample (M. George et al. 2011, in preparation).

### 2.3.2 Sources

Background sources are Lyman-break galaxies (LBGs), a type of high-redshift star-forming galaxy that has been used successfully in previous magnification studies (see Hildebrandt et al., 2009b, 2011). These LBGs were selected using the typical three color dropout technique. For the  $U$ -,  $G$ -, and  $R$ -dropouts the selections described in Hildebrandt et al. (2009a) were used, however the COSMOS Subaru  $g^+$  and  $r^+$  data were used instead of the CFHT-LS  $g^*$  and  $r^*$  data (see Capak et al. (2007) for the filter definitions). For the  $B$ -dropouts the selection from Ouchi et al. (2004) was used.

The appeal of using LBGs for magnification is rooted in the fact that their luminosity functions have been extensively studied and their redshift distributions are fairly narrow and accurate. After all quality cuts and image masking, we are left with 45,132 LBGs in total. The four distinct sets are comprised of 12,980  $U$ -, 22,520  $G$ -, 4,870  $B$ -, and 4,762  $R$ -dropouts, located at redshifts of  $\sim 3.1, 3.8, 4.0$ , and  $4.8$ , respectively.

We first test our data selection by cross-correlating the foreground groups with LBGs separated into discrete magnitude bins. Here we use the basic Landy and Szalay (1993) estimator,

$$w(\theta) = \frac{D_1 D_2 - D_1 R - D_2 R + RR}{RR}, \quad (2.6)$$

to simply compute cross-correlations between groups and background sources.  $D_1$  and  $D_2$  represent the data sets

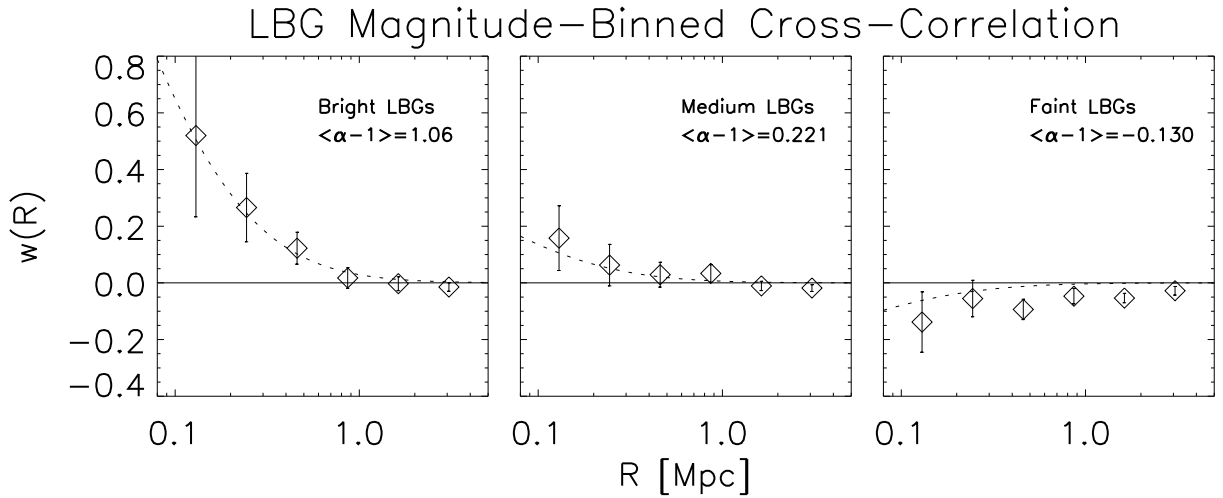


**Figure 2.2:** Angular cross-correlation of the X-ray groups with Lyman-break galaxies, the latter separated into 3 magnitude-selected samples. The Bright sample contains  $U$ ,  $G$ ,  $B$ ,  $R$ -dropouts in the magnitude ranges  $23 < r < 25$ ,  $23.5 < i < 25$ ,  $23.5 < i < 25$ ,  $24 < z < 25.5$ , respectively. Similarly, the Medium ranges are  $25 < r < 25.5$ ,  $25 < i < 26$ ,  $25 < i < 26$ ,  $25.5 < z < 26$ . The Faint ranges are  $r > 25.5$ ,  $i > 26$ ,  $i > 26$ ,  $z > 26$ . These magnitude ranges are selected to contain LBGs for which  $(\alpha - 1) > 0$ ,  $\approx 0$ , and  $< 0$ . The measured correlations for each LBG sample are simply averaged here (weighting by the number counts) in order to more clearly display this diagnostic check. The negative correlation observed for the faintest sample is a good indication that no redshift overlap exists between foreground lenses and background sources.

of lenses and sources, and  $R$  are the *random objects* from a mock catalog we create, containing points uniformly distributed throughout the COSMOS survey area. Each product of terms is the number of pairs of those objects found to lie within some angular bin, normalized by the total number of pairs found at all angular separations. This cross-correlation estimator has been shown to be both robust and unbiased (Kerscher et al., 2000).

In any lensing study, care must be taken to ensure that regions of an image containing artifacts such as saturated pixels, satellite tracks, or other spurious effects, are masked out of the investigation. We consistently apply the same masks to the group, source, and random catalogs, prior to the correlation analysis. Using a large number (584,586) of objects in this random catalog serves to reduce shot noise.

We expect that the faintest (brightest) magnitude bins should yield a negative (positive) cross-correlation with the group centers, and this is exactly what we find. Figure 2.2 displays this anticipated result, where we simply use a number count weighted average to combine the signal of the distinct LBG samples. As discussed in Hildebrandt et al. (2009b), this negative correlation is one of the strongest verifications that no redshift overlap exists between lens and source populations, for no viable reason other than lensing magnification can be given for such a signal to exist. Redshift overlap between samples must be avoided in magnification studies, as positive cross-correlations due to physical clustering would overwhelm any lensing induced signal.

## 2.4 Analysis and Results

### 2.4.1 Measuring $\alpha(m)$

Along with the mass of the lens itself, the slope of the source number counts as a function of magnitude, parameterized by the quantity  $\alpha \equiv \alpha(m)$ , controls the amplitude and sign of the expected magnification signal. To interpret the correlations that we measure, and to implement an optimally-weighted procedure, we must determine the value of this quantity for every source galaxy that we intend to use in the measurement. Fortunately, LBGs have been extensively studied and many measurements of their Luminosity Functions (LF) have been published.

For the  $U$ -,  $G$ -, and  $R$ -dropouts, we use the recent measurements by van der Burg et al. (2010). For the  $B$ -dropouts we use the results of Sawicki and Thompson (2006). These two sets of measurements both involved fitting a Schechter Function (Schechter, 1976) to their galaxy number counts, and their best fit parameters that we use here, are displayed in Table 1. The Schechter Function is given by

$$\Phi(M) = 0.4 \ln(10) \Phi^* 10^{0.4(\alpha_{LF}+1)(M^*-M)} \exp[-10^{0.4(M^*-M)}], \quad (2.7)$$

where  $\Phi^*$ ,  $M^*$ , and  $\alpha_{LF}$  are the normalization, characteristic magnitude, and faint-end slope of the LF. Note that the  $\alpha(m)$  which we want to calculate is not the same as the constant parameter  $\alpha_{LF}$ , but approaches it in the limit of very faint magnitudes.

Solving this equation for  $\alpha(m)$ , we obtain

$$\alpha(m) = 2.5 \frac{d}{dm} \log n_0(m) = 2.5 \frac{d}{dM} \log \Phi(M) = 10^{0.4(M^*-M)} - \alpha_{LF} - 1. \quad (2.8)$$

We convert the observed apparent magnitudes  $m$  of the LBGs to absolute magnitudes  $M$  via the relationship  $M = m - DM + 2.5 \log(1+z)$ , where  $DM$  and  $z$  are the distance modulus and redshift of the galaxy in question. Since we select apparent magnitudes in the  $r$ ,  $i$ , and  $z$  bands for the  $U$ -,  $G$ - and  $B$ -, and  $R$ -dropouts, we probe very similar restframe wavelengths and the  $K$ -correction between the samples is negligible. Thus we ignore it here. Using the LF parameters in Table 2.1, combined with the conversion to absolute magnitudes, we then obtain a robust measure of  $\alpha(m)$  for every LBG in the sample.

### 2.4.2 Optimally-Weighted Cross-Correlation

We implement a modified version of the Landy and Szalay (1993) estimator for the angular cross-correlation function, in which pair counts are weighted by their expectations from the differential source number counts as a function of magnitude. This weighted correlation function has been shown to optimally boost the magnification signal (Ménard et al., 2003):

$$w(\theta)_{optimal} = \frac{S^{\alpha-1}L - S^{\alpha-1}R - \langle \alpha - 1 \rangle LR}{RR} + \langle \alpha - 1 \rangle. \quad (2.9)$$

Optimal-weighting was first implemented by Scranton et al. (2005) and, apart from notation, this equation is identical to the estimator used in Hildebrandt et al. (2009b). As with the original basic estimator, each term represents the number of pairs of objects found in a given angular  $\theta$  bin, normalized by the total number of pairs at all angular separations.

**Table 2.1:** Luminosity Function (Schechter) parameters from external LBG measurements. <sup>a</sup> LF parameters from van der Burg et al. (2010). <sup>b</sup> LF parameters from Sawicki and Thompson (2006).

LBG Sample	$M^*$	$\alpha_{LF}$	Number
U ( $z \sim 3.1$ ) <sup>a</sup>	-20.84	-1.60	12,980
G ( $z \sim 3.8$ ) <sup>a</sup>	-20.84	-1.56	22,520
B ( $z \sim 4.0$ ) <sup>b</sup>	-21.00	-1.26	4,870
R ( $z \sim 4.8$ ) <sup>a</sup>	-20.94	-1.65	4,762

$S$  stands for the *sources*, or background lensed galaxies,  $L$  are the *lenses*, or X-ray groups, and once again  $R$  are the *random objects*. The superscript  $\alpha - 1$  on the  $S$  indicates that pair counts involving sources are to be weighted by this factor. After removing masked objects from the catalogs, and satisfying the above selection criteria, we are left with 45,132 LBG sources, 44 X-ray group lenses, and 584,586 random objects for the analysis.

The brightest source galaxies, which are observationally found to lie in the steepest part of the luminosity function, are expected to be positively correlated with the group centers, have the largest value of  $\alpha - 1$ , and so receive a relatively large weight in this correlation study. In contrast, the faintest background galaxies are expected to be anti-correlated, on average, with the group positions, because the effects of magnification dilution should be greater than the amplification of flux can compensate for, and these galaxies thus receive a negative weight. Sources for which  $\alpha - 1 \approx 0$ , ought to have the effects of dilution and amplification cancel out overall, and receive very little to no weight in this analysis (Scranton et al., 2005). The optimally weighted correlation function is given in Figure 2.3, and shows the measured radial profile for this stack of massive galaxy groups.

Error bars are  $1\sigma$  uncertainties, obtained by jackknife resampling of the source population. To do this, we create 30 jackknife samples of data, each with a different  $1/30$  of sources removed from it. Then we measure the optimal correlation function for each, and from these estimate the covariance matrix through

$$C(\theta_1, \theta_2) = \left( \frac{N}{N-1} \right)^2 \times \sum_{j=1}^N [w_j(\theta_1) - \bar{w}(\theta_1)] \times [w_j(\theta_2) - \bar{w}(\theta_2)], \quad (2.10)$$

where the index  $j$  runs over the  $N = 30$  jackknife measurements.

### 2.4.3 Halo Mass Profiles

Measuring the magnification-induced effects on source number counts behind massive lenses allows one to estimate properties of the lens, such as the mass profile. In this paper we use a Singular Isothermal Sphere (SIS) model to find the best fit mass parameter  $M_{200}$  for the groups. We choose the SIS primarily for its simplicity as a single-parameter model, in order to demonstrate a proof-of-concept for magnification studies. Although alternative models, e.g. NFW (Navarro et al., 1997), may better represent the true shape of the halo potential, magnification measurements alone cannot distinguish between the profiles for this small sample.

The SIS density profile is  $\rho(r) = \sigma_v^2 / (2\pi G r^2)$ , where  $G$  is the Gravitational constant and  $\sigma_v$  is the velocity dispersion of the lens. The velocity dispersion can be expressed in terms of the mass and critical energy density



of the universe at lens redshift  $z$ :

$$\sigma_v = \left[ \frac{\pi}{6} 200 \rho_{crit}(z) M_{200}^2 G^3 \right]^{\frac{1}{6}}. \quad (2.11)$$

The magnification of an SIS is given by

$$\mu_{SIS}(\theta) = \frac{\theta}{\theta - \theta_E}, \quad (2.12)$$

where  $\theta_E = 4\pi \left( \frac{\sigma_v}{c} \right)^2 \frac{D_{ls}}{D_s}$  is the Einstein radius of the lens, and  $D_{ls}$  and  $D_s$  are angular diameter distances between lens and source, and observer and source, respectively.

To account for the range of lens masses and redshifts, we perform a multi-SIS fit similar to Hildebrandt et al. (2011). The optimally weighted correlation function is related to the magnification constraint,  $\delta\mu(\theta) \equiv \mu(\theta) - 1$ , through

$$w(a)_{optimal} = \frac{1}{N_l} \sum_{i=1}^{N_l} \langle (\alpha - 1)^2 \rangle_i \delta\mu_{SIS}(z_i, a M_{shear,i}), \quad (2.13)$$

where  $i$  runs over all lenses. We use the minimum- $\chi^2$  method to fit the multi-SIS profile to the magnification measurements (see Fig. 2.3). The  $\chi^2/dof$  of the multi-SIS fit is 2.3 ( $\chi^2 = 11.5$ ,  $dof = 5$ ), and is calculated using the unbiased inverse covariance matrix, according to the prescription in Hartlap et al. (2007).

Here the fit parameter  $a$  characterizes the scaling relation between the  $M_{200}$  previously measured from the shear, and the best fit  $M_{200}$  from magnification, so that  $a \equiv M_{magnification}/M_{shear}$ . This approach allows us to fit for a range of masses, thereby avoiding any biases that would be introduced by simply fitting to a stacked average lens profile. We obtain a best fit value of  $a = 1.4 \pm 0.6$ , indicating consistency between the shear and magnification mass estimates for this lens sample.

## 2.5 Summary and Conclusions

We report a  $4.8\sigma$  detection of weak lensing magnification from a population of X-ray selected galaxy groups. This is the first magnification measurement using source number densities successfully performed on low-mass groups. Schmidt et al. (2012) has recently explored the magnification of these groups using source sizes and fluxes. For comparison, the shear detection significance is  $11\sigma$  on the same selection of 44 groups (A. Leauthaud 2011, private communication).<sup>1</sup>

To improve  $S/N$  in this measurement, we stack the lenses, consisting of 44 massive X-ray detected galaxy groups in the COSMOS 1.64 deg<sup>2</sup> field. We measure an optimally-weighted cross-correlation between the X-ray groups and high-redshift Lyman-break galaxies, with  $1\sigma$  error bars determined from jackknife resampling of the sources. Performing a multi-SIS fit to this optimally-weighted signal yields a measurement of the relative scaling between shear and magnification derived masses. Our magnification measurement yields a mass  $M_{mag} = a M_{shear}$  where the best fit parameter  $a = 1.4 \pm 0.6$ , consistent with the shear mass estimates.

We claim that Lyman-break galaxies are a preferred source sample when it comes to performing weak lensing magnification analyses using source number counts. A few reasons for the superiority of the LBG sample include more reliable redshift determinations, as well as greater lensing efficiencies and generally much higher values of the quantity  $\alpha - 1$ . The single most significant reason to choose LBGs for this type of analysis,

<sup>1</sup>The significance quoted for the shear does not take into account the full covariance matrix, as we have done for the magnification measurement. Therefore this shear significance might be a bit optimistic.

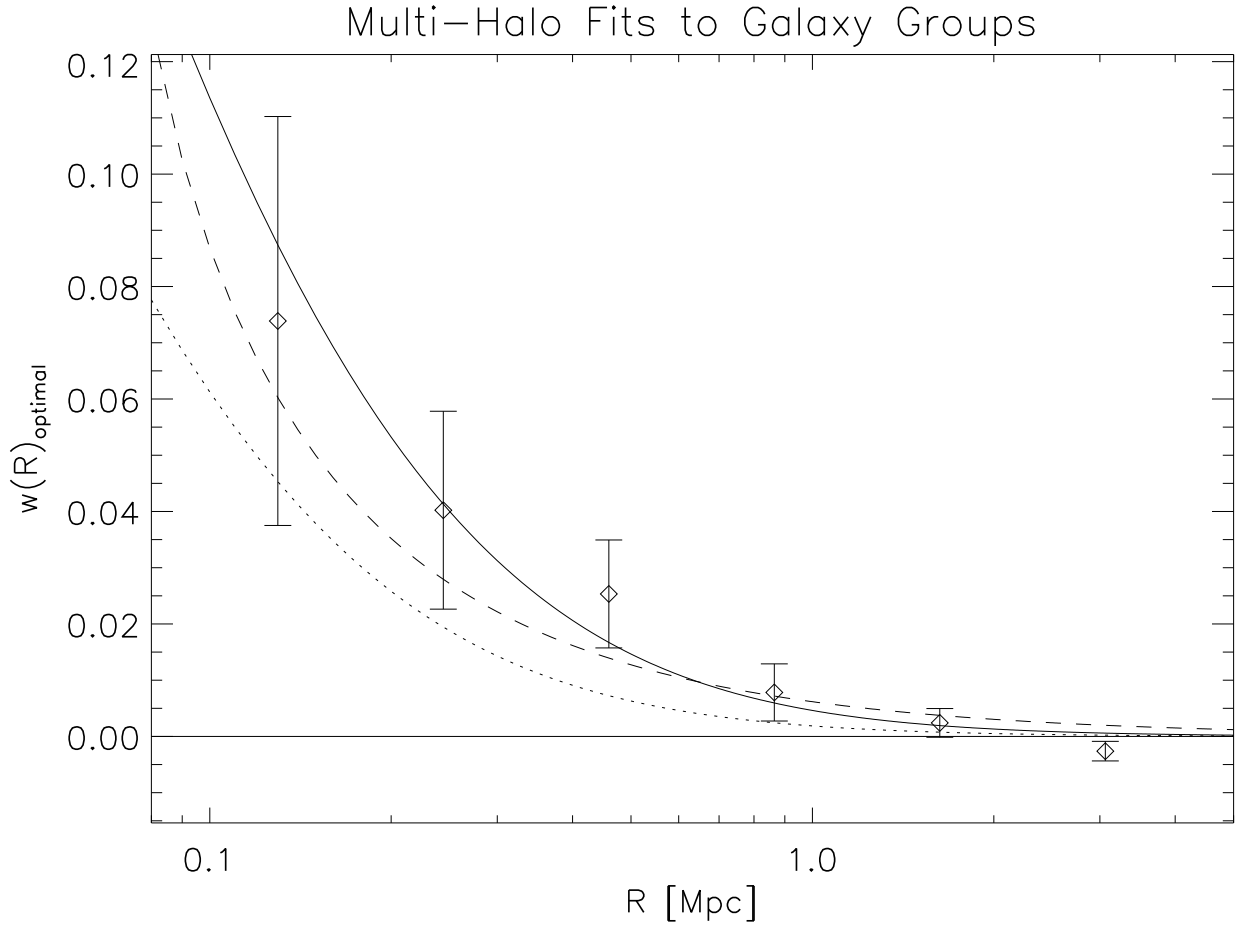


**Figure 2.3:** Multi-SIS fit to the optimally weighted correlation function, using the LBG background source sample. The significance of the magnification detection is  $4.8\sigma$ . The dashed line shows the prediction from the shear measured values of  $M_{200}$  (A. Leauthaud 2011, private communication), and the solid line is the best fit to the magnification measurement. We find the best fit relative scaling relation to be  $a = M_{mag}/M_{shear} = 1.4 \pm 0.6$ , consistent with the shear-measured group masses. It must be noted that the shear values for  $M_{200}$  were calculated assuming an NFW profile, but the dashed line plotted here is the resultant SIS achieved from applying these masses in an SIS context, for comparison.

however, is for the ease of obtaining a reliable measure of  $\alpha(m)$ . Previous deep measurements of LBG luminosity functions allow us to perform very simple calculations yielding the optimal weight factor  $\alpha = 1$ .

Although the  $S/N$  of shear is superior to magnification in general, the latter probes the surface mass density of the lens directly, while the shear measures the differential mass density. Thus the combination of these two independent measurements is desirable, and breaks the lens mass-sheet degeneracy. In fact, Rozo and Schmidt (2010) demonstrated that joining magnification into shear analyses, independent of survey details, can improve statistical precision by up to 40-50%. Magnification using source number densities is also far less sensitive to the effects of atmospheric seeing than either shear or magnification using source sizes. Both of these methods require quality source images which, for very high-redshift sources, can currently only be obtained from space-based data.

Improving the overall weak lensing derived constraints on cosmological and astrophysical parameters is not the only benefit to incorporating magnification into our analyses, however. Measurements of magnification

are sensitive to completely different systematics than shear, and therefore uniquely positioned to help improve calibration of these residual effects on shear measurements. For example, magnification (using number counts) is not at all sensitive to the possible intrinsic alignment of source galaxies, since it does not use any shape information. Magnification can also be used as a simultaneous probe of intergalactic dust extinction, a small but measurable effect through its wavelength dependence (Ménard et al., 2010), and as a direct way to measure galaxy bias (van Waerbeke, 2010).

As one proceeds to investigate dark matter structures at increasingly high redshift, it becomes more and more important to include the magnification component of the signal. This is a direct consequence of the fact that higher redshift lenses necessitate more distant sources, which are in turn much harder to measure shapes for. Proceeding exclusively with shear necessarily means that a high fraction of detected sources are being eliminated from the lensing analysis, and information is therefore being lost, simply because we lack the capabilities to robustly determine their shapes. With photometric redshifts available, the possibility to do magnification studies on our shear catalogs really comes along free of charge. Upcoming projects will survey the entire extragalactic sky, and the inclusion of magnification will be a necessary component of any robust weak lensing study.

## Chapter 3

# Cluster Magnification and the Mass-Richness Relation in CFHTLenS

Gravitational lensing magnification is measured with a significance of  $9.7\sigma$  on a large sample of galaxy clusters in the Canada-France-Hawaii Telescope Lensing Survey (CFHTLenS). This survey covers  $\sim 154 \text{ deg}^2$  and contains over 18,000 cluster candidates at redshifts  $0.2 \leq z \leq 0.9$ , detected using the 3D-Matched Filter cluster-finder of Milkeraitis et al. (2010). We fit composite-NFW models to the ensemble, accounting for cluster miscentering, source-lens redshift overlap, as well as nearby structure (the 2-halo term), and recover mass estimates of the cluster dark matter halos in range of  $\sim 10^{13} M_\odot$  to  $2 \times 10^{14} M_\odot$ . Cluster richness is measured for the entire sample, and we bin the clusters according to both richness and redshift. A mass-richness relation  $M_{200} = M_0 (N_{200}/20)^\beta$  is fit to the measurements. For two different cluster miscentering models we find consistent results for the normalization and slope,  $M_0 = (2.3 \pm 0.2) \times 10^{13} M_\odot$ ,  $\beta = 1.4 \pm 0.1$  and  $M_0 = (2.2 \pm 0.2) \times 10^{13} M_\odot$ ,  $\beta = 1.5 \pm 0.1$ . We find that accounting for the full redshift distribution of lenses and sources is important, since any overlap can have an impact on mass estimates inferred from flux magnification.

### 3.1 Introduction

Clusters of galaxies are the most massive gravitationally bound structures in the Universe today. As such they can be useful cosmological probes, as well as laboratories for all kinds of interesting physics including galaxy evolution, star formation rates, and interactions of the intergalactic medium. There are several methods commonly used to estimate cluster masses (e.g., mass-to-light ratios, Xray luminosities, the Sunyaev-Zeldovich effect), but among them gravitational lensing is unique in being sensitive to all mass along the line of sight, irrespective of its type or dynamical state (Bartelmann and Schneider, 2001).

There are multiple ways to measure the signature of gravitational lensing, and each has its own specific advantages and limitations. Observation of strong lensing arcs and multiple images is extremely useful for studying the innermost regions of clusters, and getting precise mass estimates, but can only be applied to very massive objects which are observationally limited in number. On the other hand, weak lensing shear, which measures slight deformations in background galaxy shapes, can be applied across a much wider range of lens masses. Shear studies have been used with much success to map large scale mass distributions in the nearby universe (Van Waerbeke et al., 2013; Massey et al., 2007b). However, because they rely on precise shape measurements, shear faces the practical limitation of an inability to sufficiently resolve sources for lenses more

distant than a redshift of about one (Van Waerbeke et al., 2010).

A third approach to measuring gravitational lensing is through the magnification of background sources, observable either through source size and flux variations (Schmidt et al., 2012; Huff and Graves, 2014), or the resultant modification of source number densities (Ford et al., 2012; Morrison et al., 2012; Hildebrandt et al., 2013, 2011, 2009b; Scranton et al., 2005). Magnification has been recently measured using quasar variability as well (Bauer et al., 2011). Although relative to the shear, magnification will tend to have a lower signal-to-noise for typical low-redshift lenses, the requirement for source resolution is completely removed. This makes magnification competitive for higher redshift lenses, and especially for ground based surveys where atmospheric seeing has a strong influence on image quality.

In this work we adopt the number density approach, known as flux magnification, using Lyman-break galaxies (LBGs) for the lensed background sources. The observed number density of LBGs is altered by the presence of foreground structure, due to the apparent stretching of sky solid angle, and the consequential amplification of source flux. Because of the variation in slope of the LBG luminosity function, magnification can either increase or decrease the number densities of LBGs, depending on their intrinsic magnitudes. By stacking many clusters we can overcome the predominant source of noise - physical source clustering (Hildebrandt et al., 2011).

In Section 4.2 we describe the cluster and background galaxy samples. Section 4.3 lays out the methodology for the measurement and modeling of the magnification signal. We discuss our results in Section 3.4 and conclude in Section 3.5. Throughout this paper we give all distances in physical units, and use a standard  $\Lambda$ CDM cosmology with  $H_0 = 70 \text{ km s}^{-1} \text{ Mpc}^{-1}$ ,  $\Omega_M = 0.3$ , and  $\Omega_\Lambda = 1 - \Omega_M = 0.7$ .

## 3.2 Data

For the magnification results presented in this paper, we are fortunate to work with a very large sample of galaxy cluster candidates and background galaxies in the Canada-France-Hawaii-Telescope Lensing Survey (CFHTLenS<sup>1</sup>; Erben et al. (2013); Hildebrandt et al. (2012)). CFHTLenS is based on the Wide portion of the Canada-France-Hawaii Telescope Legacy Survey, with deep 5 band photometry. The survey is composed of four separate fields, in turn divided into 171 individual pointings, covering a total of  $154 \text{ deg}^2$ .

### 3.2.1 3D-MF Galaxy Clusters

The 3D-Matched-Filter (3D-MF) cluster finding algorithm of Milkeraitis et al. (2010), essentially creates likelihood maps of the sky (in discrete redshift bins) and searches for peaks of significance above the galaxy background. The likelihood is estimated assuming that clusters follow a radial Hubble profile as well as a Schechter luminosity function. A significance peak of  $>3.5\sigma$  is considered a cluster detection, since this reduces below 1% the probability of Gaussian random noise fluctuations mimicking a true cluster. The reader is referred to Milkeraitis et al. (2010) for the details of the 3D-MF algorithm; here we discuss only the essential points relevant to our purposes.

The radial component of the 3D-MF likelihood employs a cutoff radius of 1 Mpc, which was chosen to roughly correspond to the radius  $r_{200}$  of an  $M_{200} \sim 3 \times 10^{13} M_\odot$  cluster. Milkeraitis et al. (2010) motivates this choice by the desire to optimally search for relatively high mass clusters, but notes that this radius will be less ideal for low mass clusters. One should expect that random galaxy interlopers may contaminate the estimation of significance for likelihood peaks corresponding to lower mass clusters. This may be a key factor in explaining

<sup>1</sup>[www.cfhtlens.org](http://www.cfhtlens.org); Data products available at <http://www.cadc-ccda.hia-ihp.nrc-cnrc.gc.ca/community/CFHTLenS/query.html>

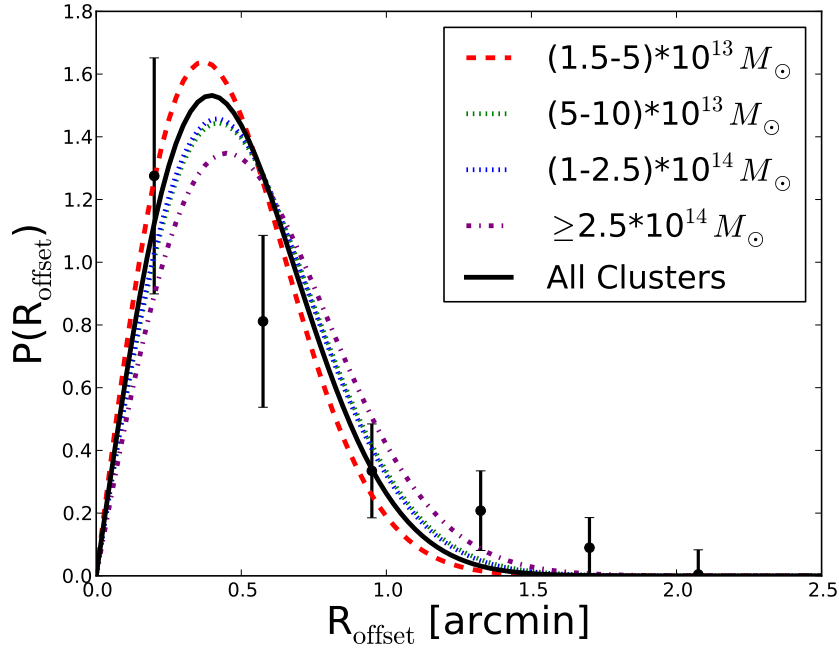


**Figure 3.1:** Modeled Gaussian distribution of radial offsets between defined 3DMF centers and simulated cluster centers. The black points and solid curve is the combined data and best fit for all CFHTLenS clusters combined. The colored curves show the best fit Gaussians for separate mass bins, and colors match the empirical offsets measured and presented in Figure 13 of Milkeraitis et al. (2010). As each of these colored curve fits is consistent with the solid black curve for the entire combined sample, we choose to use this single Gaussian distribution to model miscentering for all clusters.

the wide range of cluster significances conferred upon low mass clusters from simulations, while high mass simulated clusters were assigned significances that correlated strongly with mass (see Figure 10 in Milkeraitis et al., 2010). Because peak significance may therefore not be an ideal mass proxy to use for the full cluster ensemble, in this work we rely upon a measure of the cluster richness, which is discussed in Section 3.2.1 below. Using cluster richness has the added benefit that the mass-richness relation can be measured and used as a scaling relation.

Using the 3D-MF method, a total of 18,036 galaxy cluster candidates (hereafter clusters) have been detected in CFHTLenS, at a significance of  $>3.5\sigma$  above the background. In contrast to previous cluster magnification studies, which have been limited by small number statistics, this huge sample of clusters allows us to pursue multiple avenues of investigation. In particular, we bin the clusters according to both richness and redshift, to recover trends in physical characteristics such as the mass-richness relation, and also investigate halo miscentering as a function of these parameters.

### Cluster Centers

Due to the nature of the method, the defined centers of the 3D-MF clusters, which are located at peaks in the likelihood map, do not necessarily coincide with member galaxies. Hence the defined centers are notably different from many other cluster finders, which commonly choose the brightest cluster galaxy (BCG), the peak in X-ray emission, some type of (possibly luminosity-weighted) average of galaxy positions, or a combination of these, as a measure of the center of a dark matter halo.

**Table 3.1:** Best Fit Gaussian Distributions for the Cluster Miscentering in Figure 3.1.

Mass Range [ $M_\odot$ ]	Color	Best fit $\sigma_{\text{offset}}$ [arcmin]	$\chi^2_{\text{red}}$
$(1.5-5) \times 10^{13}$	red	$0.37 \pm 0.06$	1.8
$(5-10) \times 10^{13}$	green	$0.42 \pm 0.06$	1.4
$(1-2.5) \times 10^{14}$	blue	$0.42 \pm 0.06$	1.2
$\geq 2.5 \times 10^{14}$	purple	$0.45 \pm 0.06$	1.4
$\geq 1.5 \times 10^{13}$	black	$0.40 \pm 0.06$	1.1

The choice of cluster center is always ambiguous, both observationally and in simulations. One wants to know the center of the dark matter distribution, as the point around which to measure a radially-dependent signal. Obviously the dark matter cannot be directly seen, so an observable such as galaxies or X-ray emission must be used (see George et al. (2012) for an excellent review and analysis of cluster centroiding). The chosen center of the cluster can be wrong for several reasons. The observable chosen (e.g. the BCG) may simply be offset from the true center of the dark matter potential. Misidentification of the BCG can be a significant problem for this particular example as well (Johnston et al., 2007).

Perhaps a more interesting source for miscentering comes from the fact that clusters halos are not perfectly spherical, and exhibit substructure and irregularities caused by their own unique mass assembly histories. Especially for very massive halos, which have formed more recently and in many cases are still undergoing mergers and have yet to virialize, we really should not expect a clear center to exist. Following visual inspection, Mandelbaum et al. (2008a) chose to exclude the most massive clusters from their weak lensing analysis for this very reason. Instead of throwing away the highest mass halos in our sample, we include them in this study, but take care to account for possible miscentering effects.

Milkeraitis et al. (2010) tested for centroid offsets in 3D-MF by running the cluster-finder on simulations and comparing detected cluster centers to known centers. The simulations used were the mock catalogs of Kitzbichler and White (2007), which were created from a semi-analytic galaxy catalog (De Lucia and Blaizot, 2007) derived from the Millenium Simulation (Springel et al., 2005). Figure 13 of that work shows the number of clusters detected as a function of distance from true cluster center. Because 3D-MF was optimized to produce cluster catalogs that are as complete as possible (in contrast to, e.g. Gillis and Hudson (2011), which is designed to maximize purity), the trade-off is the presence of some contamination with false-detections, especially at the low mass end.

We use the numbers of clusters at each offset, and the contamination from Milkeraitis et al. (2010), to estimate the probability of radial offsets  $P(R_{\text{offset}})$ . We fit the result for each mass bin with a 2-dimensional Gaussian distribution:

$$P(R_{\text{offset}}) = \frac{R_{\text{offset}}}{\sigma_{\text{offset}}^2} \exp \left[ -\frac{1}{2} \left( \frac{R_{\text{offset}}}{\sigma_{\text{offset}}} \right)^2 \right]. \quad (3.1)$$

This resulting curves are presented in Figure 3.1 (colors are selected to match those in Figure 13 of Milkeraitis et al. (2010)), and for clarity we only show the data points for the bin that combines all clusters. We find consistent fits for the separate mass bins, which we list in Table 1, and therefore use the combined distribution (black curve) to model the effects of miscentering in our measurements.

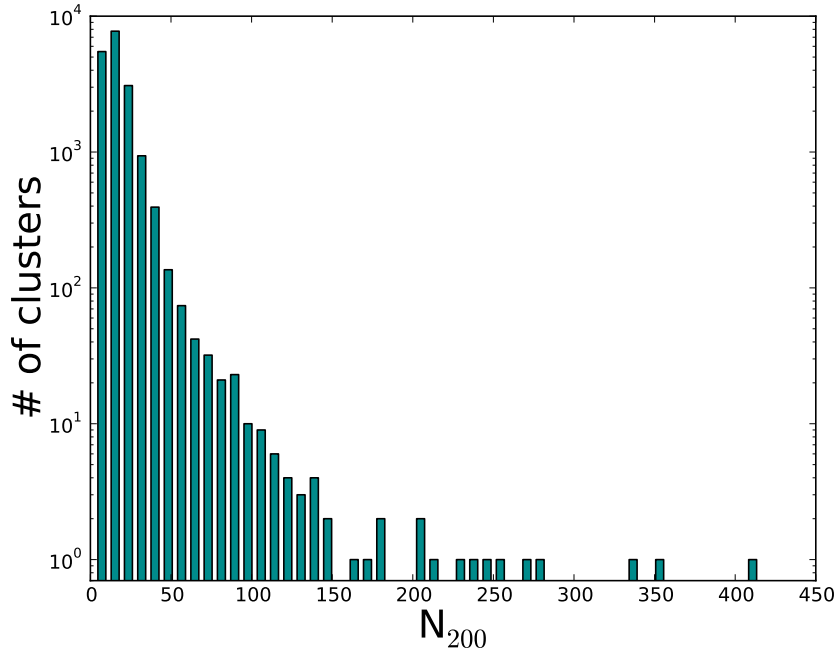


**Figure 3.2:** Distribution of richness ( $N_{200}$ ) values for clusters in this study.

### Cluster Richness

We define the richness parameter  $N_{200}$  in this work to be the number of galaxies within a radius  $r_{200}$ , and redshift  $\Delta z$ , of a cluster candidate center (both points discussed below). Member galaxies are also required to be brighter than  $i$ -band absolute magnitude  $-19.35$ . This cut-off is chosen to correspond to the limiting *apparent* magnitude of CFHTLenS ( $i \sim 24$ ) at the highest redshift clusters that we probe,  $z \sim 1$ . So at the expense of removing many galaxies from the richness count, we hope to largely avoid the effect of incompleteness on the number of galaxies per cluster. Then clusters of the same intrinsic richness at high and low redshift should have comparable observed  $N_{200}$ , within the expected scatter of the mass-richness relation.

For the line-of-sight dimension, we require galaxies to fall within  $\Delta z < 0.08(1+z)$  of the cluster redshift. This  $\Delta z$  is the  $2\sigma$  scatter of photometric redshifts in the CFHTLenS catalog, chosen so that we reduce the probability of galaxies in a cluster being missed due to errors in their photo- $z$  estimation. Of course this comes at the expense of counting galaxies within a quite broad line-of-sight extent, especially for the higher redshift clusters. This effect should cancel out though, since we also use the same  $\Delta z$  range in calculating the galaxy background density, which is subtracted to yield  $N_{200}$  as an overdensity count of cluster galaxy members.

In the plane of the sky, galaxies must lie within a projected radius  $r_{200}$  of the cluster center (defined above).  $r_{200}$  is defined as the radius within which the average density is 200 times the critical energy density of the universe,  $\rho_{crit}(z)$ , evaluated at the redshift of the cluster. However, since  $r_{200}$  itself is unknown, we require some kind of assumption about radius or mass in order to proceed with the galaxy counting. There is no unique way to do this. We begin by making an initial approximation of the masses using a best fit power-law relation between mass and cluster peak significance, for 3D-MF clusters (Milkeraitis, 2011):

$$\log(M_{200}) = 0.124\sigma + \log(10^{14}M_{\odot}) - 1.507. \quad (3.2)$$



As discussed in 3.2.1, 3D-MF tests on simulations suggested that peak significance was a good mass proxy for high, but not low, mass clusters. In light of this, we merely employ the above relation as a starting point for calculating the radii from mass,

$$r_{200} = \left[ \frac{3M_{200}}{4\pi(200)\rho_{crit}(z)} \right]^{1/3}. \quad (3.3)$$

These  $r_{200}$  estimates are then used for counting galaxies for cluster richness. Richness  $N_{200}$  is the variable of choice used as a mass proxy for binning the magnification measurement. The distribution of these richness values is shown in Fig. 2.

### 3.2.2 Sources

We use Lyman-break galaxies (LBGs) as the magnified background sources. LBGs are high-redshift star-forming galaxies (Steidel et al., 1998), that have been successfully employed in past magnification studies (see Hildebrandt et al., 2009b, 2011; Morrison et al., 2012; Ford et al., 2012) due to the fact that their redshift distributions and luminosity functions are reasonably well understood. Knowledge of the intrinsic source luminosity function allows for an interpretation of the magnification signal, which depends sensitively on the slope of the number counts as a function of magnitude. In addition, the high-redshift nature of LBGs is important to reduce redshift overlap between lenses and sources. Any source galaxies in the redshift range of the cluster lenses will contaminate the lensing-induced cross-correlation signal, with correlations due to physical clustering.

The LBG sample is selected with the color selection criteria of Hildebrandt et al. (2009a) (see Sect. 3.2 of that paper). It is composed of 122,144  $u$ -dropouts with  $23 < r \leq 24.5$ , located at redshift  $\sim 3.1$ . We choose this magnitude range to avoid as much potential low-redshift contamination as possible. See Section 3.3.2 for our modeling of the residual contamination. The detailed properties of this LBG population will be described in a forthcoming paper (Hildebrandt et al. in prep.).

## 3.3 Magnification Methodology

### 3.3.1 The Measurement

The magnification factor,  $\mu$ , of a gravitational lens can be expressed in terms of the change from intrinsic ( $n_0$ ) to observed ( $n$ ) differential number counts of background sources:

$$n(m)dm = \mu^{\alpha-1} n_0(m)dm \quad (3.4)$$

(Narayan, 1989). Here  $m$  is apparent magnitude, and  $\alpha \equiv \alpha(m)$  is proportional to the logarithmic slope of the source luminosity function. Depending on the luminosity function's slope in a given magnitude bin, it is possible to observe either an increase or a decrease in source number counts, as demonstrated in Figure 2 of Ford et al. (2012).

In practice the magnification signal is easily measured using the optimally-weighted cross-correlation function of Ménard et al. (2003):

$$w_{\text{opt}}(R) = \frac{S^{\alpha-1}L - S^{\alpha-1}R - \langle \alpha - 1 \rangle LR}{RR} + \langle \alpha - 1 \rangle. \quad (3.5)$$

In this expression, the terms are normalized pair counts in radial bins, where  $L$  stands for the lenses, and  $S^{\alpha-1}$  are the optimally-weighted sources.  $R$  represents objects from a random catalog more than ten times the size of the source catalog, with the same masks applied.

In order to determine the optimal weight factor  $\alpha - 1$ , for both the measurement and the interpretation, we require knowledge of the source luminosity function. As done in Ford et al. (2012) we determine the LBG luminosity function slope from the Schechter Function (Schechter, 1976), giving

$$\alpha = 2.5 \frac{d}{dm} \log n_0(m) = 10^{0.4(M^* - M)} - \alpha_{LF} - 1, \quad (3.6)$$

and rely on externally measured luminosity functions for the characteristic magnitude  $M^*$  and faint end slope  $\alpha_{LF}$ . We use the LBG luminosity function of van der Burg et al. (2010), measured using much deeper data from the CFHTLS Deep fields. For  $u$ -dropouts  $M^*$  is -20.84 and  $\alpha_{LF}$  is -1.6. Thus every source galaxy is assigned a weight factor of  $\alpha - 1$  according to its absolute magnitude  $M$ .

The magnification signal,  $w_{\text{opt}}(R)$ , is measured in logarithmic radial bins of physical range 0.09 – 4 Mpc (in contrast to angle), so that we can stack clusters at different redshifts without mixing very different physical scales. Each cluster's signal is measured separately before stacking the measured  $w_{\text{opt}}(R)$ , and full covariance matrices are estimated from the different measurements.

### 3.3.2 The Modeling

The magnification is a function of the halo masses, and to first order it is proportional to the convergence  $\kappa$ . In this work, however, we will use the full expression for  $\mu$  to account for any deviations from weak lensing in the inner regions of the clusters:

$$\mu = \frac{1}{(1 - \kappa)^2 - |\gamma|^2} \quad (3.7)$$

(Bartelmann and Schneider, 2001).

We assume a spherical Navarro-Frenk-White (NFW) model (Navarro et al., 1997) for the dark matter halos, along with the mass-concentration relation of Prada et al. (2012). The convergence is modeled as the sum of three terms,

$$\kappa = \left[ p_{\text{cc}} \Sigma_{\text{NFW}} + (1 - p_{\text{cc}}) \Sigma_{\text{NFW}}^{\text{smoothed}} + \Sigma_{2\text{halo}} \right] / \Sigma_{\text{crit}}, \quad (3.8)$$

where  $p_{\text{cc}}$  is the fraction of clusters correctly centered (i.e. with  $R_{\text{offset}} = 0$ ), and  $\Sigma_{\text{crit}}(z)$  is the critical surface mass density at the lens redshift. The expression for the shear,  $\gamma$ , is identical with  $\kappa \rightarrow \gamma$ , and  $\Sigma \rightarrow \Delta \Sigma$ . Note that the first term in Equation 4.16 is equivalent to adding a delta function to the miscentered distribution of Figure 3.1, to represent clusters with perfectly-identified centers. As discussed in Section 3.4, the fits do not give strong preference to miscentering in the measurement, but in future work (in particular with weak lensing shear) it will be useful to constrain the degree of miscentering using the data, instead of relying solely on simulations.

We assume both lenses and sources are located at known discrete redshifts. This is  $z \sim 3.1$  for the LBGs. Since they are at very high redshift the effect of any small offsets from this has negligible effect on the angular diameter distance, the relevant distance measure for lensing. The clusters, on the other hand, have redshift uncertainties of 0.05 (due to the shifting redshift slices employed by 3D-MF (Milkeraitis et al., 2010)). This translates into an uncertainty on the mass estimates ranging from less than a percent up to  $\sim 17\%$  (depending on cluster  $z$ ), and is included in the reported mass estimates.

$\Sigma_{\text{NFW}}$  is the standard surface mass density for a perfectly centered NFW halo, calculated using expressions for  $\kappa$  (and  $\gamma$ ) in Wright and Brainerd (2000).  $\Sigma_{\text{NFW}}^{\text{smoothed}}$  on the other hand, is the expected surface mass density measured for a miscentered NFW halo:

$$\Sigma_{\text{NFW}}^{\text{smoothed}}(R) = \int_0^\infty \Sigma_{\text{NFW}}(R|R_{\text{offset}})P(R_{\text{offset}})dR_{\text{offset}}. \quad (3.9)$$

The distribution of offsets  $P(R_{\text{offset}})$  is given by Equation 3.1, and the other factor in the integrand is

$$\Sigma_{\text{NFW}}(R|R_{\text{offset}}) = \frac{1}{2\pi} \int_0^{2\pi} \Sigma_{\text{NFW}}(R')d\theta, \quad (3.10)$$

where  $R' = \sqrt{R^2 + R_{\text{offset}}^2 + 2RR_{\text{offset}}\cos\theta}$  (Yang et al., 2006).

The 2-halo term  $\Sigma_{\text{2halo}}$  accounts for the fact that the halos we study do not live in isolation, but are clustered as all matter in the universe is. We account for neighboring halos following the prescription of Johnston et al. (2007):

$$\Sigma_{\text{2halo}}(R, z) = b_l(M_{200}, z)\Omega_M\sigma_8^2 D(z)^2 \Sigma_l(R, z) \quad (3.11)$$

$$\Sigma_l(R, z) = (1+z)^3 \rho_{\text{crit},0} \int_{-\infty}^{\infty} \xi\left((1+z)\sqrt{R^2 + y^2}\right) dy \quad (3.12)$$

$$\xi(r) = \frac{1}{2\pi^2} \int_0^\infty k^2 P(k) \frac{\sin kr}{kr} dk \quad (3.13)$$

Here small  $r$  is comoving distance,  $D(z)$  is the growth factor,  $P(k)$  is the linear matter power spectrum, and  $\sigma_8$  is the amplitude of the power spectrum on scales of  $8 h^{-1}\text{Mpc}$ . For the lens bias factor  $b_l(M_{200}, z)$  we use Equation 5 of Seljak and Warren (2004).

### Composite-Halo Fits

The part of the optimal correlation function which is caused by gravitation lensing is related to the magnification contrast  $\delta\mu \equiv \mu - 1$  through

$$w_{\text{lensing}}(R) = \frac{1}{N_{\text{lens}}} \sum_{i=1}^{N_{\text{lens}}} \langle (\alpha - 1)^2 \rangle_i \delta\mu(R, M_{200})_i. \quad (3.14)$$

Here the sum is over the number of lenses in a given stacked measurement, and  $\langle (\alpha - 1)^2 \rangle_i$  refers to the average of the weight factor squared in the pointing of a given cluster.

We perform composite-halo fits using the above prescription, in which we allow for the fact that the clusters in a given measurement have a range of masses and redshifts. We do not fit a single average mass. Instead, we calculate  $\delta\mu(R, M_{200})_i$  for each individual cluster using a scaling relation between mass and richness,

$$M_{200} = M_0 \left( \frac{N_{200}}{20} \right)^\beta. \quad (3.15)$$

The fit parameters are the normalization,  $M_0$ , and (log-) slope,  $\log\beta$ , of the assumed power-law relation. From

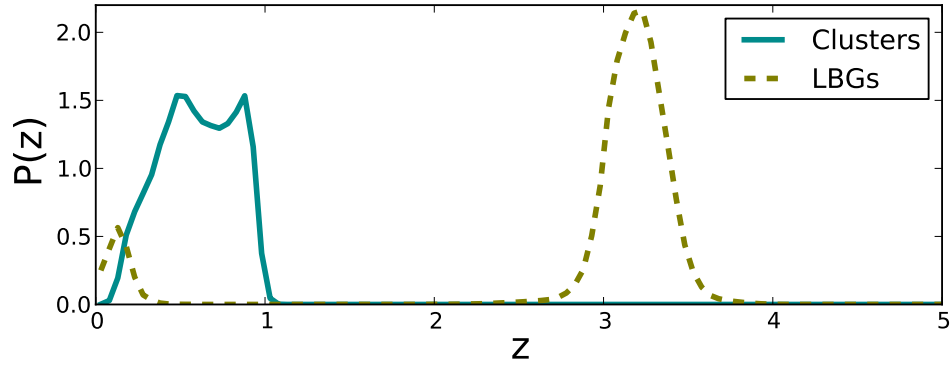


**Figure 3.3:** Redshift probability distribution functions for the clusters and the LBG sources. Low-redshift contamination of the LBGs will lead to physical clustering correlations where overlap with the cluster redshifts occurs.

this we calculate the optimal correlation  $w_{\text{opt}}(R)$  according to Equation 3.14. The best-fit relation is determined by minimizing  $\chi^2$ , which is calculated using the full covariance matrix. We apply the correction factor from Hartlap et al. (2007) to the inverse covariance matrix; this corrects for a known bias (related to the number of data sets and bins) which would otherwise lead to our error bars being too small.

### LBG Contamination

An important source of systematic error for magnification comes from low-redshift contamination of the sources, leading to physical clustering between the lens and source populations. The cross-correlation that results from contamination can easily overwhelm the measurement of magnification, making redshift overlap far more important for magnification than for shear. Past studies sought to minimize this effect, for example by checking for the negative cross-correlation that should exist between lenses and very faint sources with shallow number count (Ford et al., 2012; Hildebrandt et al., 2009b). Here we incorporate this clustering into the model, using a similar approach to Hildebrandt et al. (2013).

Figure 3.3 shows the redshift probability distributions,  $P(z)$ , for the clusters and the LBGs. The LBG redshift distribution is based on the stacked posterior  $P(z)$  put out by the BPZ redshift code (for details on the CFHTLenS photo- $z$  see Hildebrandt et al., 2012). Since the BPZ prior is only calibrated for a magnitude limited sample of galaxies we can not expect the stacked  $P(z)$  to reflect the real redshift distribution of the color-selected LBGs. Hence we use the location and shape of the primary (high- $z$ ) and secondary (low- $z$ ) peaks but adjust their relative heights separately. This can be done with a cross-correlation technique similar to Newman (2008). Details of this technique will be presented in Hildebrandt et al. (in prep.).

Despite our efforts to avoid contamination, there is obviously some redshift overlap with the clusters. We use the products of the lens and source  $P(z)$  to define selection functions, and calculate the expected angular correlations using the code from Hamana et al. (2004). The weighted correlation function that we measure is the sum of the correlations due to lensing magnification and clustering contamination:

$$w_{\text{opt}}(R, z) = f_{\text{lensing}} w_{\text{lensing}} + f_{\text{clustering}} w_{\text{clustering}}. \quad (3.16)$$

Note that  $f_{\text{lensing}} + f_{\text{clustering}} \leq 1$ , since some of the contaminants may be neither in the background and lensed, nor close enough in redshift to be clustered with the lenses.

The clustering contamination fraction  $f_{\text{clustering}}(z)$  for each cluster redshift is defined as the fraction of each source  $P(z)$  that lies within 0.1 in redshift (twice the cluster redshift uncertainty). The part of the source  $P(z)$  that lies at higher redshift than the lens is then the lensed fraction  $f_{\text{lensing}}(z)$ , and the part at lower redshift (i.e. in *front* of the lens) has no contribution to the signal.

The factor  $f_{\text{clustering}}(z)$  itself is generally very small for the LBGs used in this work, only really non-negligible for cluster redshifts  $z \sim 0.2$ - $0.3$ , which can be seen in Figure 3.3. The more significant effect on the estimated masses is that  $f_{\text{lensing}}(z) \sim 0.9$  across all redshift bins, because about 10% of the sources are not really being lensed. We tested our results for robustness against uncertainties in the contamination fraction. When we vary the total low- $z$  contamination fraction by  $\pm 1\sigma$  ( $\sim 4\%$ ), the best fit cluster mass estimates remain within the stated error bars.

We explore three ways of determining  $w_{\text{clustering}}$ . Because of the weighting applied to LBGs in our measurement (which is optimal for the lensed sources, and should suppress contributions from redshift overlap), there will always be a prefactor of  $\langle \alpha - 1 \rangle$  in each estimation of clustering. The first method uses the dark matter angular auto-correlation,  $w_{\text{dm}}$ , and estimates of the galaxy and cluster bias to calculate:

$$w_{\text{clustering}}(R, z) = \langle \alpha - 1 \rangle b_l b_s w_{\text{dm}}(R, z). \quad (3.17)$$

We set the bias factor for the galaxy contaminants  $b_s=1$  for this analysis, which is reasonably consistent with the bias relation of Seljak and Warren (2004) that is employed for the cluster bias ( $b_l$ ).

We also calculate both the 1- and 2-halo terms for NFW halos,  $w_{1\text{halo}}$  and  $w_{2\text{halo}}$  (again using the code and methods described in Hamana et al., 2004). Here the expression for physical clustering takes the form:

$$w_{\text{clustering}}(R, z) = \langle \alpha - 1 \rangle b_s [w_{1\text{halo}}(R, z) + w_{2\text{halo}}(R, z)]. \quad (3.18)$$

This method requires knowledge of the occupation distribution of the low- $z$  galaxy contaminants in the cluster dark matter halos, which is not well determined. As a first approximation we use the simple power-law form described in Hamana et al. (2004),

$$N_g(M) = \begin{cases} (M/M_1)^\alpha & \text{for } M > M_{\text{min}} \\ 0 & \text{for } M < M_{\text{min}} \end{cases}. \quad (3.19)$$

Since these parameters are unknown, we use the values for  $M_1$  and  $\alpha$  measured for galaxies in the SDSS (see Table 3 of Zehavi et al., 2011). We choose  $M_{\text{min}}$  to correspond to the minimum mass measured for cluster halos, and assume that halos above this mass always host a detected cluster. As a final check, we also ask what the clustering signal would be if every halo above  $M_{\text{min}}$  hosted both a cluster and a single low- $z$  galaxy contaminant (so that  $N_g = 1$  for  $M > M_{\text{min}}$ ).

This final method yields the largest estimates of  $w_{\text{clustering}}$ , and therefore a smaller estimate of cluster masses. The former (using SDSS parameters) gives the highest mass estimates, and the simple biasing approach of Equation 3.17 yields intermediate results. We use the range of these results to estimate an uncertainty in mass estimates coming from lack of knowledge about the nature of the low- $z$  galaxies that contaminate our LBG source sample. This additional systematic error affects only the clusters at low redshift, where the source and lens  $P(z)$  distributions overlap, and is reported on the mass estimates given in Table 3. All best fit mass values reported in the tables of this work are calculated using the contamination approach of Equation 3.17, since this

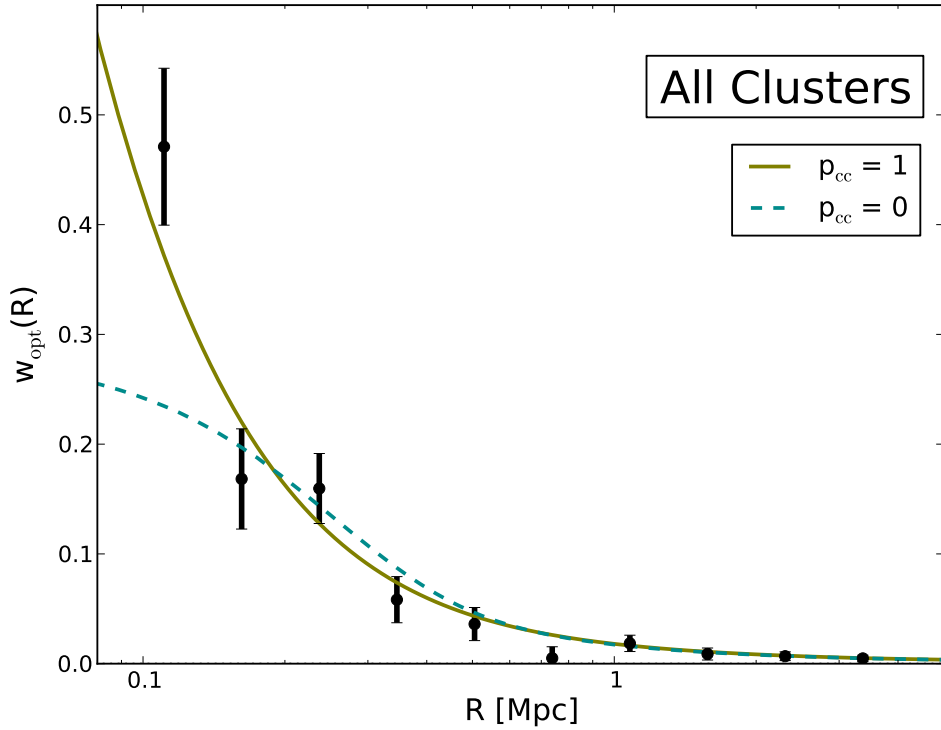


**Figure 3.4:** Optimal cross-correlation signal measured for the entire stacked sample of 18,024 clusters. The model fits are both composite-NFW (see text for all terms in the fit). The solid line assumes the clusters are perfectly centered on the peak likelihood of the 3DMF cluster detection, while the dashed line includes the effects of cluster miscentering.

method relied on the fewest assumptions about the nature of the galaxy contaminants.

Accounting for redshift distributions in this particular source sample effectively means that cluster masses are *higher* than one would naively guess by fitting for only the magnification signal. However, note that in a case with more significant redshift overlap, so that  $f_{\text{clustering}}$  was large, the opposite statement would be true, and mass estimates that included the full  $P(z)$  distribution would be smaller than the naive magnification-only approach. These are important effects to consider, and future flux magnification studies should be careful to use full redshift distributions in modeling the measured signal.

### 3.4 Results

Stacking the entire set of 18,036 clusters gives a total significance of  $9.7\sigma$  for the combined detection, shown in Figure 3.4. The perfectly centered model is a better fit to the overall measurement, with  $\chi^2_{\text{red}} \sim 1.2$ , while the miscentered model gives  $\chi^2_{\text{red}}$  of 2.3. For both models, there are two free parameters ( $M_0$  and  $\log \beta$ ), leading to 8 degrees of freedom. To investigate miscentering and mass-richness scaling, we divide the clusters into six richness bins, and measure the optimal cross-correlation in each.

We measure the characteristic signature of magnification in every richness bin with significances between  $4.6$  and  $5.9\sigma$ . These results are shown in Figure 3.5, where we try fitting both a perfectly centered model ( $p_{\text{cc}} = 1$ ) and a model where every cluster is affected by centroid offsets ( $p_{\text{cc}} = 0$ ). Details of the fits, including reduced  $\chi^2$  and the average of the best fit mass values  $\langle M_{200} \rangle$ , are given in Table 3.2.

The lowest mass (richness) bin is not well fit by either model. Overall there is not a strong preference for

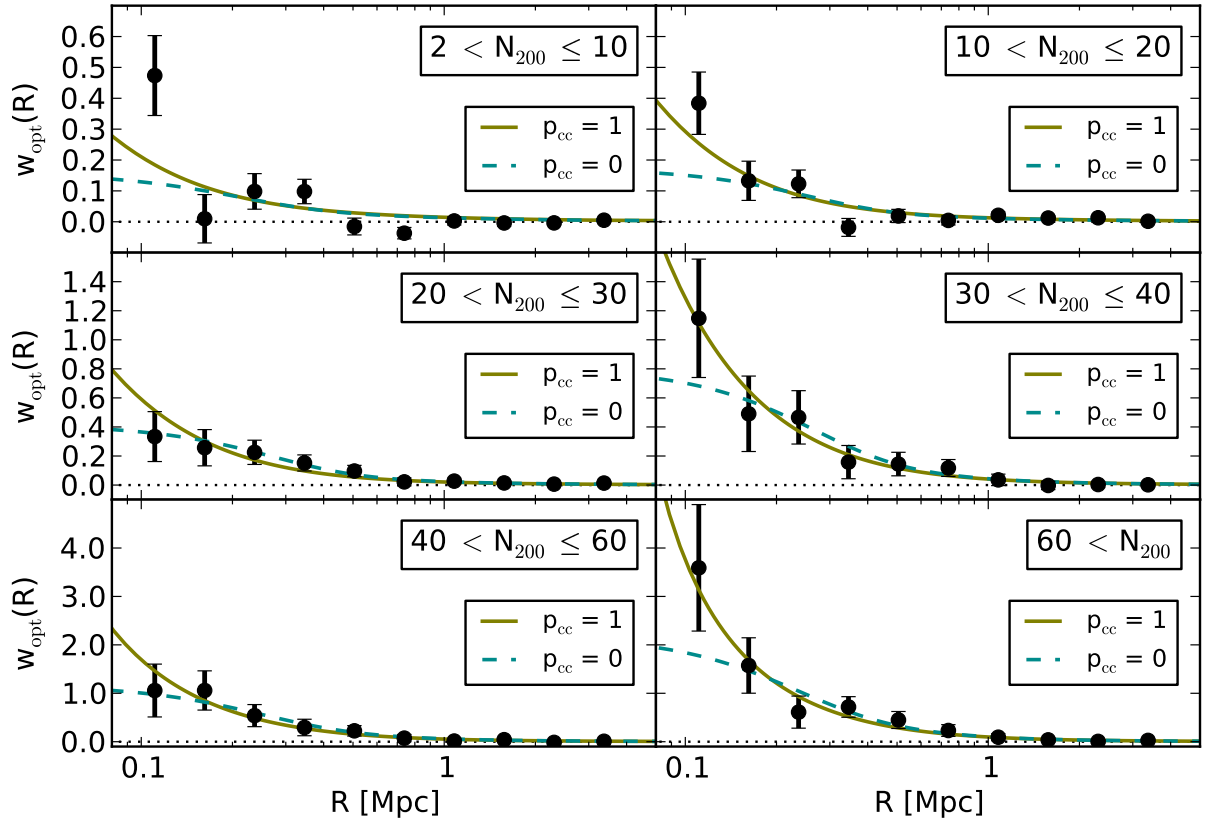


**Figure 3.5:** Optimal cross-correlation signal measured for each  $N_{200}$  (richness) bin. Two composite-NFW fits are shown. The solid curve assumes clusters are perfectly centered, while the dashed curve accounts for cluster miscentering, using the gaussian offset distribution modeled in Figure 3.1 and discussed in Section 3.3.2.

either perfectly centered ( $p_{cc} = 1$ ) or miscentered ( $p_{cc} = 0$ ) clusters, and both are reasonably good fits. Generally, the miscentered model yields slightly higher masses for the clusters (though it is sensitive to the shape of the data), due to the Gaussian smoothing applied, which lowers the model amplitude in the innermost regions. However this is easily within the uncertainty on the mass estimates, so the results are in agreement.

The issue of cluster miscentering is interesting in its own right as discussed in Section 3.2.1. It is tempting to try and fit for the parameter  $p_{cc}$ , describing the fraction that are actually correctly centered, or else for the miscentering Gaussian width  $\sigma_{\text{offset}}$ , as done in Johnston et al. (2007). The issue here is a strong degeneracy between  $p_{cc}$ ,  $\sigma_{\text{offset}}$ , and cluster concentration. Increasing the number of clusters that have offset centers produces essentially the same results as leaving  $p_{cc}$  fixed and increasing  $\sigma_{\text{offset}}$ , an effect that can be mimicked by a lower concentration in the NFW model. We run the risk of overfitting to the results.

In fact, Johnston et al. (2007) found very little constraining power on the miscentering width and the fraction of miscentered MaxBCG clusters, and applied strong priors to these distributions. George et al. (2012) performed an extensive weak lensing miscentering study of groups in the Cosmological Evolution Survey (COSMOS), and chose to forgo the additional parameter  $p_{cc}$ , as they achieved sufficiently good fits without it. Mandelbaum et al. (2008a) performed a lensing analysis of the MaxBCG clusters, and found that including miscentering effects with the Johnston et al. (2007) prescription strongly affected the resultant fits for concentration, again asserting the degeneracies of these parameters. Mandelbaum et al. (2008a) conclude that this

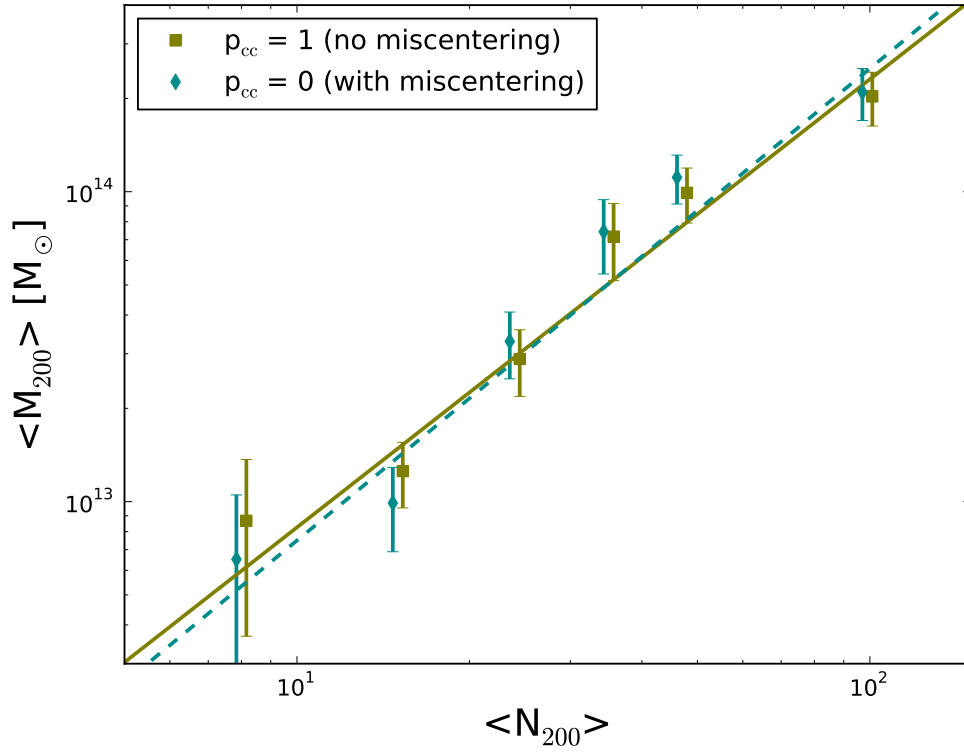


**Figure 3.6:** Cluster mass-richness relation, using the same  $N_{200}$  bins as in Figures 3.5. Power law fits to the data are presented for both cases of with (blue diamonds and dashed line) and without (green squares and solid line) the effects of miscentering. Points are slightly offset horizontally for clarity.

method of accounting for miscentering depends heavily on the mock catalogs from which the input parameters are generated, and in the case of MaxBCG clusters likely overcompensates.

In a forthcoming paper, we will present weak lensing shear measurements of these clusters, as well as a more detailed investigation of the centroiding. Shear, being proportional to the differential surface mass density, is more affected by offset centers than magnification (Johnston et al., 2007), and will be a better probe of miscentering.

### 3.4.1 The Mass-Richness Relation

We observe a prominent scaling of best fit mass to richness, across the six richness bins (although the first two bins do generally have overlapping error bars). We plot this trend in Figure 3.6, showing the average of the fit masses as a function of average cluster richness in each bin. Note that the distribution of  $N_{200}$  in a bin is not uniform, and in the case of the highest richness bin the distribution is highly skewed (see Figure 3.2).

We fit a simple power-law, Equation 3.15, to these points, using the same plotted color and line schemes for perfectly centered and miscentered clusters. For this cluster sample, we find the best fit gives the normalization and slope of the mass-richness relation to be

$$M_0 = (2.3 \pm 0.2) \times 10^{13} M_{\odot}, \beta = 1.4 \pm 0.1 \quad (3.20)$$



for the perfectly centered  $p_{\text{cc}} = 1$  case, and

$$M_0 = (2.2 \pm 0.2) \times 10^{13} M_{\odot}, \beta = 1.5 \pm 0.1 \quad (3.21)$$

for the miscentered  $p_{\text{cc}} = 0$  case. The reduced  $\chi^2$  are 0.9 and 1.7, respectively (4 degrees of freedom), and there is good agreement between the two different centering scenarios explored here.

**Table 3.2:** Details of fits for richness-binned measurements in Figure 3.5. We list the richness range selected, the number of clusters in that bin, the detection significance, the average richness of the bin, and the mass estimates and reduced  $\chi^2$  for both the centered and miscentered models fit to the data. Note that the average mass given is not the value fit itself, but the average of all resulting masses fit using the composite-halo approach discussed in Section 3.3.2.

Richness	# Clusters	Significance	$\langle N_{200} \rangle$	$p_{cc}=1: \langle M_{200} \rangle$	$\chi_{red}^2$	$p_{cc}=0: \langle M_{200} \rangle$	$\chi_{red}^2$
$2 < N_{200}$	18036	$9.7\sigma$	17	$(2.0 \pm 0.3) \times 10^{13} M_{\odot}$	1.2	$(1.8 \pm 0.3) \times 10^{13} M_{\odot}$	2.3
$2 < N_{200} < 10$	4453	$5.3\sigma$	8	$(0.9 \pm 0.5) \times 10^{13} M_{\odot}$	3.0	$(0.7 \pm 0.4) \times 10^{13} M_{\odot}$	3.2
$10 < N_{200} < 20$	9398	$5.9\sigma$	15	$(1.3 \pm 0.3) \times 10^{13} M_{\odot}$	1.6	$(1.0 \pm 0.3) \times 10^{13} M_{\odot}$	2.2
$20 < N_{200} < 30$	2967	$5.4\sigma$	24	$(2.9 \pm 0.7) \times 10^{13} M_{\odot}$	0.7	$(3.3 \pm 0.8) \times 10^{13} M_{\odot}$	0.3
$30 < N_{200} < 40$	695	$5.0\sigma$	35	$(7 \pm 2) \times 10^{13} M_{\odot}$	0.3	$(7 \pm 2) \times 10^{13} M_{\odot}$	0.5
$40 < N_{200} < 60$	351	$4.6\sigma$	47	$(1.0 \pm 0.2) \times 10^{14} M_{\odot}$	0.4	$(1.1 \pm 0.2) \times 10^{14} M_{\odot}$	0.3
$60 < N_{200}$	172	$5.5\sigma$	99	$(2.0 \pm 0.4) \times 10^{14} M_{\odot}$	0.5	$(2.1 \pm 0.4) \times 10^{14} M_{\odot}$	0.6

**Table 3.3:** Details of fits for redshift-binned measurements in Figure 3.8. We list the same bin properties and fits given in Table 3.2, as well as  $f_{clustering}$ , which is the total fraction of LBGs expected to lie within  $\Delta z \sim 0.1$  of the cluster  $z$ .

Redshift	$f_{clustering}$	Clusters	Significance	$\langle N_{200} \rangle$	$p_{cc}=1: \langle M_{200} \rangle$	$\chi_{red}^2$	$p_{cc}=0: \langle M_{200} \rangle$	$\chi_{red}^2$
$z \sim 0.2$	0.07	1157	$12.5\sigma$	11.6	$(9 \pm 2 \pm 2^{sys}) \times 10^{13} M_{\odot}$	3.6	$(9 \pm 2 \pm 2^{sys}) \times 10^{13} M_{\odot}$	3.4
$z \sim 0.3$	0.02	1515	$8.0\sigma$	14.4	$(6 \pm 1 \pm 1^{sys}) \times 10^{13} M_{\odot}$	2.2	$(6 \pm 1 \pm 1^{sys}) \times 10^{13} M_{\odot}$	2.1
$z \sim 0.4$	$3 \times 10^{-3}$	2242	$4.6\sigma$	15.2	$(1.9 \pm 0.7) \times 10^{13} M_{\odot}$	1.4	$(1.6 \pm 0.7) \times 10^{13} M_{\odot}$	1.6
$z \sim 0.5$	$4 \times 10^{-4}$	2932	$4.0\sigma$	15.9	$(0.3 \pm 0.4) \times 10^{13} M_{\odot}$	1.9	$(0.2 \pm 0.5) \times 10^{13} M_{\odot}$	1.9
$z \sim 0.6$	$1 \times 10^{-4}$	2455	$4.6\sigma$	18.0	$(2.2 \pm 0.8) \times 10^{13} M_{\odot}$	1.5	$(2.0 \pm 0.8) \times 10^{13} M_{\odot}$	1.6
$z \sim 0.7$	$2 \times 10^{-5}$	2331	$4.5\sigma$	19.3	$(1.2 \pm 0.7) \times 10^{13} M_{\odot}$	1.7	$(1.1 \pm 0.7) \times 10^{13} M_{\odot}$	1.9
$z \sim 0.8$	$2 \times 10^{-5}$	2364	$4.9\sigma$	19.9	$(2.5 \pm 0.9) \times 10^{13} M_{\odot}$	1.5	$(2.2 \pm 0.9) \times 10^{13} M_{\odot}$	1.7
$z \sim 0.9$	$2 \times 10^{-5}$	3040	$2.6\sigma$	17.6	$(0.5 \pm 0.5) \times 10^{13} M_{\odot}$	0.6	$(0.3 \pm 0.6) \times 10^{13} M_{\odot}$	0.8

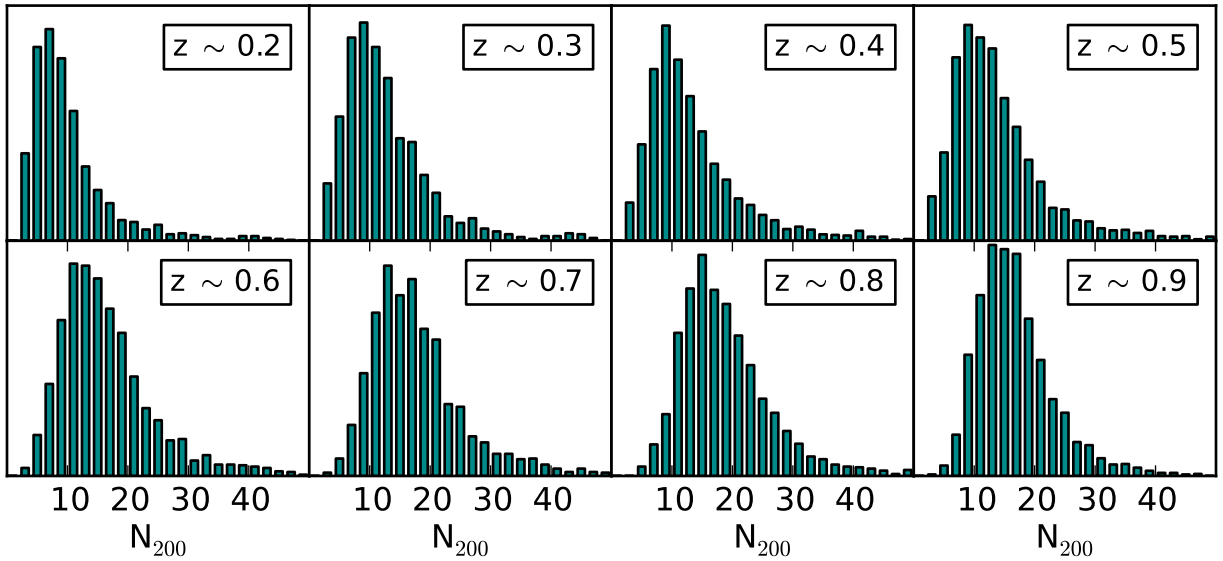


**Figure 3.7:**  $N_{200}$  distributions as a function of cluster redshift.

It is difficult to directly compare the results for the mass-richness relation in this work to other studies. The main reason is that the richness  $N_{200}$  we use is different than other definitions, which often count only red-sequence galaxies. Some uncertainty exists in the measure of richness as well, which we do not include in the analysis. Alternative measures of cluster richness would yield different scaling relations. Another factor is the cluster sample, which was compiled using a novel cluster-finder, and may well have different characteristics than other samples in the literature. In a follow-up paper we will present a shear analysis of the CFHTLenS clusters, and compare the mass-richness relation obtained using that complementary probe of halo mass.

### 3.4.2 Redshift Binning

Finally, we investigate the magnification as a function of redshift. We stack clusters of all richnesses, at each redshift in the catalog,  $0.2 \leq z \leq 0.9$ , and measure the optimal correlations in each. This is displayed in Figure 3.8. We observe a steady decrease in measured signal as the cluster redshift increases from  $z \sim 0.2$  to  $0.5$ , then roughly consistent measurements from  $0.6 \leq z \leq 0.8$ , followed by rather low signal at  $z \sim 0.9$ .

The  $N_{200}$  distributions in Figure 3.7 show that these trends cannot be caused by deviations in richness between these different cluster redshifts. This is difficult to reconcile with the clear mass-richness scaling observed when all redshifts are combined. Table 3 shows that detection significance for each redshift bin is more tightly linked to mass than the  $\langle N_{200} \rangle$ . Perhaps the richness estimates used in this work are not optimized for use as a mass proxy at all redshifts. Another possibility is that we have not correctly accounted for redshift overlap between samples. If the contamination fraction is higher than estimated, this could lead to a boost in correlation strength at low redshift, as well as a depletion at higher redshift. However it is still very difficult to explain the anomalously low measurement at intermediate redshift,  $z \sim 0.5$ , with this reasoning.

One factor that we have not accounted for is possible cluster false detections in our sample. Since 3D-MF was optimized to produce cluster catalogs that are as complete as possible, false detection rates could be quite high. In particular, we would expect these rates to increase at high redshift, which would also weaken those measured correlations. We note in particular that cluster redshift bins  $z \sim 0.5$  and  $0.9$ , which yield relatively

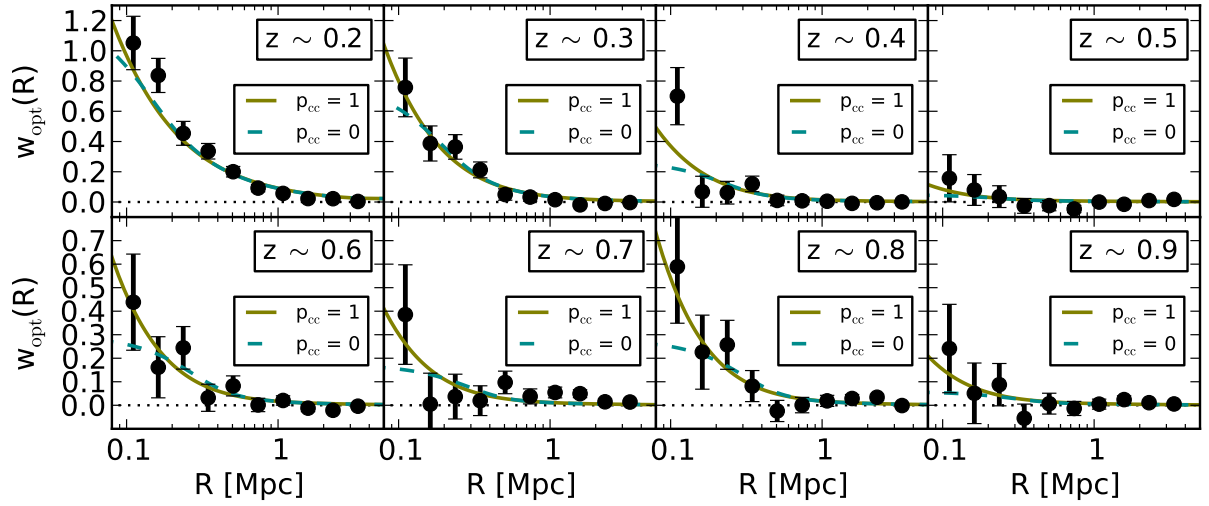


**Figure 3.8:** Optimal correlation for clusters binned in redshift.

low cluster masses, are seen in Figure 3.3 to have excess numbers of detected clusters, possibly an indication of higher false detection rates at these redshifts.

### 3.5 Conclusions

We present the most significant magnification-only cluster measurement to date, at  $9.7\sigma$ . A sample of 18,036 cluster candidates has been detected using the 3D-MF technique in the  $\sim 154 \text{ deg}^2$  CFHTLenS survey. In this analysis we have investigated the mass of cluster dark matter halos, from flux magnification, as a function of both richness and redshift. A forthcoming paper will present the weak lensing shear analysis of these clusters as well.

We fit a composite-NFW model that accounts for the full redshift and mass ranges of the cluster sample, as well as redshift overlap with low- $z$  source contaminants, cluster halo miscentering, and the 2-halo term. We find that the entire cluster sample is marginally better fit by the model that does not include miscentering, but do not see a strong preference either way across richness bins. In the future, shear measurements, which are more sensitive to miscentering, may illuminate this aspect of the investigation.

We observe a strong scaling between measured mass and cluster richness, and fit a simple power-law relation to the data. The two miscentering models explored in this work yield consistent values for the normalization and slope of the mass-richness relation.

We have attempted to account for the contamination of our background sources with low- $z$  galaxies. This is a serious systematic effect for magnification, as redshift overlap between lenses and sources will lead to physical clustering correlations, swamping the lensing-induced correlations that we want to measure. We use the full stacked redshift probability distributions for the lens and source populations, and include the expected clustering contribution in our model. In spite of this we see unexpected features in the redshift-binned measurements. Part of the reason could come from cluster false detections, which can be high for the 3D-MF method which is optimized for completeness. Another contribution could come from errors in the source redshift distributions. Accounting for redshift overlap is imperative if significant overlap exists between the lens and source distributions, or else mass estimates can end up very biased.

This is the first analysis presented of the 3D-MF clusters in CFHTLenS, but much more science is left to do with the sample. In particular, a more thorough investigation of the miscentering problem will be carried out in the forthcoming shear analysis, where it will be possible to compare different candidate centers. Another interesting question is whether dust can be detected on cluster scales by simultaneously measuring the chromatic extinction along with flux magnification. Finally different background source samples may be employed to improve signal-to-noise, but only if their redshift distributions can be well determined. We leave these tasks to future work.

This work has been an important step in the development of weak lensing magnification measurements, and the progression from signal detection to science. Many upcoming surveys will benefit from the inclusion of magnification in their lensing programs, as the technique offers a very complimentary probe of large scale structure. Since measuring flux magnification is not a strong function of image quality, it is especially useful for ground-based surveys which must deal with atmospheric effects. Next generation surveys like the Large Synoptic Survey Telescope (LSST), the Wide-Field Infrared Survey Telescope (WFIRST), and Euclid, will have greater numbers of sources, and improved redshift probability distribution estimates, so we can expect future magnification studies to yield important contributions to weak lensing science and cosmology.

## Chapter 4

# CFHTLenS: A Weak Lensing Shear Analysis of the 3D-Matched-Filter Galaxy Clusters

We present the cluster mass-richness scaling relation calibrated by a weak lensing analysis of  $>18000$  galaxy cluster candidates in the Canada-France-Hawaii Telescope Lensing Survey (CFHTLenS). Detected using the 3D-Matched-Filter cluster-finder of Milkeraitis et al., these cluster candidates span a wide range of masses, from the small group scale up to  $\sim 10^{15}M_{\odot}$ , and redshifts  $0.2 \leq z \leq 0.9$ . The total significance of the stacked shear measurement amounts to  $54\sigma$ . We compare cluster masses determined using weak lensing shear and magnification, finding the measurements in individual richness bins to yield  $1\sigma$  compatibility, but with magnification estimates biased low. This first direct mass comparison yields important insights for improving the systematics handling of future lensing magnification work. In addition, we confirm analyses that suggest cluster miscentring has an important effect on the observed 3D-MF halo profiles, and we quantify this by fitting for projected cluster centroid offsets, which are typically  $\sim 0.4$  arcmin. We bin the cluster candidates as a function of redshift, finding similar cluster masses and richness across the full range up to  $z \sim 0.9$ . We measure the 3D-MF mass-richness scaling relation  $M_{200} = M_0(N_{200}/20)^{\beta}$ . We find a normalization  $M_0 \sim (2.7^{+0.5}_{-0.4}) \times 10^{13}M_{\odot}$ , and a logarithmic slope of  $\beta \sim 1.4 \pm 0.1$ , both of which are in  $1\sigma$  agreement with results from the magnification analysis. We find no evidence for a redshift-dependence of the normalization. The CFHTLenS 3D-MF cluster catalogue is now available at [cfhtlens.org](http://cfhtlens.org).

### 4.1 Introduction

The evolution of large scale structure is overwhelmingly driven by the invisible components which make up the majority of the present day energy density of the Universe. In order to probe these structures we are forced to rely on biased tracers of the underlying density field that we can actually observe, such as galaxies. Large galaxy cluster surveys are invaluable in providing sufficient statistics for classifying and analysing the most massive gravitationally bound systems that have had time to form in our cosmic history. In addition to providing a cosmological probe, they are interesting laboratories for the evolution of individual galaxies and the intracluster medium (Voit, 2005).

Several methods have been developed for identifying clusters in optical galaxy surveys, including the red sequence technique (Gladders and Yee, 2000), density maps (Adami et al., 2010), redMaPPer (Rykoff et al., 2014), and matched-filter methods (Postman et al., 1996). An extension of the latter, 3D-Matched-Filter (3D-

MF), is described in Milkeraitis et al. (2010) and used in this work. This cluster finder attempts to circumvent the common issue of line-of-sight projections by using photometric redshift information to identify clusters in redshift slices. Beyond the use of photometric redshifts, 3D-MF does not apply any additional colour-selection criteria for identifying clusters (e.g. that cluster members must fall on the red sequence). A similar algorithm tuned for galaxy groups was introduced by Gillis and Hudson (2011). Every cluster-finding technique will pick out clusters with somewhat distinct characteristics because of different assumptions that are made in the algorithm, and it is therefore important to characterize and contrast independent samples of clusters (Milkeraitis et al., 2010).

Among the broad array of analysis tools employed by the galaxy cluster research community, gravitational lensing is a crucial technique for obtaining masses and density profiles, independent of assumptions regarding cluster dynamical state. In the weak regime, lensing provides robust measurements of stacked cluster samples (and individual masses for very massive clusters), affording a statistical view of average galaxy cluster properties (Hoekstra et al., 2013). The majority of weak lensing studies measure the shear, or shape distortion, of lensed source galaxies. The complementary magnification component of the lensing signal has more recently been measured with increasing precision (Scranton et al., 2005; Hildebrandt et al., 2009b; Ford et al., 2012, 2014; Morrison et al., 2012; Hildebrandt et al., 2013; Bauer et al., 2014), and has been combined with shear in joint-lensing analyses (Umetsu et al., 2011, 2014). When combined with other cluster observables, lensing yields useful scaling relations that can be extrapolated with some caution to wider cluster populations, or cross-examined to characterize intrinsic disparities that may distinguish catalogues compiled using different cluster-finding techniques (Hoekstra, 2007; Johnston et al., 2007; Leauthaud et al., 2010; Hoekstra et al., 2012; Covone et al., 2014; Oguri, 2014).

Section 2 of this paper describes the data, Section 3 gives the formalism of the weak lensing measurement, and Section 4 presents the results. We then discuss and compare our findings to other results, including our previous magnification measurements of the same lens sample, in Section 5. We finish with conclusions in Section 6. Throughout this work we use a concordance  $\Lambda$  cold dark matter cosmology with  $\Omega_M = 0.3$ ,  $\Omega_\Lambda = 0.7$ , and  $H_0 = 70$  km/s/Mpc.

## 4.2 Data

### 4.2.1 The Canada-France-Hawaii Telescope Legacy Survey Wide

The Canada-France-Hawaii Telescope Legacy Survey (CFHTLS) is a multi-component optical survey conducted over more than 2300 h in 5 yr ( $\sim 450$  nights) using the wide field optical imaging camera MegaCam on the CFHT’s imaging system MegaPrime. The Wide survey is composed of four patches ranging from 25-72 deg<sup>2</sup>, together totalling an effective survey area of  $\sim 154$  deg<sup>2</sup>. The data were acquired through five filters:  $u^*$ ,  $g'$ ,  $r'$ ,  $i'$ ,  $z'$ , and has a  $5\sigma$  point source  $i'$ -band limiting magnitude of 24.5. The breadth of CFHTLS-Wide was intended for the study of large scale structure and matter distribution in the Universe.

The CFHTLS-Wide optical multi-colour catalogues used in this work were created from stacked images of the aforementioned Wide fields (see Erben et al., 2009; Hildebrandt et al., 2009a, 2012; Erben et al., 2013, for details on the data processing and multi-colour catalogue creation). Basic photometric redshift ( $z_{\text{phot}}$ ) statistics were determined by Hildebrandt et al. (2012). In this work we restrict ourselves to a redshift range of  $0.1 \leq z \leq 1.2$ , which has outlier rates  $\leq 6\%$  and scatter  $\sigma \leq 0.06$ .

## 4.2.2 CFHTLenS Shear Catalogue

The Canada-France-Hawaii Telescope Lensing Survey (CFHTLenS) reduced CFHTLS-Wide data for weak lensing science applications (Heymans et al., 2012; Erben et al., 2013). Many factors affect high-precision weak lensing analyses, including correlated background noise, PSF measurement, and galaxy morphology evolution for example (for a more detailed list and study, see Massey et al., 2007a; Heymans et al., 2012). The efforts of CFHTLenS have led to new reduction methodologies with reduced systematic errors and a more thorough understanding of the PSF and its variation in the CFHTLS-Wide images. As part of this pipeline, *lensfit* was used to measure galaxy shapes (Miller et al., 2013), which were tested for systematics in Heymans et al. (2012). The galaxy shear measurements and photometric redshifts used in this work are publicly available.<sup>1</sup>

## 4.2.3 3D-MF Clusters

Here we give a brief overview of the 3D-MF galaxy cluster-finding algorithm. For additional background and details on the algorithm, including extensive testing on the Millennium Simulation data set, and information on the completeness and purity of a 3D-MF derived galaxy cluster catalogue, the reader is directed to Milkeraitis et al. (2010).

3D-MF searches survey data for areas that maximally match a given luminosity and radial profile for a fiducial galaxy cluster, similar to the technique used by Postman et al. (1996). For the luminosity profile we use an integrable Schechter function, given by

$$\Phi(M) = 0.4 \ln(10) \Phi^* 10^{0.4(\alpha+1)(M^*-M)} \exp \left[ -10^{0.4(M^*-M)} \right], \quad (4.1)$$

where  $\Phi$  is the galaxy luminosity function,  $\Phi^*$  sets the overall normalization,  $M$  is absolute magnitude,  $M^*$  is a characteristic absolute magnitude, and  $\alpha$  is the faint end slope of the luminosity function. As discussed in Milkeraitis et al. (2010), the multiplicative term,  $\exp[-10^{0.4(M^*-M)}]$ , keeps this function from diverging when  $\alpha < -1$  and  $M < M^*$ . For the radial profile we use a truncated Hubble profile, given by

$$P\left(\frac{r}{r_c}\right) = \frac{1}{\sqrt{1 + \left(\frac{r}{r_c}\right)^2}} - \frac{1}{\sqrt{1 + \left(\frac{r_{co}}{r_c}\right)^2}}, \quad (4.2)$$

where  $r_c$  is the cluster core radius, and  $r_{co} \gg r_c$  is the cutoff radius. In an attempt to match both of the above profiles, 3D-MF creates likelihood maps of the sky survey area. Peaks in this map are possible cluster detections, and are each assigned a significance  $\sigma_{cl}$  relative to the background signal ( $\sigma_{cl}$  is calculated using Equation 5 of Milkeraitis et al., 2010, which the reader is referred to for more details). The cluster centres are defined to be the locations of the likelihood peaks; see Section 4.3.3 for how uncertainties in the centres are dealt with.

An important characteristic of this cluster-finding algorithm is the fact that the described process is carried out in discrete redshift bins to avoid spurious false-detections due to line-of-sight projections. 3D-MF was run on the CFHTLS-Wide catalogues with redshift slices of width  $\Delta z = 0.2$ , which are then shifted by 0.1, and the finder is run again on the overlapping redshift slices. Clusters are assigned a final redshift estimate (of bin width  $\Delta z = 0.1$ ) by using the centre of the slice that maximizes cluster detection significance. 3D-MF was run using the same run-time parameters listed in table 2 in Milkeraitis et al. (2010), with the exception of an absolute  $i'$ -band

<sup>1</sup>[www.cfhtlens.org](http://www.cfhtlens.org); Data products are made available at <http://www.cadc-ccda.hia-ihp.nrc-cnrc.gc.ca/community/CFHTLenS/query.html>



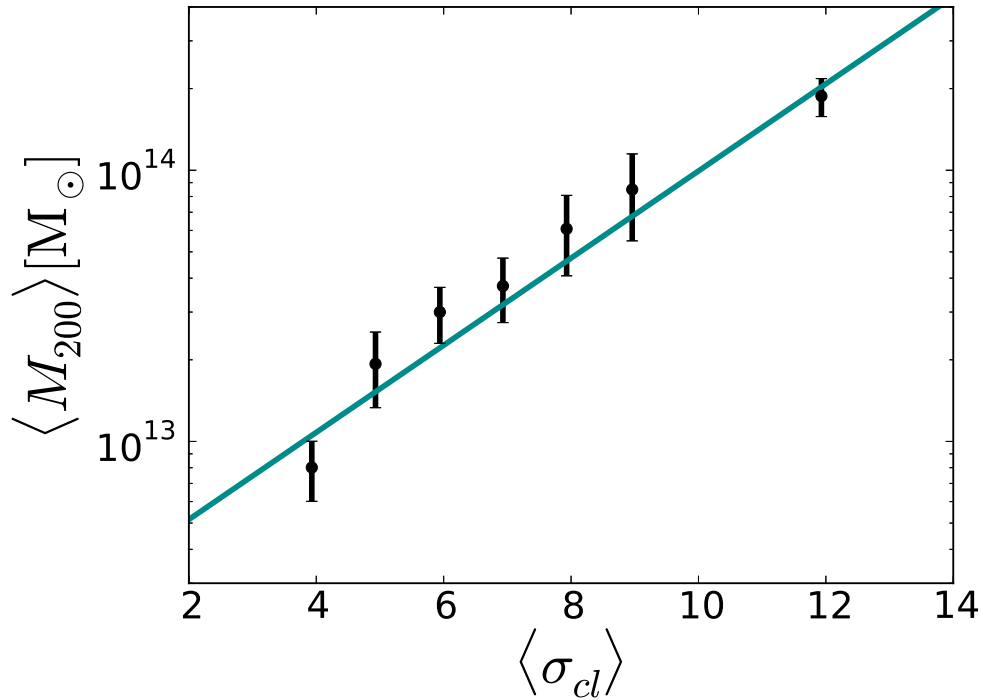


**Figure 4.1:** Scaling of shear-measured mass  $M_{200}$  with the 3D-MF cluster detection significance  $\sigma_{cl}$ . Since we find significance to be a good proxy for mass, we use the derived mass-significance relation to estimate a radius  $r_{200}$  for each cluster candidate, within which we count galaxies for richness  $N_{200}$ , as described in the Section 4.2.3.

magnitude of  $M_{i'-band}^* = -23.22 \pm 0.01$  and slope of the Schechter luminosity function,  $\alpha = -1.04 \pm 0.01$ , derived from the Wide data (Milkeraitis, 2011).

Excluding possible multiple detections, a total of 22,694 galaxy cluster candidates were found in the CFHTLS-Wide data set with detection significance  $\sigma_{cl} \geq 3.5$ . Using 3D-MF’s multiple detection criteria, there were 34.4% additional duplicate detections of galaxy clusters. This is comparable to the  $\sim 36\%$  multiple detection rate found from Millennium Simulation tests and 37.6% found in the CFHTLS-Deep galaxy cluster catalogue in Milkeraitis et al. (2010). Using the Millennium Simulation, Milkeraitis et al. (2010) determined that there are potentially  $\sim 16\% - 24\%$  false positives in 3D-MF-derived galaxy cluster catalogues, distributed mostly in the lower significance ranges (see Table 3 in Milkeraitis et al., 2010).

Following the 3D-MF methodology for galaxy cluster catalogue generation, the significance of galaxy cluster detections was used to select the best galaxy cluster candidate among multiple detections, and the remaining multiple detections were rejected from the analysis. A single detection of each cluster candidate then makes up the CFHTLS-Wide galaxy cluster candidate catalogue. We restrict our analysis herein to a cluster redshift range of  $0.2 \leq z \leq 0.9$ , where 3D-MF detections are the most reliable.

In Ford et al. (2014), we described our method of calculating richness for each of these candidate clusters.  $N_{200}$  is defined to be the number of member galaxies brighter than absolute magnitude  $M_i \geq -19.35$ , which is chosen to match the limiting magnitude at the furthest cluster redshift that we probe ( $N_{200}$  is background-subtracted; there is no correction for passive evolution). To be considered a cluster member, a galaxy must lie within a projected radius  $R_{200}$  of a cluster centre, and have  $\Delta z < 0.08(1+z)$  (based on the photometric errors of the CFHTLenS catalogue; for details regarding  $N_{200}$  see Ford et al., 2014).  $R_{200}$  is defined as radius within

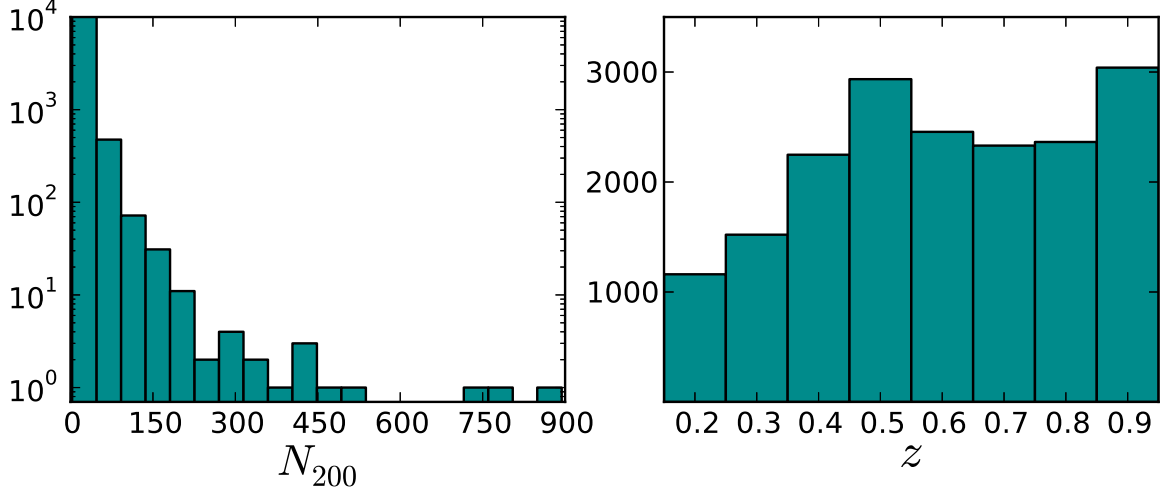


**Figure 4.2:** Number of 3D-MF cluster candidates as a function of richness  $N_{200}$  and redshift  $z$ .

which the average density is 200 times the critical energy density of the Universe ( $M_{200}$  is the total mass inside  $R_{200}$ ), and in this work has been re-estimated from the data as follows.

Initially cluster candidates were stacked in bins of cluster detection significance  $\sigma_{cl}$ , which was found to correlate well with the amplitude of the measured shear profiles, and therefore with mass (see Figure 4.1). These preliminary masses were estimated using the same method described in Section 4.3. A new mass-significance relationship,

$$\log \left[ \frac{M_{200}^{\text{prelim}}}{M_{\odot}} \right] = (0.161^{+0.006}_{-0.009}) \sigma_{cl} + 12.39^{+0.05}_{-0.08}, \quad (4.3)$$

was derived from this result and the preliminary mass values converted into the corresponding radii, which were used to count galaxies for richness ( $\sigma_{cl} \rightarrow M_{200}^{\text{prelim}} \rightarrow R_{200} \rightarrow N_{200}$ ). Compared with the richness estimates used in Ford et al. (2014), which were based on a preliminary shear analysis using a more basic cluster modelling approach (Milkeraitis, 2011), the updated richnesses are larger in most cases (see the Full Model description in Section 4.3.4 for improvements). For the log-normal curve in Figure 4.1, as well as for all models fit in this work, the best fit is the curve that minimizes  $\chi^2$ , using a downhill simplex algorithm to search parameter space.

Cluster candidates used in this work are required to have at least  $N_{200} > 2$ , and a detection significance  $\geq 3.5$ . The richness and redshift distributions are summarized in Figure 4.2. Figure 4.3 shows the relative scaling between richness and detection significance. The final catalogue contains the same 18036 cluster candidates used in Ford et al. (2014), now with updated richness estimates based on the shear mass-significance scaling just described. There are also 20 additional low-significance cluster candidates whose revised  $N_{200}$  now survive the cuts – these systems have negligible impact on the overall results, but do increase the total number of clusters to 18056. The full 3D-MF catalogue is available at [cfhtlens.org](http://cfhtlens.org).

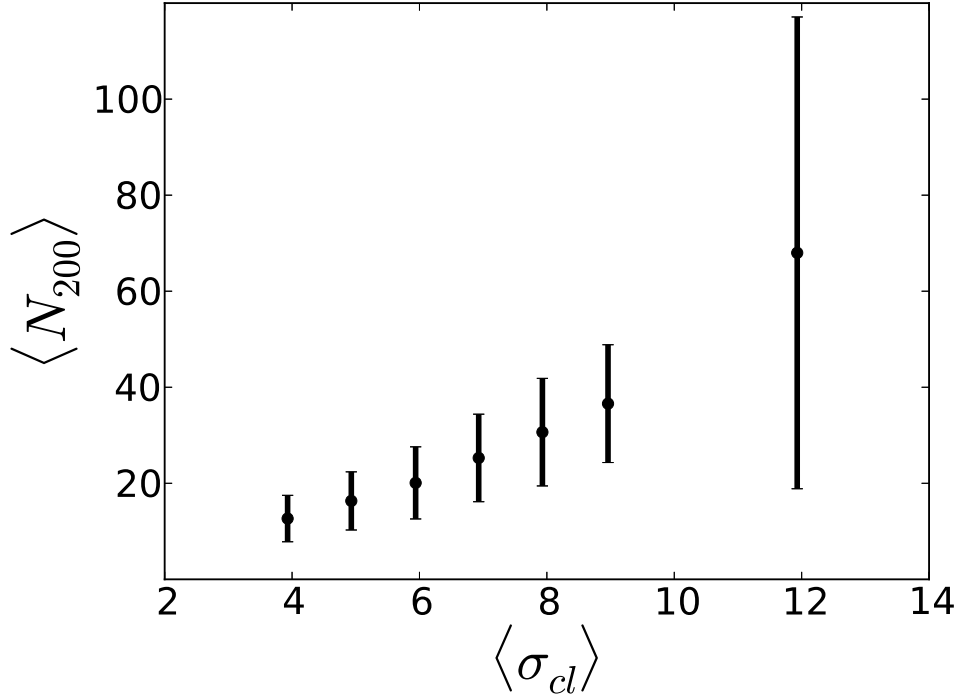


**Figure 4.3:** Scaling of richness  $N_{200}$  with the 3D-MF cluster detection significance  $\sigma_{cl}$ . Error bars denote the standard deviation of the ensemble of  $N_{200}$  values in each  $\sigma_{cl}$  bin. Since  $N_{200}$  is estimated using individual cluster radii calculated from the mass-significance relation (Equation 4.3), this figure confirms what we would expect – a strong scaling between richness and significance.

## 4.3 Method

### 4.3.1 Stacking Galaxy Clusters

The mass of a galaxy cluster can be determined by measuring shear in binned annuli out from the cluster centre, and fitting this with a theoretical density profile. For the most massive galaxy clusters, this is relatively straightforward. However, for most galaxy clusters (especially given the high number of lower mass galaxy cluster candidates explored in this work), the background noise overwhelms the measurable shear. Fortunately, stacking many individual galaxy clusters together improves the signal-to-noise ratio, enabling the measurement of a statistically significant signal, averaged over a cluster ensemble.

To obtain a meaningful average for a property of an ensemble of galaxy clusters, similar clusters must clearly be chosen for a stack. It is desirable to stack clusters of very similar mass (and thus clusters of roughly the same size and profile), as an average mass measurement of the cluster stacks is the goal. In fitting models to the stacked weak lensing measurements in this work, we assume that the haloes are spherical on average. However, recent studies have explored halo orientation bias in simulations, demonstrating that optically-selected clusters will tend to be aligned along the line-of-sight, and this effect could lead to our mass estimates being biased high by 3 – 6% (Dietrich et al., 2014).

For this analysis, the cluster candidates are stacked in bins of richness  $N_{200}$  as well as redshift, identical to those used in Ford et al. (2014). The overall approach is conceptually very similar to that used in galaxy-galaxy lensing (see Velander et al., 2014), except we replace the galaxy lenses with cluster lenses.

### 4.3.2 Measuring $\Delta\Sigma$

We measure the radial profile of the tangential shear,  $\gamma_t(R)$ , around each cluster candidate in bins of projected *physical* distance  $R$ , extending from 0.09 to 5 Mpc. The logarithmically-spaced radial bins are chosen to match those used in Ford et al. (2014), which we compare results to in Section 4.5.5, and the resulting mass measurements are insensitive to small adjustments in the innermost radii. To select background galaxies for measuring shear, we use their redshift probability distributions  $P(z_s)$ , where  $z_s$  is the source redshift. Relative to a given cluster redshift ( $z_l$ ), we require both that (1) the peak of a galaxy's  $P(z_s)$  distribution is at higher redshift, and (2) at least 90% of a galaxy's  $P(z_s)$  is at higher redshift. The second requirement is designed to account for the occasional galaxy with an odd  $P(z_s)$ , which may peak at high redshift (and so would be included in many conventional shear analyses), but could perhaps have a non-negligible tail extending to low  $z$ , or even be bimodal.

From the individual shear profiles we construct  $\Delta\Sigma$ , the differential surface mass density, for each stacked cluster candidate sample:

$$\Delta\Sigma(R) \equiv \bar{\Sigma}(<R) - \Sigma(R) = \langle \gamma_t(R) \rangle \Sigma_{\text{crit}}. \quad (4.4)$$

Here  $\Sigma(R)$  is the surface mass density of a lens, and  $\Sigma_{\text{crit}}$  is the critical surface mass density, which depends on the geometry of the lens-source pairs. It is given by

$$\Sigma_{\text{crit}} = \frac{C^2}{4\pi G} \frac{D_s}{D_l D_{ls}}, \quad (4.5)$$

where  $C$  is the speed of light and  $D_s$ ,  $D_l$ , and  $D_{ls}$ , are the angular diameter distances to the source, to the lens, and between the lens and source, respectively.

In computing  $\Sigma_{\text{crit}}$  for *each lens-source pair*, we treat the individual lens  $z_l$  as fixed, and integrate over the full source  $P(z_s)$ , for  $z_s > z_l$ , to compute the distances:

$$D_s = \int_{z_l}^{\infty} D_{\text{ang}}(0, z_s) P(z_s) dz_s \quad (4.6)$$

$$D_{ls} = \int_{z_l}^{\infty} D_{\text{ang}}(z_l, z_s) P(z_s) dz_s \quad (4.7)$$

Here  $D_{\text{ang}}$  is the angular diameter distance between two redshifts (and  $D_l$  is simply  $D_{\text{ang}}(0, z_l)$ ). The source redshift probability distribution is renormalized behind the lens, so that  $\int_{z_l}^{\infty} P(z_s) dz_s = 1$ . Using the full  $P(z_s)$  distribution should improve any residual photo- $z$  calibration bias in the lensing measurement (Mandelbaum et al., 2008b).

We follow the same procedure described in detail in Velander et al. (2014), wherein we combine shear profiles using the *lensfit* source weighting (Equation 8 of Miller et al., 2013), and apply a correction for multiplicative bias (Miller et al., 2013), so that the  $\langle \gamma_t(R) \rangle$  appearing in Equation 4.4 is the average *calibrated* tangential shear. We estimate a covariance matrix for each stacked sample, by running 100 sets of bootstrapped cluster measurements, and calculating the covariance as:

$$C(R_i, R_j) = \left[ \frac{N}{N-1} \right]^2 \frac{1}{N} \sum_{k=1}^N [\Delta\Sigma_k(R_i) - \bar{\Delta\Sigma}(R_i)] \times [\Delta\Sigma_k(R_j) - \bar{\Delta\Sigma}(R_j)] \quad (4.8)$$

Here  $N$  is the number of bootstrap samples,  $R_i$  and  $R_j$  denote specific angular bins, and  $\overline{\Delta\Sigma}(R_i)$  is the differential surface mass density at  $R_i$ , averaged across all bootstrap realizations. The square-root of the diagonal of this matrix yields the error bars displayed on the weak lensing measurements in Section 4.4. We confirm that  $N = 100$  bootstrap realizations of the data is sufficient by tracking the covariance estimated from different numbers of bootstrapped samples and checking for convergence, which typically occurs at around 40 realizations. We use the full covariance matrices when fitting to the data, as will be described in Section 4.1.

We test our  $\Delta\Sigma$  measurements for systematics by measuring the rotated shear  $\gamma_r(R)$  (where each galaxy ellipticity is rotated by  $45^\circ$ ), finding a signal consistent with zero. We also check that masked areas and edge effects are not affecting our measurement, by measuring  $\Delta\Sigma$  around many randomly chosen points ( $> 50$  times the number of cluster candidates), and we find no significant signal here either.

### The NFW model

We use the Navarro, Frenk and White (NFW) dark matter density profile (Navarro et al., 1997) for modelling  $\Delta\Sigma$ . As demonstrated by numerical simulations, the dissipationless collapse of density fluctuations under gravity produces overdensities that are approximated well by the NFW profile

$$\rho_{\text{NFW}}(r) = \frac{\delta_c \rho_{\text{crit}}(z)}{(r/r_s)(1 + r/r_s)^2}, \quad (4.9)$$

where  $\delta_c$  is the characteristic overdensity of a halo, and  $\rho_{\text{crit}}(z)$  is the critical energy density of the Universe at that redshift. The scale radius is  $r_s = R_{200}/c$ , where  $c$  is the concentration parameter (not to be confused with the speed of light  $C$  in Equation 4.5).  $R_{200}$  is the cluster radius, and the total mass within that radius is known as  $M_{200}$ . Wright and Brainerd (2000) derived the NFW forms of the projected mass density profiles in Equation 4.4, which we make use of in this work.

In general, the NFW profile is a two parameter model for the halo density, commonly parametrized in terms of  $M_{200}$  and  $c$ . However, there is a well-established correlation between these two parameters, and it is common to introduce a mass-concentration relation to reduce the dimensionality of the problem (note that concentration itself may be degenerate with cluster centroid offsets, which will be discussed in Section 4.3.3). In this work we invoke the mass-concentration relation recently presented by Dutton and Macciò (2014) for the Planck cosmological parameters, which successfully characterizes the profiles of simulated haloes spanning a wide range of masses and redshifts. Given a cluster mass, the concentration is then fixed, and we have just a single mass-related fit parameter to deal with.

### Non-weak shear corrections

The gravitational lensing observable is galaxy shapes. From these, we measure the reduced shear  $g = \gamma/(1 - \kappa)$  about the lens, where  $\gamma$  is the true shear and  $\kappa = \Sigma/\Sigma_{\text{crit}}$  is the convergence (as before, calculated using the NFW halo formalism in Wright and Brainerd, 2000). At the innermost radii that we probe ( $\sim 0.1$  Mpc) the common weak lensing assumption that  $g \approx \gamma$  may break down for the more massive clusters. We account for the difference between true and reduced shear using the correction factor from Johnston et al. (2007), which was worked out in detail in Mandelbaum et al. (2006). The differential surface mass density corrected for non-weak shear is given by:

$$\widehat{\Delta\Sigma} = \Delta\Sigma + \Delta\Sigma \Sigma \mathcal{L}_z, \quad (4.10)$$

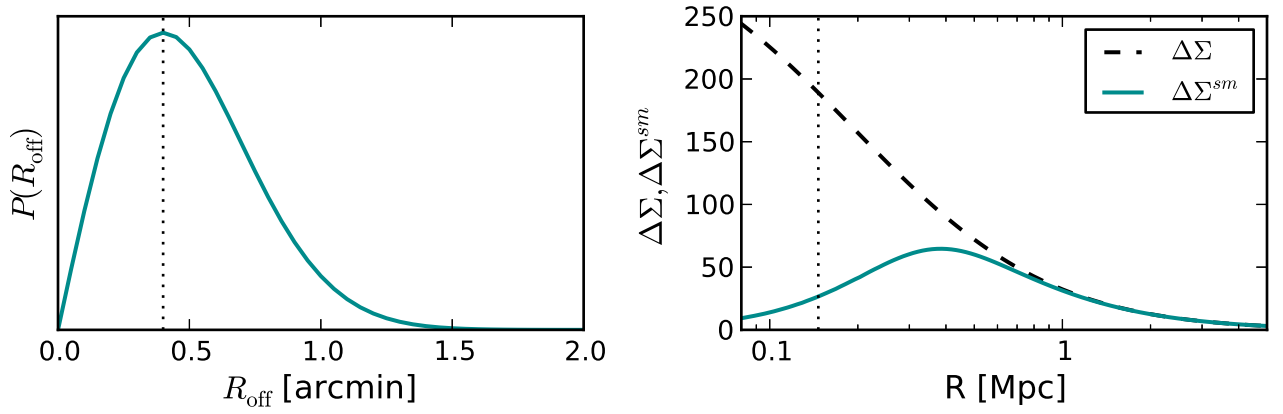


**Figure 4.4:** This figure is an illustrative example of typical  $\Delta\Sigma(R)$  and  $\Delta\Sigma^{\text{sm}}(R)$  profiles, to demonstrate the effects of cluster miscentring (Equations 7 – 11) on measured shear density profiles. The left-hand panel shows a typical probability distribution of centroid offsets,  $P(R_{\text{off}})$ , modelled via a 2D Gaussian with  $\sigma_{\text{off}} = 0.4$  arcmin. The right-hand panel demonstrates the effect of this offset distribution on the measured shear profile (in vertical axis units of  $[M_{\odot}/\text{pc}^2]$ ) of a fiducial halo of mass  $M_{200} = 10^{14} M_{\odot}$ , located at  $z = 0.5$ . The dashed black curve shows the perfectly centred  $\Delta\Sigma(R)$  profile, and the solid blue curve shows the miscentred profile  $\Delta\Sigma^{\text{sm}}(R)$ . In both panels, the vertical dotted line marks the location of the miscentring offset  $\sigma_{\text{off}}$ , to guide the eye in the comparison.

where  $\mathcal{L}_z = \langle \Sigma_{\text{crit}}^{-3} \rangle / \langle \Sigma_{\text{crit}}^{-2} \rangle$  is calculated for each cluster redshift, using the full distribution of background galaxies satisfying the same redshift requirements outlined in Section 4.3.2. Similar to Leauthaud et al. (2010), we ignore any radial variations of  $\mathcal{L}_z$ , but do account for the variation with redshift, as our cluster sample spans a large  $z$  range. The entire correction term  $\Delta\Sigma \Sigma \mathcal{L}_z$  is negligible at all radii except for the innermost bin, where it typically makes up a few percent (at most  $\sim 10\%$ ) of the measured signal.

### 4.3.3 Miscentring Formalism

As was shown in Milkeraitis et al. (2010), 3D-MF does not always determine the exact correct centre for a galaxy cluster, and clusters may not always have a well-defined centre. This is a problem with all galaxy cluster finders and dealing with it properly involves understanding and quantifying its effects, such as including the uncertainty of the centre in calculations. The amplitude of measured shear profiles is absolutely dependent on the declared centre of the profile, so miscentring can potentially have a large impact on results. Offset cluster centres that are mistakenly modelled as being the true centres of the gravitational potentials will lead to underestimates in the inferred lens masses.

In our first analysis of the 3D-MF cluster candidates, we found modest evidence for cluster centroid errors (Ford et al., 2014). However, that work relied on the lensing magnification technique, which is less sensitive to these effects than the shear, since magnification directly probes  $\Sigma(R)$ , while it is  $\Delta\Sigma(R)$  that is more drastically reduced by a misplaced centre. See, for example, fig. 4 in Johnston et al. (2007), for a nice illustration of the comparative effect of miscentring on these two lensing profiles.

In this work, we are able to directly quantify the presence of cluster miscentring by fitting for the offsets in our measurements of  $\Delta\Sigma$ . As will be shown in Section 4, we find that the best-fitting distribution of centroid offsets is in agreement with the following distribution based on simulations, which we assumed in Ford et al. (2014).

The distribution of cluster offsets can be modelled as a two-dimensional Gaussian, by using a uniform angular distribution and the following radial profile:

$$P(R_{\text{off}}) = \frac{R_{\text{off}}}{\sigma_{\text{off}}^2} \exp \left[ -\frac{1}{2} \left( \frac{R_{\text{off}}}{\sigma_{\text{off}}} \right)^2 \right]. \quad (4.11)$$

Here,  $R_{\text{off}}$  is the projected offset of the 3D-MF derived galaxy cluster centre from the true galaxy cluster centre, and  $\sigma_{\text{off}}$  is the width of the distribution and one of the miscentring parameters which we fit to the stacked shear measurement. An example  $P(R_{\text{off}})$  curve is plotted in the left-hand panel of Figure 4.4, for  $\sigma_{\text{off}}=0.4$  arcmin. Note that we use physical units (e.g. Mpc) for most distances in this work, the exception being  $\sigma_{\text{off}}$  which we report in angular size (arcmin). The reason for this choice is that we believe a significant contribution to miscentring derives from 3D-MF's cluster characterization, which does not for example select a member galaxy as the centre (this choice of angular size is a matter of taste, since complex cluster physics certainly contributes to ambiguous halo centres).

The effect of this offset distribution  $P(R_{\text{off}})$  is to reduce the ideal  $\Sigma(R)$  to a smoothed profile (see e.g. Johnston et al., 2007; George et al., 2012)

$$\Sigma^{\text{sm}}(R) = \int_0^\infty \Sigma(R|R_{\text{off}}) P(R_{\text{off}}) dR_{\text{off}}, \quad (4.12)$$

which is illustrated in the right-hand panel of Figure 4.4. Equation 4.12 is an integration over all possible values of  $R_{\text{off}}$  in the distribution. The expression for the surface mass density at a single  $R_{\text{off}}$  is

$$\Sigma(R|R_{\text{off}}) = \frac{1}{2\pi} \int_0^{2\pi} \Sigma(r) d\theta, \quad (4.13)$$

where  $r = \sqrt{R^2 + R_{\text{off}}^2 - 2RR_{\text{off}}\cos(\theta)}$  and  $\theta$  is the azimuthal angle (Yang et al., 2006). From the smoothed  $\Sigma^{\text{sm}}(R)$  profile, we can obtain the smoothed shear profile:

$$\Delta\Sigma^{\text{sm}} = \overline{\Sigma^{\text{sm}}}(< R) - \Sigma^{\text{sm}}(R) \quad (4.14)$$

$$\overline{\Sigma^{\text{sm}}}(< R) = \frac{2}{R^2} \int_0^R \Sigma^{\text{sm}}(R') R' dR' \quad (4.15)$$

See George et al. (2012) for a discussion of the effects of cluster miscentring on measured shear profiles. There are several different approaches in the literature for actually applying this formalism to data. For example, in some work authors apply the same smoothing to all clusters in a stack (George et al., 2012), whereas others apply a two-component smoothing profile (Oguri, 2014), or chose a uniform distribution of offsets instead of the Gaussian (Sehgal et al., 2013). In our previous analysis of this cluster candidate sample, the magnification technique did not give significant constraining power for additional parameters, so we simply compared fits for both a perfectly centred and miscentred model, using estimates of  $\sigma_{\text{off}}$  obtained from running 3D-MF on simulations (Ford et al., 2014). Both Johnston et al. (2007) and Covone et al. (2014) applied a combination of perfectly centred and miscentred haloes, thus fitting for the fraction of offset clusters in addition to the magnitude of the offset distribution  $\sigma_{\text{off}}$ . We follow this latter approach in the current analysis.

As a caveat, we note that the degree of miscentring is fairly degenerate with the cluster concentration pa-

parameter, as both can have an effect on the amplitude of the inner shear profile. For example, we tried using the mass-concentration relation of Prada et al. (2012), which yields higher concentration for a given mass than the Dutton and Macciò (2014) relation used here, and results in a best fit with larger centroid offsets. For the lower mass (richness) clusters this change is negligible, but for the most massive clusters in this study, the choice of concentration-mass relation can affect the miscentring fit parameters by as much as 40%. Importantly, however, the best-fitting cluster mass is the *same* in both cases (within the stated  $1\sigma$  uncertainties). The degeneracy of cluster concentration and miscentring would be important to consider in a study seeking to constrain cluster mass-concentration relations. The measured concentrations will be biased low if cluster centroid offsets are significant and not fully accounted for.

#### 4.3.4 The Halo Model

Weak lensing measurements are sensitive to the fact that structures in the Universe are spatially correlated. We account for this large scale clustering using the halo model, which provides a useful framework for modelling the clustered and complex dark matter environments that we probe in gravitational lensing studies. This phenomenological approach places all the matter in the Universe into spherical haloes, which are clustered according to their mass. Observables such as galaxies and clusters are considered biased tracers of the underlying dark matter distribution, with a bias factor that has been constrained in many numerical simulations (e.g. Mo and White, 1996; Sheth and Tormen, 1999; Tinker et al., 2010). See Cooray and Sheth (2002) for an extensive review of the halo model.

We follow an approach similar to Johnston et al. (2007), in considering a two-halo term in addition to the main NFW halo fit to our weak lensing shear measurement. Calculation of the two-halo term is identical to our approach in Ford et al. (2014), and we refer the reader there for explicit details. The two-halo term is proportional to a cluster bias factor which depends on mass, and for this we continue to use the  $b(M)$  relation of Seljak and Warren (2004). The full model including the two-halo term is:

$$\Delta\Sigma(R) = p_{\text{cc}}\Delta\Sigma_{\text{NFW}} + (1 - p_{\text{cc}})\Delta\Sigma_{\text{NFW}}^{\text{sm}} + \Delta\Sigma_{\text{2halo}} \quad (4.16)$$

The fraction of cluster candidates that is *correctly centred* on their parent dark matter haloes,  $p_{\text{cc}}$ , is a parameter that we fit to the data.  $p_{\text{cc}}$  is a continuous variable, bounded between 0 and 1, fit separately for each stacked weak lensing measurement. Thus we have two cluster-centring-related parameters ( $p_{\text{cc}}$  and  $\sigma_{\text{off}}$ ), as well as one mass-related parameter ( $M_0$ ), in the final modelling of the data.

## 4.4 Galaxy Cluster Weak Lensing Shear Results



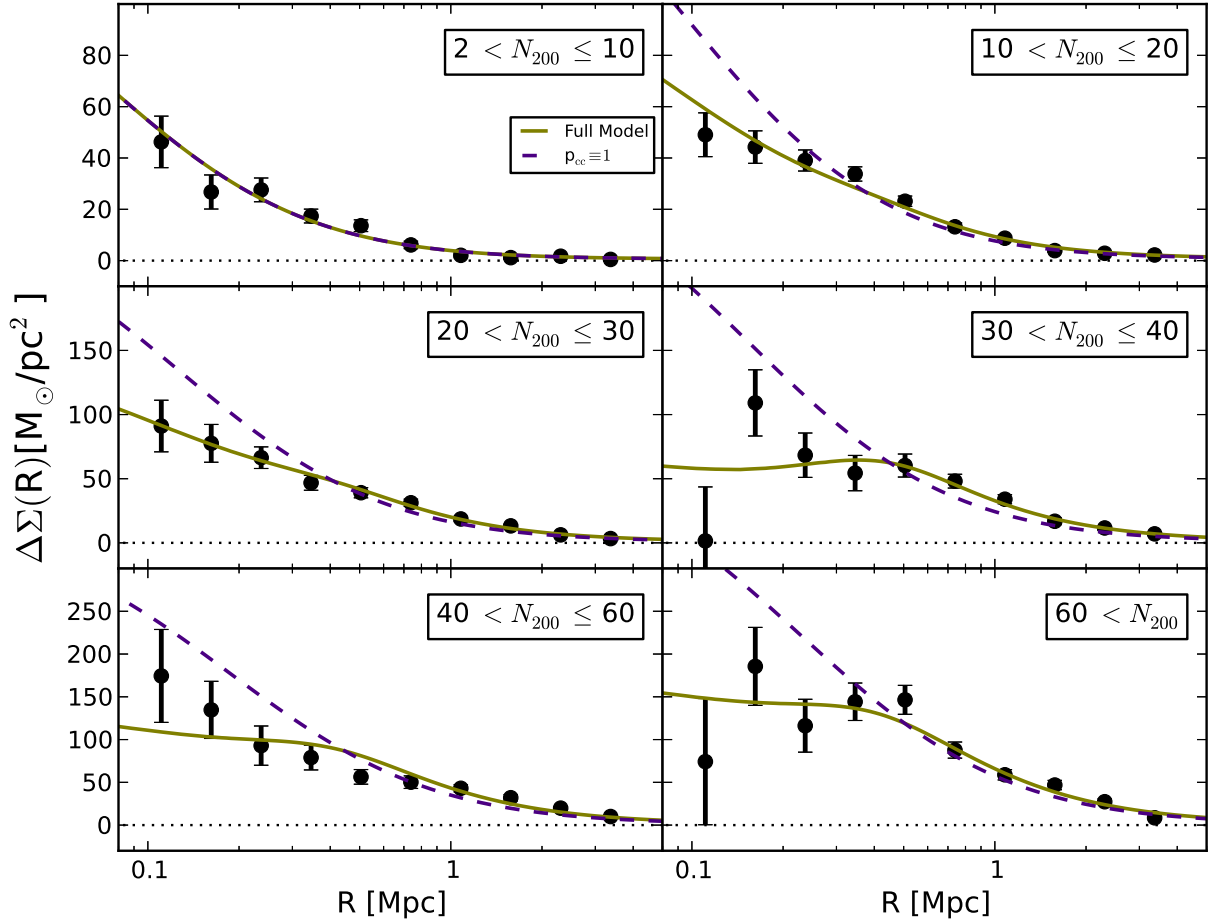


**Figure 4.5:** Best-fitting models for each richness-binned stack of cluster candidates. The solid green curves are the best fits to the full model given by Equation 4.16. The dashed purple curves are the best-fitting models which assumes that every cluster centre identified by 3D-MF is perfectly aligned with the dark matter halo centre. With the exception of the lowest richness bin, where the best-fitting curves coincide, the perfectly centred model does not provide a good fit to the data at small  $R$ . Tables 4.1 and 4.2 summarize the results of both fits.

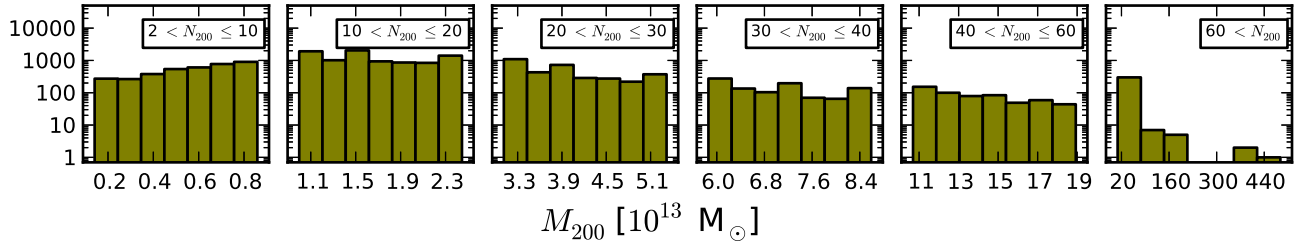


**Figure 4.6:** The underlying distribution of cluster candidate masses, within each of the six richness bins in Figure 4.5, for the full miscentred model. Because the parameters fit to the shear measurements are the normalization of the mass-richness relation (Equation 4.18) and the miscentring parameters  $p_{cc}$  and  $\sigma_{off}$ , the full (*not binned*) set of cluster  $N_{200}$  values are each converted to an individual cluster mass. We bin these masses for presentation in the above histograms only, but emphasize that the composite-halo modelling approach in this work treats every cluster candidate as having an individual mass (richness) and redshift. This figure is also a visual representation of the 3D-MF cluster mass function, as obtained from weak lensing shear.

**Table 4.1:** Details of the “Full Model” fits for the richness-binned measurements (Equation 4.16, green curves in Figure 4.5). This model has 7 degrees of freedom. We list the richness range selected, the number of cluster candidates in that bin, the shear detection significance, and the average richness and redshift of clusters in the bin. Fitted parameters include the centring-related parameters  $p_{\text{cc}}$  and  $\sigma_{\text{off}}$ , and the normalization of the mass-richness relation  $M_0$ , from which the average mass in each bin  $\langle M_{200} \rangle$  is derived. Note that the average mass given is not the value fit itself, but the average of all resulting masses fit using the composite-halo approach discussed in Section 4.3.2. See Figure 4.6 for a summary of the mass distributions within each  $N_{200}$  bin. Reduced generalized  $\chi^2$  are given for each bin, and should be compared with the corresponding fits listed in Table 4.2, for the simple one-parameter model assuming perfect centres.

Richness	Clusters	Significance	$\langle N_{200} \rangle$	$\langle z_l \rangle$	$p_{\text{cc}}$	$\sigma_{\text{off}}$	$M_0 [10^{13} M_\odot]$	$\langle M_{200} \rangle [10^{13} M_\odot]$	$\chi_{\text{red}}^2$
$2 < N_{200} \leq 10$	3745	$14.2\sigma$	8	0.45	$1.0_{-0.2}$	—	$2.4^{+0.9}_{-1.0}$	$0.6^{+0.2}_{-0.3}$	2.1
$10 < N_{200} \leq 20$	9034	$22.8\sigma$	15	0.63	$0.5 \pm 0.1$	$(0.40^{+0.06}_{-0.2})'$	$2.4 \pm 0.6$	$1.6 \pm 0.4$	2.3
$20 < N_{200} \leq 30$	3409	$25.6\sigma$	24	0.67	$0.5 \pm 0.1$	$(0.4^{+0.2}_{-0.1})'$	$2.9 \pm 0.5$	$3.9 \pm 0.7$	0.8
$30 < N_{200} \leq 40$	986	$23.4\sigma$	35	0.65	$0.5 \pm 0.2$	$(0.4 \pm 0.1)'$	$3.0 \pm 0.7$	$7 \pm 2$	2.6
$40 < N_{200} \leq 60$	568	$22.2\sigma$	48	0.60	$0.54 \pm 0.08$	$(1.3^{+0.5}_{-0.4})'$	$3.6^{+0.8}_{-1.0}$	$14^{+3}_{-4}$	0.3
$60 < N_{200}$	314	$22.5\sigma$	114	0.55	$0.5 \pm 0.2$	$(0.4^{+0.2}_{-0.1})'$	$1.6^{+0.4}_{-0.5}$	$26^{+6}_{-7}$	3.4

**Table 4.2:** This table is a companion to Table 4.1, giving details of the  $p_{\text{cc}} \equiv 1$  model fits for the richness-binned measurements (purple dashed curves in Figure 4.5). This model has 9 degrees of freedom. We list the richness range selected (the reader can refer to Table 4.1 for the number of clusters, shear significance, and average richness and redshift). For this model, there is a single fit parameter, the normalization of the mass-richness relation  $M_0$ , from which  $\langle M_{200} \rangle$  is derived (again see Figure 4.6 for the full distribution of masses in each richness bin).

Richness	$M_0 [10^{13} M_\odot]$	$\langle M_{200} \rangle [10^{13} M_\odot]$	$\chi_{\text{red}}^2$
$2 < N_{200} \leq 10$	$2.4^{+0.4}_{-0.6}$	$0.6 \pm 0.1$	1.6
$10 < N_{200} \leq 20$	$1.8 \pm 0.2$	$1.2 \pm 0.2$	4.8
$20 < N_{200} \leq 30$	$2.2^{+0.2}_{-0.3}$	$3.0^{+0.3}_{-0.4}$	5.3
$30 < N_{200} \leq 40$	$2.4 \pm 0.3$	$5.5 \pm 0.8$	4.4
$40 < N_{200} \leq 60$	$2.1 \pm 0.3$	$8 \pm 1$	4.7
$60 < N_{200}$	$1.4 \pm 0.2$	$23 \pm 3$	4.4

**Table 4.3:** Details of the “Full Model” fits for the redshift-binned measurements (green curves in Figure 4.8). This model has 7 degrees of freedom. We list the same bin properties and fits given in Table 4.1. The systematic errors listed on some cluster masses stem from uncertainties on the exact redshift of the cluster candidate. The fits in this table should be compared with the corresponding values in Table 4.4, which represents the perfectly centred model.

Redshift	Clusters	Significance	$\langle N_{200} \rangle$	$p_{cc}$	$\sigma_{off}$	$M_0 [10^{13} M_\odot]$	$\langle M_{200} \rangle [10^{13} M_\odot]$	$\chi^2_{red}$
$z \sim 0.2$	1161	$13.8\sigma$	14	$0.3 \pm 0.3$	$(0.4^{+0.3}_{-0.1})'$	$3 \pm 1$	$2.3^{+0.9}_{-1.0} \pm 0.4^{sys}$	0.6
$z \sim 0.3$	1521	$15.7\sigma$	17	$0.8^{+0.2}_{-0.3}$	$(0.4^{+1}_{-0.4})'$	$2.3^{+0.7}_{-0.9}$	$2.6^{+0.8}_{-0.9} \pm 0.2$	0.4
$z \sim 0.4$	2248	$17.0\sigma$	18	$0.7 \pm 0.2$	$(0.4^{+0.3}_{-0.2})'$	$2.6 \pm 0.9$	$3 \pm 1 \pm 0.1^{sys}$	0.8
$z \sim 0.5$	2935	$20.2\sigma$	18	$0.8 \pm 0.2$	$(0.4^{+0.2}_{-0.3})'$	$2.5^{+0.6}_{-0.8}$	$3.0^{+0.7}_{-1.0}$	1.7
$z \sim 0.6$	2456	$14.7\sigma$	20	$0.4 \pm 0.2$	$(0.4 \pm 0.1)'$	$3 \pm 1$	$4 \pm 1$	1.1
$z \sim 0.7$	2331	$11.9\sigma$	22	$0.7 \pm 0.3$	$(0.4^{+0.6}_{-0.4})'$	$2.1^{+0.9}_{-1.0}$	$3 \pm 1$	0.8
$z \sim 0.8$	2364	$8.7\sigma$	22	$0.2 \pm 0.2$	$(0.4 \pm 0.2)'$	$3^{+1}_{-3}$	$4^{+2}_{-3}$	1.9
$z \sim 0.9$	3040	$6.8\sigma$	19	$0.6 \pm 0.4$	$(0.4^{+1}_{-0.4})'$	$1.8^{+0.8}_{-1.7}$	$1.9^{+0.9}_{-1.8}$	0.5

**Table 4.4:** This table is a companion to Table 4.3, giving details of the  $p_{cc} \equiv 1$  model fits for the redshift-binned measurements (purple dashed curves in Figure 4.8). This model has 9 degrees of freedom. For this model, there is a single fit parameter, the normalization of the mass-richness relation  $M_0$ , from which  $\langle M_{200} \rangle$  is derived.

Redshift	$M_0 [10^{13} M_\odot]$	$\langle M_{200} \rangle [10^{13} M_\odot]$	$\chi^2_{red}$
$z \sim 0.2$	$2.6 \pm 0.6$	$2.0 \pm 0.5 \pm 0.3^{sys}$	2.1
$z \sim 0.3$	$2.1 \pm 0.4$	$2.4 \pm 0.4 \pm 0.2^{sys}$	0.4
$z \sim 0.4$	$2.2 \pm 0.4$	$2.7 \pm 0.5 \pm 0.1^{sys}$	1.4
$z \sim 0.5$	$2.2 \pm 0.3$	$2.7 \pm 0.4$	1.6
$z \sim 0.6$	$2.4 \pm 0.6$	$2.9 \pm 0.7$	4.5
$z \sim 0.7$	$1.9^{+0.4}_{-0.5}$	$2.4^{+0.6}_{-0.7}$	0.8
$z \sim 0.8$	$1.4 \pm 0.6$	$1.8 \pm 0.8$	3.3
$z \sim 0.9$	$1.3 \pm 0.6$	$1.4 \pm 0.6$	0.6

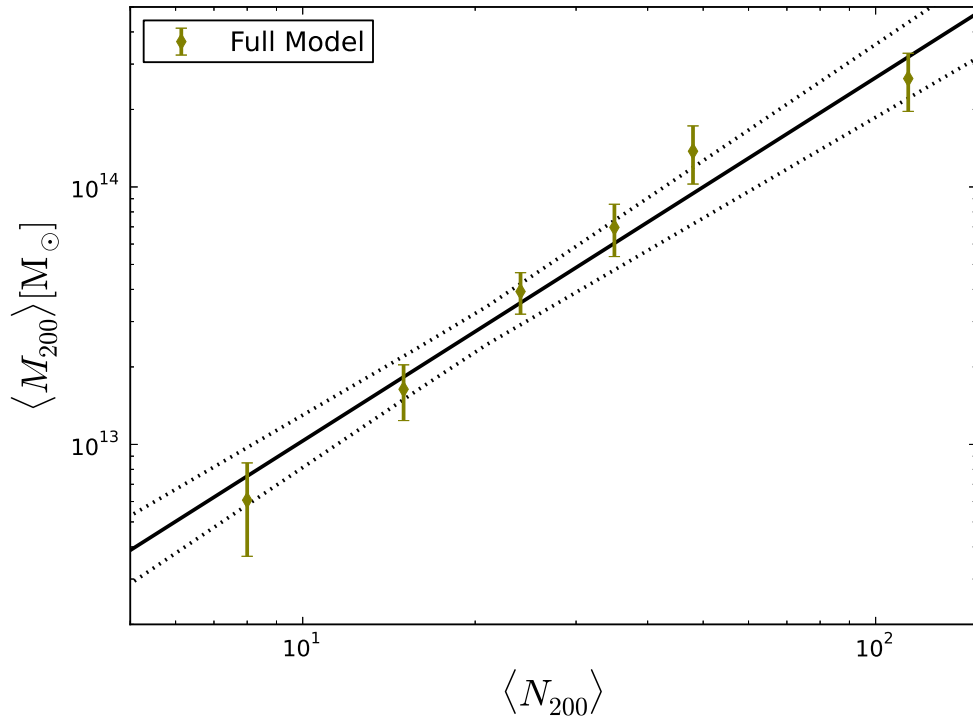


**Figure 4.7:** Power law best fit to mass-richness relation (Equation 4.18) obtained from average masses measured for the individual  $N_{200}$  bins in Figure 4.5 and Table 4.1, for the full model which accounts for miscentring, and including the (very small) correction for intrinsic scatter. The dotted lines show the  $1\sigma$  limits on this relation. As discussed in Section 4.4.2 the simple  $p_{cc} \equiv 1$  model, which assumes perfect cluster centres, yields the same slope, but a slightly lower overall normalization.

#### 4.4.1 Fits to $\Delta\Sigma$

We divide our cluster candidate catalogue into six richness bins, and measure the differential surface mass density as described in Section 4.3.2. The significances of the separate stacked measurements of  $\Delta\Sigma(R)$  shown in Figure 4.5 range from  $14.2\sigma$  to  $25.6\sigma$ , calculated using the full covariance matrices to include correlation between radial measurement bins. Error bars are calculated as the square root of the diagonal of the covariance matrices. These values, along with details of the richness bins and fits are given in Table 4.1. This yields a total 3D-MF cluster shear significance of  $\sim 54\sigma$ .

In modelling the halo mass, we use a composite-halo approach, which allows for the fact that the cluster candidates in a given stacked measurement may have a range of individual masses and redshifts. We emphasize that instead of fitting a single average mass (and also avoiding a single effective cluster redshift), we actually fit to the normalization of the mass-richness relation,  $M_0$ . We convert the array of cluster  $N_{200}$  values into masses with the equation

$$M_{200} = M_0 \left( \frac{N_{200}}{20} \right)^{1.5}. \quad (4.17)$$

In each separate stacked weak lensing measurement, we keep the slope of this mass-richness relation fixed, to avoid over-fitting to each stack with parameters that are quite degenerate within a narrow cluster bin. The NFW mass of each individual cluster is given by Equation 4.17, with the fixed slope of 1.5 from Ford et al. (2014), which will be shown to be consistent with the global mass-richness relation, measured and discussed in

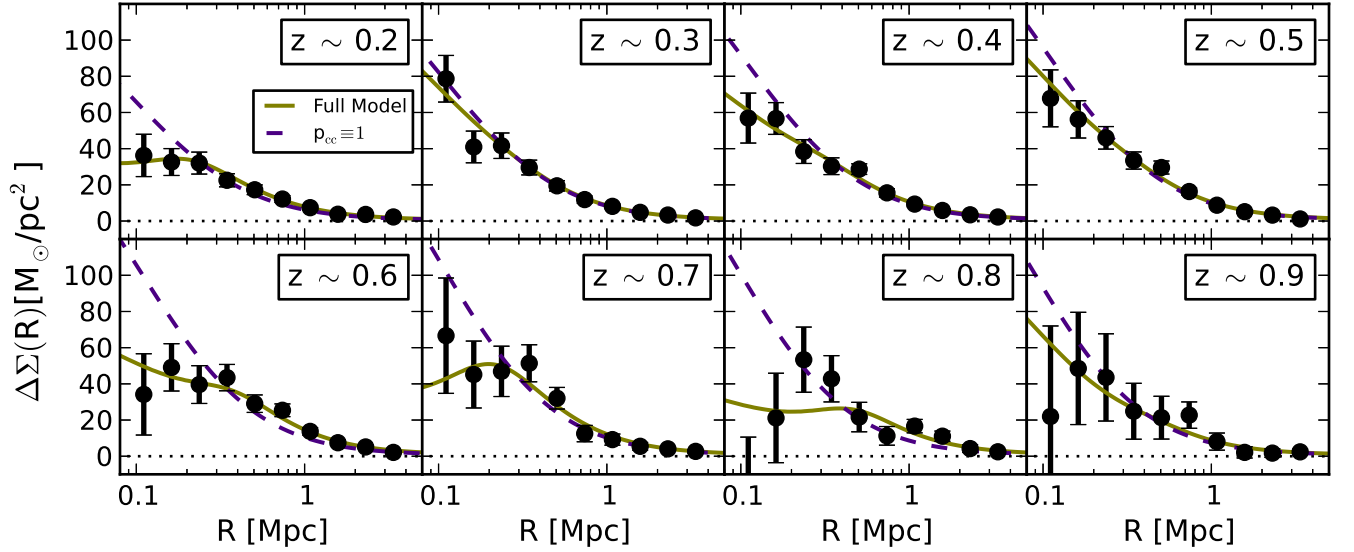


**Figure 4.8:** Best-fitting models for each stack of cluster candidates, this time binned in redshift. As in Figure 4.5, the solid green curves are the best fits to the full model given by Equation 4.16. The dashed purple curves are the best-fitting models which assumes that every cluster centre identified by 3D-MF is perfectly aligned with the dark matter halo centre. Tables 4.3 and 4.4 summarize the results of these fits.

Section 4.4.2 of this current work. We note that because of the free normalization  $M_0$ , this approach does neither impose the form of the richness distribution (Figure 4.2) nor does it set a prior on the individual mass.

We fit the halo model given in Equation 4.16 to the data, employing the downhill simplex method to minimize the generalized  $\chi^2$ , using the full covariance matrices estimated from bootstrap resampling. The results are displayed as the green curves in Figure 4.5 (labelled “Full Model”), and summarized in Table 4.1. The number of degrees of freedom for the model is 7 (10 radial bins minus 3 fit parameters).

To emphasize the importance of cluster miscentring, we also plot the best-fitting model where  $p_{cc} \equiv 1$  (i.e. perfect cluster centres) for comparison. This is shown as the dashed purple curves in Figure 4.5 (with a single fit parameter,  $M_0$ , this model has 9 degrees of freedom). Visual inspection reveals poor fits to the data at small radii for this model, and this fact is quantified by the reduced generalized  $\chi^2$  statistic ( $\chi^2_{red}$ ) values in Table 4.2. These results imply that cluster centroiding is an important component in the modelling of the 3D-MF weak lensing shear mass profiles, especially at the high mass (richness) end. For the majority of the rest of this work we will focus our attention on the results of the full model, which accounts for offset cluster centres.

The ensemble of cluster masses that result from the composite-halo modelling approach are displayed in Figure 4.6, where each panel represents a single stacked weak lensing measurement, congruent with Figure 4.5. This visual representation of the cluster mass function is largely distinct from the  $N_{200}$  histogram in Figure 4.2, because these masses are dependent upon the mass-richness normalization, as well as the miscentring parameters, which are fit to the measurements.

#### 4.4.2 The Mass-Richness Relation

The results of the previous section demonstrate a strong scaling of mass with richness. In Figure 4.7 we plot the average mass  $M_{200}$  measured in each richness bin, as a function of richness  $N_{200}$ , and fit the power law scaling

relation:

$$M_{200} = M_0 \left( \frac{N_{200}}{20} \right)^\beta. \quad (4.18)$$

This is similar to Equation 4.17, but the slope  $\beta$  is now a free parameter, and the mass-richness normalization  $M_0$  is fit across the full distribution of clusters. We note that the choice of  $\beta = 1.5$  in Equation 4.17 does not have a significant effect on the  $\beta$  measured here. Because of the degeneracy between  $\beta$  and  $M_0$  in each narrow cluster bin, a different choice of slope for the measurements in Section 4.4.1 still yields essentially the same mass estimates  $M_{200}$ , and thus the same global mass-richness relation.

Since galaxy clusters exhibit a natural intrinsic scatter between halo mass and richness (or other mass proxy), a bias in scaling relations can result if this scatter is ignored (Rozo et al., 2009a). The idea here is that while galaxy clusters at a given richness will scatter randomly with regard to their average mass, because of the shape of the cluster mass function, the net effect is to scatter from low to high mass. This can lead to a biased mass estimate in a given richness bin, as well as affect the global result for the mass-richness relation. We correct for intrinsic scatter using the data itself, following a procedure inspired by Velander et al. (2014), which is as follows.

We first fit Equation 4.18 to the uncorrected raw mass estimates from each richness bin, and use this power law relation to assign an individual mass to each cluster, based on its value of  $N_{200}$ . We then draw many “simulated” clusters from the observed cluster mass function (i.e. the  $N_{200}$  histogram in Figure 4.2), taking 1000 times as many “simulated” as observed clusters. We then scatter their masses by values drawn from a Gaussian in  $\ln(M_{200})$ , with width  $\sigma_{\ln M|N}$ , centred on the particular  $N_{200}$ . For the width of the intrinsic scatter, we use values estimated by Rozo et al. (2009a) for the MaxBCG clusters in the Sloan Digital Sky Survey (SDSS). This is  $\sigma_{\ln M|N} \sim 0.45$ , which is the scatter in the natural logarithm of mass, at fixed richness.

The resulting mass estimates are then used to calculate the corrected arithmetic mean mass in each of the richness bins, which are plotted in Figure 4.7 and used to re-fit Equation 4.18, yielding the final mass-richness relation reported below. The corrections applied to the mass estimates are at the sub-percent level, and therefore negligible compared to other sources of uncertainty in this work. Nevertheless, we include these small corrections when fitting for the mass-richness relation. We note that increasing  $\sigma_{\ln M|N}$  up to the 95% confidence limit reported by Rozo et al. (2009a) still does not affect the conclusions drawn in this work. A glance at Figure 4.6 justifies the low-impact of the intrinsic scatter correction, as most richness bins do not exhibit a very strong slope, which would otherwise lead to a larger effect on average mass in each bin.

In this work we measure  $M_0 = (2.7^{+0.5}_{-0.4}) \times 10^{13} M_\odot$  and  $\beta = 1.4 \pm 0.1$  for the full model (Figure 4.7), with a  $\chi^2_{\text{red}}$  of 0.9. For the perfectly centred model, we get  $M_0 = (2.2 \pm 0.2) \times 10^{13} M_\odot$  and  $\beta = 1.4 \pm 0.1$ , with a  $\chi^2_{\text{red}}$  of 1.0. (Note that uncertainties are larger on parameters estimated from the full model, both here and throughout this work, since there are simply more parameters than the perfectly-centred model). These results demonstrate that not including the centroid uncertainty in our analysis would lead us to systematically underestimate the cluster masses as well as the mass-richness normalization. Section 4.5.5 contains a thorough comparison of these results with our previous magnification measurements of these cluster candidates.

#### 4.4.3 Results of Binning Clusters in Redshift

We also investigate the weak lensing shear measurement of 3D-MF cluster candidates as a function of cluster redshift. 3D-MF sorts candidate clusters into bins of width  $\Delta z \sim 0.1$ , so these are natural bin choices, and

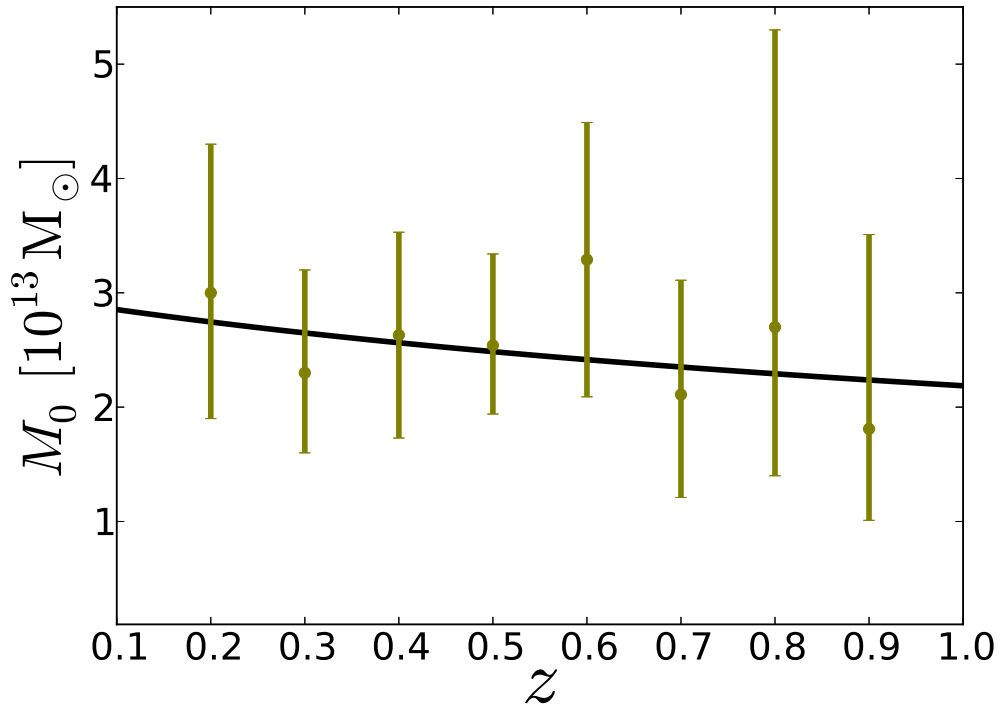


**Figure 4.9:** Normalization of the mass-richness relation  $M_0$  as a function of redshift  $z$ . The evidence for redshift evolution is not significant: the mildly negative slope is consistent with zero.

the same used in our previous analysis (Ford et al., 2014). Figure 4.8 shows the measurements and fits to  $\Delta\Sigma$ , with error bars again obtained from the covariance matrices (Section 4.3.2). The significance of the shear measurements reaches  $\sim 20\sigma$  at  $z \sim 0.5$ , where there is an abundance of 3D-MF cluster candidates, and drops to  $\sim 7\sigma$  at the highest redshifts, where shear signal-to-noise is depleted.

In Figure 4.8 (similar to Figure 4.5), we plot the full model in solid green, and the perfectly centred model in dashed purple. Table 4.3 and Table 4.4 display the results and fit parameters for these two models, respectively. The measurements at lower redshifts have an additional systematic error listed, which stems from uncertainties on the cluster redshifts, due to the way the 3D-MF method slices in redshift space (Ford et al., 2014). The 3D-MF cluster candidates are found to be quite similar in average mass across the range of redshift probed – we consistently obtain measurements of a few  $10^{13}M_\odot$ . The best-fitting miscentring parameter  $p_{cc}$  varies somewhat erratically as a function of redshift, but the error bars are too large to infer any significance from this. The width of the offset distribution on the other hand remains squarely at  $\sigma_{off} \sim 0.4$  arcmin. We discuss this result in relation to other cluster miscentring studies in Section 4.5.4.

We investigate possible redshift evolution of the mass-richness relation (given by Equation 4.18) in Figure 4.9, which shows the normalization of this scaling relation,  $M_0$ , as a function of redshift (with  $\beta = 1.5$  fixed), as listed in Table 4.3. We fit a powerlaw relation of the form

$$M_0(z) = M_0(z=0) \cdot [1+z]^\gamma. \quad (4.19)$$

We find a normalization  $M_0(z=0) = (3.0 \pm 0.6) \times 10^{13}M_\odot$ , and a powerlaw slope  $\gamma = -0.4^{+0.5}_{-0.6}$ . The slope is consistent with zero, so no significant redshift-evolution is detected for the 3D-MF mass-richness scaling relation.

## 4.5 Discussion

### 4.5.1 Interpretation of the Results

The 3D-MF clusters represent a wide range of halo masses and impose a significant shear signal on background galaxies. The measured  $\Delta\Sigma$  profiles from different stacked subsamples of clusters yield an important glimpse at the state of the dark matter haloes. We fit a model that includes parameters designed to distinguish the fraction of well-centred versus offset haloes, and the width of the offset distribution. The latter is consistently measured to peak at an offset of  $\sim 0.4$  arcmin, except for the richness bin  $40 < N_{200} \leq 60$ , for which we find a larger best fit of 1.3 arcmin (this much larger offset is puzzling, and will require follow-up to determine whether it is physical or perhaps a spurious effect of overfitting). The fraction of clusters that are not correctly centred is generally about 50% across richness bins, but has large error bars that do not allow us to distinguish interesting features at a statistically significant level. Nonetheless, we do find overall that the 3D-MF cluster halo profiles are better fitted by not enforcing perfect centroiding.

This study comprises several novel components, which will be discussed in more detail below. The large number of clusters, and the fact that 3D-MF does not assume anything about cluster galaxy colours, makes the uniqueness of the data set valuable in its own right. Evolution of the normalization of the mass-richness relation across a wide span of redshift has only been constrained previously by van Uitert (2012) and Andreon and Congdon (2014). The direct comparison between shear and magnification measured masses is a first for a cluster catalogue of this volume. There are several caveats to the implications of this work, notably the very likely presence of false-detections at the low-significance (low-richness) end of the cluster candidate spectrum.

### 4.5.2 Comparisons of Cluster Catalogue Volume

The most noteworthy aspect of the CFHTLS-Wide 3D-MF cluster catalogue is its sheer size. With over 100 cluster candidates per square degree (18056 clusters in  $154 \text{ deg}^2$ ), spanning redshifts up to  $z \sim 0.9$ , this compilation of cluster candidates is one of the most complete available. We encourage others to utilize this catalogue, available from [cfhtlens.org](http://cfhtlens.org), as there are an abundance of scientific investigations now possible with it.

The current widest survey with a galaxy cluster catalogue is SDSS. The SDSS collaboration found 13823 galaxy groups and clusters spread over  $7500 \text{ deg}^2$ , using their maxBCG method (Koester et al., 2007). This amounts to less than two clusters per  $\text{deg}^2$ , and is restricted to lower redshifts ( $0.1 < z < 0.3$ ). The maxBCG technique relies on finding potential bright galaxies and searching around them for the presence of a red sequence in colour-magnitude space (which would indicate the presence of red, elliptical galaxies, common in galaxy clusters).

Interestingly, visual inspection of 3D-MF galaxy cluster candidates shows that the lower redshift clusters often do have a bright central galaxy, but this is less true at higher redshifts. It would be interesting to quantify this aspect in future work, especially when an opportunity presents itself to compare 3D-MF to other algorithms directly, by running both on the same optical data set. Galaxy clusters do not always have one brightest central galaxy, and if they do have one, it is not always exactly in the centre of the galaxy cluster, so comparing the biases of both methods could ultimately result in a more complete cluster list, or could potentially show the limitations of methods like maxBCG.

Several cluster catalogues have been compiled in the CFHTLS-Wide. Durret et al. (2011) used photometric redshift information to construct galaxy density maps in CFHTLS, building upon earlier work by Adami et al.



(2010) and Mazure et al. (2007). They found 4061 cluster candidates in the Wide fields, with masses greater than about  $10^{14}M_{\odot}$ , spanning redshifts  $0.1 \leq z \leq 1.15$ . Shan et al. (2012) used a 3D-lensing approach, with convergence maps and galaxy photometric redshifts, to detect 85 clusters at  $\langle z \rangle \sim 0.36$  in the W1 field of the CFHTLS-Wide.

Wen et al. (2012) compiled an optical cluster catalogue from SDSS-III, using galaxy photometric redshifts and a friends-of-friends algorithm. They found an impressive 132684 clusters over  $14000 \text{ deg}^2$  in a redshift range  $0.05 \leq z < 0.8$ . A recent cluster shear analysis was done by Covone et al. (2014), using the overlapping portion of the Wen et al. (2012) catalogue, with the CFHTLenS shear catalogue. To date, this is the most complete cluster catalogue analysed in the context of CFHTLenS, but still the cluster density is  $\leq 1/10$ th of that achieved with 3D-MF. A comparison of 3D-MF with the cluster catalogues compiled using these different techniques will be presented in a future analysis.

### 4.5.3 Comparison with other Mass-Richness Relations

The 3D-MF cluster finder presents us with a sample of cluster candidates which, like every other cluster-finder, are drawn from a somewhat unique distribution defined by its particular selection function. Despite the difficulties inherent to making exact comparisons between scaling relations measured on disparate cluster samples, we attempt a broad look at how the 3D-MF mass-richness scaling compares to other relations in the literature.

Wen et al. (2009) defined a measure of richness  $R$  for their SDSS clusters, which is somewhat similar to the  $N_{200}$  used in this work. They counted all galaxies brighter than absolute magnitude  $M_r \leq -21$ , within a 1 Mpc radius and  $\Delta z < 0.04(1+z)$ . Converting their mass-richness relation to the form of ours (Equation 4.18), they obtained a somewhat steeper slope  $\beta \sim 1.9$ , and a higher normalization  $M_0 \sim 2.5 \times 10^{14}M_{\odot}$  than the best-fitting models presented in this work (*Full Model*:  $M_0 \sim 2.7 \times 10^{13}M_{\odot}$ ,  $\beta \sim 1.4$ ). We tried measuring richness for the 3D-MF clusters following the same prescription as Wen et al. (2009), but found the one-size-fits-all radius to be a serious limitation for our sample, since the 3D-MF cluster candidates span a wide range of masses and therefore characteristic radii. The resulting richness estimates had greatly enhanced scatter and did not scale well with mass at the more massive end of the cluster catalogue.

In a follow-up paper, Wen et al. (2012) defined a new richness  $R_{L*}$  – the total r-band luminosity within  $R_{200}$  in units of  $L_{\odot}$ . For the portion of clusters with previously measured masses (weak lensing or X-ray), a scaling between the radius  $R_{200}$  derived from these masses and the luminosity within 1 Mpc was measured, and this was used to estimate radii for calculating  $R_{L*}$  for the full sample of 132684 clusters. For the subsample with existing mass estimates, Wen et al. (2012) found a mass-richness relation with normalization  $M_0 \sim 1.1 \times 10^{14}M_{\odot}$  and slope  $\beta \sim 1.2$  (again converting to the form of our Equation 4.18). Covone et al. (2014) measured weak lensing masses for 1176 of the clusters from Wen et al. (2012), which overlapped with CFHTLenS. They found a very similar mass-richness scaling, with  $M_0 \sim 10^{14}M_{\odot}$  and  $\beta \sim 1.2$ .

The mass-richness slope of the 3D-MF cluster candidates sits squarely between the results of Wen et al. (2009), using the  $R$  richness, and Wen et al. (2012) and Covone et al. (2014), which used the  $R_{L*}$  measure. The 3D-MF normalization is lower than the other cluster catalogues, which could partly be a result of 3D-MF detecting more lower mass clusters missed by other finders. However, the different definition of richness, namely the fainter limit on galaxies contributing to  $N_{200}$ , means that the same mass cluster will have a larger measured richness in this work, implying a lower mass-richness normalization. Finally, the presence of false detections in the 3D-MF catalogue (estimated from simulations to be at the level of 16 – 24%) would certainly bias the mass

estimates low.

Johnston et al. (2007) used a quite different definition of richness for the maxBCG clusters, counting only red-sequence galaxies brighter than  $0.4L_*$ , within an  $R_{200}^{\text{gals}}$  that was estimated from the number of galaxies within 1 Mpc (following a prescription in Hansen et al., 2005). Weak lensing masses were used to find a normalization  $M_0 \sim 1.3 \times 10^{14} M_\odot$  and slope  $\beta \sim 1.3$ . Rozo et al. (2009b) created updated richness estimates of the maxBCG clusters by applying an improved colour modelling of cluster members, and allowing individual cluster radii to vary until the scatter between richness and X-ray luminosity was minimized.

Andreon and Hurn (2010) defined a measure of richness for the Cluster Infall Regions in SDSS catalogue, for which masses  $M_{200}$  and radii  $R_{200}$  were already available (from application of the caustic technique). They studied a sample of 53 low-redshift clusters, in the range  $0.03 < z < 0.1$ , and their  $N_{200}$  included all red galaxies brighter than  $M_V = -20$  within the radius  $R_{200}$ . In a follow-up analysis they measured a tight mass-richness scaling relation with normalization  $M_0 \sim 1.4 \times 10^{11} M_\odot$  and slope  $\beta \sim 2.1$  (Andreon and Bergé, 2012).

The addition of the galaxy colour information in the richness estimate of the previous three examples, in particular, creates difficulty in drawing meaningful comparisons between their mass-richness scaling relation and the 3D-MF scaling relation. We emphasize that the value of any mass-richness relation is limited to the particular cluster sample for which it was derived, which in turn depends on the cluster-finding algorithm and details of the survey on which the catalogue was compiled. As discussed in Rozo et al. (2009b), the simple fact that estimates of richness are readily available in an optical cluster survey, and that they can be applied to clusters of virtually any mass, nevertheless makes richness a worthwhile parameter to measure. So although richness has many different definitions, and some unavoidable scatter in its scaling relations with various cluster mass estimates, it remains a useful tool for characterizing galaxy clusters.

#### 4.5.4 Comparisons with other Cluster Centroid Analyses

We find the distribution of centroid offsets to be well characterized by a Gaussian of width  $\sigma_{\text{off}} \sim 0.4$  arcmin,<sup>2</sup> and that this miscentring has an effect on a significant portion of the candidate clusters (up to  $\sim 80\%$  of them are affected, see Table 4.1). Interestingly, previous studies applying 3D-MF to simulations yielded an average  $\sigma_{\text{off}} = 0.40 \pm 0.06$  arcmin (see Figure 1 in Ford et al., 2014), which is easily consistent with the best-fitting offset measured on the real 3D-MF cluster candidates in this work.

The maxBCG clusters were found to have centroid offsets around  $0.42 h^{-1} \text{Mpc}$ , based on simulations (Johnston et al., 2007), which is several times larger than the ones measured for the 3D-MF cluster candidates. There were large uncertainties associated with the probability of a cluster having a correct centroid selected, but this was determined to be approximately  $\geq 50\%$  (see Figure 5 in Johnston et al., 2007), which is similar to  $p_{cc}$  found in this work. George et al. (2012) performed a miscentring analysis of X-ray groups in the COSMOS field. They found offsets of  $\sim 20 - 70$  kpc, for different candidate centres, which are smaller than measured for 3D-MF clusters.

It is worth noting that candidate cluster centres that are coincident with a member galaxy have been found to better trace the halo’s centre of mass, relative to other types of centroids such as X-ray, or various weighted centres of galaxy positions (George et al., 2012). See also Bildfell et al. (2008) for a study of massive X-ray clusters. 3D-MF centres (peaks in the likelihood map) do not necessarily coincide with a cluster galaxy member, so future work should investigate various possible candidate centres to find the one that best traces the centre of

<sup>2</sup>For comparisons,  $0.4$  arcmin  $\sim 147$  kpc at redshift  $0.5$

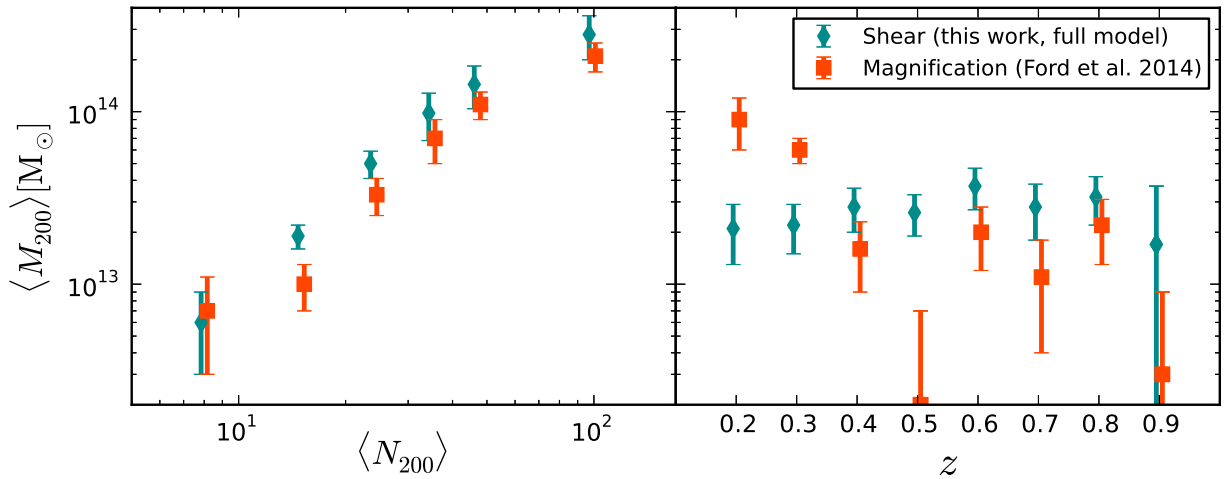


**Figure 4.10:** Here we compare the mass measurements obtained for the 3D-MF cluster candidates using weak lensing shear (i.e. this work) with the results obtained measuring the masses with the lensing magnification technique (the  $N_{200}$  estimates from that work, Ford et al., 2014, are used in this plot for the purposes of comparison). The first panel compares mass measurements when cluster candidates are binned in richness  $N_{200}$ , and the second panel shows the redshift  $z$  binning. Bins are identical for magnification and for shear, but the points are slightly offset horizontally for clarity. Blue diamonds represent the shear, and orange squares are for magnification.

mass for 3D-MF cluster haloes.

#### 4.5.5 Comparison with Magnification Results

One of the most interesting aspects of this work is the direct comparison between magnification and shear mass estimates, which is now made possible in the context of a very large lens sample. Prior to this work, the only observational magnification–shear direct cluster mass comparison in the literature was Ford et al. (2012). That study demonstrated a  $1\sigma$  consistency between masses measured with the two techniques, but applied to a small sample of just 44 galaxy groups, so any trends in cluster size or redshift were unable to be explored. Huff and Graves (2014) compared magnification and shear masses for SDSS galaxy lenses, using a different and novel approach to measuring lensing magnification, and found mass profiles to be within a factor 3 of agreement.

Important work related to the *joint* analysis of shear and magnification has been developed in Umetsu et al. (2011) and Umetsu (2013). Umetsu et al. (2014) combined shear and magnification to measure the mass profiles of 20 massive X-ray-selected clusters. This work demonstrated that the geometric mean mass of the shear+magnification measurement was consistent with the shear-only measurement, but did not show magnification results on their own. Earlier work in Umetsu et al. (2011) compared the signal-to-noise of the magnification and shear, but did not present mass estimates from separate analyses.

In this work we exploit the volume of the 3D-MF cluster catalogue to fully compare masses determined with each of the independent techniques, as a function of both candidate cluster richness and redshift. The findings are summarized in Figure 4.10. For consistency in the comparison, this plot uses the original  $N_{200}$  estimates from Ford et al. (2014), so that the cluster candidate stacks in each richness bin are identical. Also, in this section only, we use the mass-concentration relation of Prada et al. (2012), in identical fashion to the magnification work. The Prada et al. (2012) relation is in excellent agreement with recent measurements by Covone et al. (2014) of the

masses and concentrations of a cluster sample in CFHTLenS, although it is in tension with other measurements such as Merten et al. (2014).

The left-hand panel of Figure 4.10 displays the results when 3D-MF cluster candidates are stacked across all redshifts. The average of the composite-halo masses fit to each stack is comparable between the two methods, but the magnification estimates are systematically lower than the shear estimates. This yields a mass-richness normalization which is about  $2\sigma$  higher for the shear method, although the slope of the relation recovered with the two techniques is essentially identical. The magnification measurements yielded  $M_0 = (2.2 \pm 0.2) \times 10^{13} M_\odot$  and  $\beta = 1.5 \pm 0.1$  (see the miscentred model in Ford et al., 2014), while the shear measurements here give  $M_0 = (3.1 \pm 0.5) \times 10^{13} M_\odot$  and  $\beta = 1.5 \pm 0.2$ . We note that the mass-richness relation parameters obtained from the shear measurements in Figure 4.10 are consistent within  $1\sigma$  with the new mass-richness parameters obtained with shear in Figure 4.7 and discussed in Section 4.4.2. We reiterate that the slight difference between the shear measurements in Figures 4.7 and 4.10 is due to a recalibration of the cluster  $N_{200}$  estimates (see Section 4.2.3) and a different choice of mass-concentration relation.

It is important to note that in both of the aforementioned magnification studies (Ford et al., 2012, 2014), the background source sample is completely distinct from the background sources used to measure shear. Indeed, both magnification results used magnified Lyman-break galaxies, which are point-like sources whose negligible apparent size would not permit a measurement of the shear. In this sense, the magnification results are largely independent from the shear measurements to which they are compared, having only the lens population in common. We note that alternative methods of measuring magnification using source size information would instead tend to use the same source sample employed for measuring shear.

The comparison becomes more interesting as a function of redshift, shown in the right-hand panel of Figure 4.10. Here we see that the shear-measured average mass of cluster candidates does not vary as a function of redshift, while the magnification masses fluctuate. In Ford et al. (2014), we discussed this behaviour of the magnification signal, but without an alternative mass determination were not able to conclude whether this variation communicated an intrinsic property of the 3D-MF cluster candidates, or was an artefact of the magnification measurement. We are still unable to say with certainty whether the masses of the 3DMF cluster sample truly are constant or evolving across the redshift range, as suggested by the conflicting shear and magnification measurements. Here, we discuss several possible reasons for these discrepant redshift-binned results.

First of all, the distributions of richness values for the separate  $z$  slices are very similar, with the lower redshift slices containing relatively higher fractions of low-richness cluster candidates (see Figure 7 in Ford et al., 2014). So if (1) richness is a good estimator for mass, which it appears to be given the strong scaling, and (2) the mass-richness relation does not evolve strongly with redshift over the range  $z \sim 0.5 \rightarrow 0.2$ , then we would expect similar masses across this range, or for masses to actually decrease at lower redshift in concordance with the lower mean cluster  $N_{200}$  (i.e. the opposite of the trend suggested by magnification).

As discussed in detail in Ford et al. (2014), at  $z \sim 0.2 - 0.3$  the magnification measurement is expected to be affected by some low- $z$  contamination in the Lyman-break galaxy source sample. In that work we attempted to compensate for this effect by including a term in the modelling of the measured signal, to account for physical clustering where the populations overlapped. A crucial assumption was the actual fraction of contaminated sources, which was estimated using a cross-correlation technique with foreground galaxies (Hildebrandt et al., in preparation). If these fractions were biased low, then much of the physical clustering signal would have been interpreted as due to magnification, leading to mass estimates that were too high (at low- $z$ ).

Currently, we are also investigating the influence of several other systematic effects on our magnification measurements. In particular, we are studying how the varying depth and the varying seeing of the survey affect different lens and source samples, and how stellar contamination (or also just the light haloes of stars) and galactic dust can alter the magnification signal. This in-depth analysis of systematic effects will be presented in a forthcoming paper (Morrison et al., in preparation) and might provide additional insight into the apparent redshift dependence of the cluster magnification signal reported in Ford et al. (2014). Another possibility may be related to the masking effect of cluster galaxy members, which is survey dependent and can affect both magnification and shear measurements (Simet and Mandelbaum, 2014). This sky obscuration could lead to our magnification masses being biased low, but our shear measurements should be robust because of the stringent criteria used for selecting background galaxies (Section 4.3.2).

In order for magnification to yield robust results that encourage its employment in the next generation of large surveys, this discrepancy needs to be addressed. Studies that compare shear and magnification measurements for large binned lens and source samples are crucial for teasing out these underlying systematics.

## 4.6 Conclusions

This work has presented weak lensing shear results, measured at  $54\sigma$  significance, for a new catalogue of cluster candidates detected by the 3D-MF algorithm. 3D-MF is a three-dimensional advancement of older matched-filter techniques, which automatically searches wide and deep optical data for galaxy clusters across a range of redshifts. Given a sensible luminosity and radial profile, 3D-MF is able to search within data for a range of galaxy cluster masses. By construction, 3D-MF has allowed us to find lower mass cluster candidates (and groups) which other popular techniques, such as the red sequence and maxBCG, may not be capable of finding.

3D-MF was run on the CFHTLS-Wide fields using galaxy photometric redshifts and  $i'$ -band data for cluster luminosity profiles, producing one of the largest and most complete cluster catalogues currently available. 18056 cluster candidates were detected with a significance  $\geq 3.5$  and richness  $N_{200} > 2$ , out to a redshift of 0.9 ( $>100/\text{deg}^2$ ). Many of these cluster candidates are in the lower mass ranges (down to  $\leq 10^{13}M_{\odot}$ ), which is notably a larger low mass sample than currently exists from deep, wide surveys in the literature, offering an enormous opportunity for further study.

The CFHTLS-Wide 3D-MF catalogue was investigated to learn more about candidate cluster properties, such as masses and centroiding, as well as to follow up on previous results applying the less developed technique of lensing magnification to this cluster sample (Ford et al., 2014). Shear profiles were measured around cluster candidates, which were stacked as a function of richness and redshift, and we focused on presenting composite-halo model fits to measurements of the differential surface mass density  $\Delta\Sigma$ .

Careful consideration of potential miscentring of galaxy clusters by 3D-MF had to be taken into account in the analysis. We fit the data with smoothed shear profiles,  $\Delta\Sigma^{\text{sm}}$ , that describe a cluster whose halo is offset from its assumed centre. The fraction of clusters that are affected by miscentring, as well as the probability distribution of the offsets, were both allowed to vary in the modelling. We found the inclusion of these parameters to significantly improve the  $\chi^2$  of the cluster profile fits, relative to a perfectly centred model for  $\Delta\Sigma$ , which we also demonstrated for comparison. The stacked cluster shear measurements were well fitted by a model in which about half the clusters are affected by miscentring ( $p_{\text{cc}} \sim 0.5$ ), with the distribution of centroid offsets peaking at  $\sim 0.4$  arcmin.

The large sample of cluster candidates in this work allowed us to bin the shear measurements as a function

of both richness and redshift. The average cluster candidate masses were found to be relatively constant with redshift, estimated at 2 to  $4 \times 10^{13} M_{\odot}$ . The masses scaled strongly with richness, ranging from  $\sim 6 \times 10^{12} M_{\odot}$  to  $\sim 3 \times 10^{14} M_{\odot}$ . We measured the normalization and slope of the mass-richness relation for the 3D-MF cluster candidates, finding  $M_0 = (2.7^{+0.5}_{-0.4}) \times 10^{13} M_{\odot}$  and  $\beta = 1.4 \pm 0.1$ . The redshift dependence of the normalization  $M_0(z)$  was not significant, yielding a powerlaw slope in  $(1+z)$  of  $-0.4^{+0.5}_{-0.6}$ .

The masses of individual cluster candidates were found to range from a small group scale, with stacked average masses of less than  $10^{13} M_{\odot}$ , all the way up to a few very massive clusters, at several  $10^{15} M_{\odot}$ . Since the 3D-MF catalogue has not been followed up spectroscopically, we expect some fraction of false-detections (estimated between  $\sim 16$  and  $24\%$  from simulations), which would lead to these mass estimates being biased low, and would especially affect the low-richness stacked measurements. We note, however, that the impact of false detections may be less severe than implied, if line-of-sight projections are significant. Chance alignments of low-mass structures would have a similar effect on a shear measurement (which probes surface mass density) as it would on an estimate of optical cluster properties like richness.

By design, we binned cluster candidates in an identical fashion to the previous magnification study (Ford et al., 2014), and compared the results obtained. This is the first large study directly comparing the outcomes of magnification and shear on the same lens sample. When stacked across all redshifts, we found that the average masses derived within a given richness bin were similar (within  $1\sigma$ ), but magnification masses were systematically lower, yielding a  $2\sigma$  difference in the normalization of the mass-richness relation derived from the two techniques. The mass-richness slope was essentially identical for magnification and for shear. The comparison across redshift slices yielded very interesting insights into problems that may still exist for magnification. The fact that the shear-determined masses were roughly constant across redshift led us to conclude that the magnification measurement (using magnification-biased number counts of Lyman-break galaxy sources) may still suffer from residual systematics at low- $z$ . Notably, however, this occurs at very predictable lens redshifts, so if one has accurate photometric redshift distributions for the sources, these contaminated redshift zones could potentially be avoided.

In future work, it would be interesting to apply various cluster finding algorithms to the *same* large data set in order to compare the capabilities of the finders, potentially increase the overall cluster sample and reduce its biases, or even just to compare how different search algorithms perform. This could ideally lead to more complete and unbiased cluster samples. Current surveys, such as the Kilo-Degree Survey (de Jong et al., 2013), the Subaru Hyper Suprime-Cam Project (Takada, 2010), and the Dark Energy Survey (The Dark Energy Survey Collaboration, 2005) for example, are large enough that cluster masses and concentrations will be measured quite accurately as a function of redshift and richness. The area of these surveys is an order of magnitude higher than the CFHTLS-Wide, and high precision cluster profiling will naturally continue to evolve alongside these surveys.

The CFHTLS-Wide 3D-MF galaxy cluster catalogue contains 18056 cluster candidates, over a wide range of mass and redshift, and is now publicly available at [cfhtlens.org](http://cfhtlens.org). We encourage others to make use of the rich science opportunities afforded by this catalogue.

## **Chapter 5**

# **Conclusions**

### **5.1 Summary and Conclusions**

### **5.2 Future Work**

# Bibliography

- C. Adami, F. Durret, C. Benoist, J. Coupon, A. Mazure, B. Meneux, O. Ilbert, J. Blaizot, S. Arnouts, A. Cappi, B. Garilli, L. Guennou, V. Lebrun, O. Lefèvre, S. Maurogordato, H. J. McCracken, Y. Mellier, E. Slezak, L. Tresse, and M. P. Ulmer. Galaxy structure searches by photometric redshifts in the CFHTLS. *A&A*, 509: A81, Jan. 2010. doi:10.1051/0004-6361/200913067. → pages 45, 63
- S. Andreon and J. Bergé. Richness-mass relation self-calibration for galaxy clusters. *A&A*, 547:A117, Nov. 2012. doi:10.1051/0004-6361/201220115. → pages 65
- S. Andreon and P. Congdon. The insignificant evolution of the richness-mass relation of galaxy clusters. *A&A*, 568:A23, Aug. 2014. doi:10.1051/0004-6361/201423616. → pages 63
- S. Andreon and M. A. Hurn. The scaling relation between richness and mass of galaxy clusters: a Bayesian approach. *MNRAS*, 404:1922–1937, June 2010. doi:10.1111/j.1365-2966.2010.16406.x. → pages 65
- J. Audouze and J. Tran Thanh Van, editors. *Formation and evolution of galaxies and large structures in the universe; Proceedings of the Third Moriond Astrophysics Meeting, La Plagne, France, March 1983*, volume 117 of *NATO Advanced Science Institutes (ASI) Series C*, 1984. → pages 3
- M. W. Auger, T. Treu, A. S. Bolton, R. Gavazzi, L. V. E. Koopmans, P. J. Marshall, L. A. Moustakas, and S. Burles. The Sloan Lens ACS Survey. X. Stellar, Dynamical, and Total Mass Correlations of Massive Early-type Galaxies. *ApJ*, 724:511–525, Nov. 2010. doi:10.1088/0004-637X/724/1/511. → pages 8
- H. W. Babcock. The rotation of the Andromeda Nebula. *Lick Observatory Bulletin*, 19:41–51, 1939. doi:10.5479/ADS/bib/1939LicOB.19.41B. → pages 3
- M. Bartelmann and P. Schneider. Weak gravitational lensing. *Phys. Rep.*, 340:291–472, Jan. 2001. doi:10.1016/S0370-1573(00)00082-X. → pages 2, 3, 7, 9, 11, 12, 18, 27, 33
- A. H. Bauer, S. Seitz, J. Jerke, R. Scalzo, D. Rabinowitz, N. Ellman, and C. Baltay. Measuring Lensing Magnification of Quasars by Large Scale Structure Using the Variability-Luminosity Relation. *ApJ*, 732:64, May 2011. doi:10.1088/0004-637X/732/2/64. → pages 28
- A. H. Bauer, E. Gaztañaga, P. Martí, and R. Miquel. Magnification of photometric LRGs by foreground LRGs and clusters in the Sloan Digital Sky Survey. *MNRAS*, 440:3701–3713, June 2014. doi:10.1093/mnras/stu530. → pages 46
- G. Bertone, D. Hooper, and J. Silk. Particle dark matter: evidence, candidates and constraints. *Phys. Rep.*, 405: 279–390, Jan. 2005. doi:10.1016/j.physrep.2004.08.031. → pages 4
- C. Bildfell, H. Hoekstra, A. Babul, and A. Mahdavi. Resurrecting the red from the dead: optical properties of BCGs in X-ray luminous clusters. *MNRAS*, 389:1637–1654, Oct. 2008. doi:10.1111/j.1365-2966.2008.13699.x. → pages 65
- A. S. Bolton, S. Burles, L. V. E. Koopmans, T. Treu, R. Gavazzi, L. A. Moustakas, R. Wayth, and D. J. Schlegel. The Sloan Lens ACS Survey. V. The Full ACS Strong-Lens Sample. *ApJ*, 682:964–984, Aug. 2008. doi:10.1086/589327. → pages 8



- S. Bridle, J. Shawe-Taylor, A. Amara, D. Applegate, J. S. T. Balan, Berge, G. Bernstein, H. Dahle, T. Erben, M. Gill, A. Heavens, C. Heymans, F. W. High, H. Hoekstra, M. Jarvis, D. Kirk, T. Kitching, J.-P. Kneib, K. Kuijken, D. Lagatutta, R. Mandelbaum, R. Massey, Y. Mellier, B. Moghaddam, Y. Moudén, R. Nakajima, S. Paulin-Henriksson, S. Pires, A. Rassat, A. Refregier, J. Rhodes, T. Schrabbach, E. Semboloni, M. Shmakova, L. van Waerbeke, D. Witherick, L. Voigt, and D. Wittman. Handbook for the GREAT08 Challenge: An image analysis competition for cosmological lensing. *Annals of Applied Statistics*, 3:6–37, 2009. doi:10.1214/08-AOAS222. → pages 17
- T. J. Broadhurst, A. N. Taylor, and J. A. Peacock. Mapping cluster mass distributions via gravitational lensing of background galaxies. *ApJ*, 438:49–61, Jan. 1995. doi:10.1086/175053. → pages 14, 15
- I. W. A. Browne, P. N. Wilkinson, N. J. F. Jackson, S. T. Myers, C. D. Fassnacht, L. V. E. Koopmans, D. R. Marlow, M. Norbury, D. Rusin, C. M. Sykes, A. D. Biggs, R. D. Blandford, A. G. de Bruyn, K.-H. Chae, P. Helbig, L. J. King, J. P. McKean, T. J. Pearson, P. M. Phillips, A. C. S. Readhead, E. Xanthopoulos, and T. York. The Cosmic Lens All-Sky Survey - II. Gravitational lens candidate selection and follow-up. *MNRAS*, 341:13–32, May 2003. doi:10.1046/j.1365-8711.2003.06257.x. → pages 8
- P. Capak, H. Aussel, M. Ajiki, H. J. McCracken, B. Mobasher, N. Scoville, P. Shopbell, Y. Taniguchi, D. Thompson, S. Tribiano, S. Sasaki, A. W. Blain, M. Brusa, C. Carilli, A. Comastri, C. M. Carollo, P. Cassata, J. Colbert, R. S. Ellis, M. Elvis, M. Giavalisco, W. Green, L. Guzzo, G. Hasinger, O. Ilbert, C. Impey, K. Jahnke, J. Kartaltepe, J.-P. Kneib, J. Koda, A. Koekemoer, Y. Komiyama, A. Leauthaud, O. Le Fevre, S. Lilly, C. Liu, R. Massey, S. Miyazaki, T. Murayama, T. Nagao, J. A. Peacock, A. Pickles, C. Porciani, A. Renzini, J. Rhodes, M. Rich, M. Salvato, D. B. Sanders, C. Scarlata, D. Schiminovich, E. Schinnerer, M. Scodeggio, K. Sheth, Y. Shioya, L. A. M. Tasca, J. E. Taylor, L. Yan, and G. Zamorani. The First Release COSMOS Optical and Near-IR Data and Catalog. *ApJS*, 172:99–116, Sept. 2007. doi:10.1086/519081. → pages 20
- D. Clowe, M. Bradač, A. H. Gonzalez, M. Markevitch, S. W. Randall, C. Jones, and D. Zaritsky. A Direct Empirical Proof of the Existence of Dark Matter. *ApJ*, 648:L109–L113, Sept. 2006. doi:10.1086/508162. → pages 3
- A. Cooray and R. Sheth. Halo models of large scale structure. *Phys. Rep.*, 372:1–129, Dec. 2002. doi:10.1016/S0370-1573(02)00276-4. → pages 55
- G. Covone, M. Sereno, M. Kilbinger, and V. F. Cardone. Measurement of the Halo Bias from Stacked Shear Profiles of Galaxy Clusters. *ApJ*, 784:L25, Apr. 2014. doi:10.1088/2041-8205/784/2/L25. → pages 46, 54, 64, 66
- P. Cushman, C. Galbiati, D. N. McKinsey, H. Robertson, T. M. P. Tait, D. Bauer, A. Borgland, B. Cabrera, F. Calaprice, J. Cooley, T. Empl, R. Essig, E. Figueroa-Feliciano, R. Gaitskell, S. Golwala, J. Hall, R. Hill, A. Hime, E. Hoppe, L. Hsu, E. Hungerford, R. Jacobsen, M. Kelsey, R. F. Lang, W. H. Lippincott, B. Loer, S. Luitz, V. Mandic, J. Mardon, J. Maricic, R. Maruyama, R. Mahapatra, H. Nelson, J. Orrell, K. Palladino, E. Pantic, R. Partridge, A. Ryd, T. Saab, B. Sadoulet, R. Schnee, W. Shepherd, A. Sonnenschein, P. Sorensen, M. Szydagis, T. Volansky, M. Witherell, D. Wright, and K. Zurek. Snowmass CF1 Summary: WIMP Dark Matter Direct Detection. *ArXiv e-prints*, Oct. 2013. → pages 3
- N. Dalal and C. S. Kochanek. Direct Detection of Cold Dark Matter Substructure. *ApJ*, 572:25–33, June 2002. doi:10.1086/340303. → pages 8
- J. T. A. de Jong, G. A. Verdoes Kleijn, K. H. Kuijken, and E. A. Valentijn. The Kilo-Degree Survey. *Experimental Astronomy*, 35:25–44, Jan. 2013. doi:10.1007/s10686-012-9306-1. → pages 69
- G. De Lucia and J. Blaizot. The hierarchical formation of the brightest cluster galaxies. *MNRAS*, 375:2–14, Feb. 2007. doi:10.1111/j.1365-2966.2006.11287.x. → pages 30

- J. P. Dietrich, Y. Zhang, J. Song, C. P. Davis, T. A. McKay, L. Baruah, M. Becker, C. Benoist, M. Busha, L. A. N. da Costa, J. Hao, M. A. G. Maia, C. J. Miller, R. Ogando, A. K. Romer, E. Rozo, E. Rykoff, and R. Wechsler. Orientation bias of optically selected galaxy clusters and its impact on stacked weak-lensing analyses. *MNRAS*, 443:1713–1722, Sept. 2014. doi:10.1093/mnras/stu1282. → pages 50
- S. Dodelson. *Modern cosmology*. 2003. → pages 3, 5, 10
- F. Durret, C. Adami, A. Cappi, S. Maurogordato, I. Márquez, O. Ilbert, J. Coupon, S. Arnouts, C. Benoist, J. Blaizot, T. M. Ederh, B. Garilli, L. Guennou, V. Le Brun, O. Le Fèvre, A. Mazure, H. J. McCracken, Y. Mellier, C. Mezrag, E. Slezak, L. Tresse, and M. P. Ulmer. Galaxy cluster searches based on photometric redshifts in the four CFHTLS Wide fields. *A&A*, 535:A65, Nov. 2011. doi:10.1051/0004-6361/201116985. → pages 63
- A. A. Dutton and A. V. Macciò. Cold dark matter haloes in the Planck era: evolution of structural parameters for Einasto and NFW profiles. *MNRAS*, 441:3359–3374, July 2014. doi:10.1093/mnras/stu742. → pages 52, 55
- T. Erben, H. Hildebrandt, M. Lerchster, P. Hudelot, J. Benjamin, L. van Waerbeke, T. Schrabback, F. Brimiouille, O. Cordes, J. P. Dietrich, K. Holhjem, M. Schirmer, and P. Schneider. CARS: the CFHTLS-Archive-Research Survey. I. Five-band multi-colour data from 37 sq. deg. CFHTLS-wide observations. *A&A*, 493:1197–1222, Jan. 2009. doi:10.1051/0004-6361:200810426. → pages 46
- T. Erben, H. Hildebrandt, L. Miller, L. van Waerbeke, C. Heymans, H. Hoekstra, T. D. Kitching, Y. Mellier, J. Benjamin, C. Blake, C. Bonnett, O. Cordes, J. Coupon, L. Fu, R. Gavazzi, B. Gillis, E. Grocutt, S. D. J. Gwyn, K. Holhjem, M. J. Hudson, M. Kilbinger, K. Kuijken, M. Milkeraitis, B. T. P. Rowe, T. Schrabback, E. Semboloni, P. Simon, M. Smit, O. Toader, S. Vafaei, E. van Uitert, and M. Velander. CFHTLenS: the Canada-France-Hawaii Telescope Lensing Survey - imaging data and catalogue products. *MNRAS*, 433: 2545–2563, Aug. 2013. doi:10.1093/mnras/stt928. → pages 28, 46, 47
- D. J. Fixsen, E. S. Cheng, J. M. Gales, J. C. Mather, R. A. Shafer, and E. L. Wright. The Cosmic Microwave Background Spectrum from the Full COBE FIRAS Data Set. *ApJ*, 473:576, Dec. 1996. doi:10.1086/178173. → pages 2
- J. Ford, H. Hildebrandt, L. Van Waerbeke, A. Leauthaud, P. Capak, A. Finoguenov, M. Tanaka, M. R. George, and J. Rhodes. Magnification by Galaxy Group Dark Matter Halos. *ApJ*, 754:143, Aug. 2012. doi:10.1088/0004-637X/754/2/143. → pages 15, 28, 32, 33, 35, 46, 66, 67
- J. Ford, H. Hildebrandt, L. Van Waerbeke, T. Erben, C. Laigle, M. Milkeraitis, and C. B. Morrison. Cluster magnification and the mass-richness relation in CFHTLenS. *MNRAS*, 439:3755–3764, Apr. 2014. doi:10.1093/mnras/stu225. → pages 16, 46, 48, 49, 50, 51, 53, 54, 55, 59, 62, 65, 66, 67, 68, 69
- J. Ford, L. Van Waerbeke, M. Milkeraitis, C. Laigle, H. Hildebrandt, T. Erben, C. Heymans, H. Hoekstra, T. Kitching, Y. Mellier, L. Miller, A. Choi, J. Coupon, L. Fu, M. J. Hudson, K. Kuijken, N. Robertson, B. Rowe, T. Schrabback, and M. Velander. CFHTLenS: a weak lensing shear analysis of the 3D-Matched-Filter galaxy clusters. *MNRAS*, 447:1304–1318, Feb. 2015. doi:10.1093/mnras/stu2545. → pages 16
- M. R. George, A. Leauthaud, K. Bundy, A. Finoguenov, J. Tinker, Y.-T. Lin, S. Mei, J.-P. Kneib, H. Aussel, P. S. Behroozi, M. T. Busha, P. Capak, L. Coccato, G. Covone, C. Faure, S. L. Fiorenza, O. Ilbert, E. Le Floch, A. M. Koekemoer, M. Tanaka, R. H. Wechsler, and M. Wolk. Galaxies in X-Ray Groups. I. Robust Membership Assignment and the Impact of Group Environments on Quenching. *ApJ*, 742:125, Dec. 2011. doi:10.1088/0004-637X/742/2/125. → pages 19, 20

- M. R. George, A. Leauthaud, K. Bundy, A. Finoguenov, C.-P. Ma, E. S. Rykoff, J. L. Tinker, R. H. Wechsler, R. Massey, and S. Mei. Galaxies in X-Ray Groups. II. A Weak Lensing Study of Halo Centering. *ApJ*, 757: 2, Sept. 2012. doi:10.1088/0004-637X/757/1/2. → pages 30, 38, 54, 65
- B. R. Gillis and M. J. Hudson. Group-finding with photometric redshifts: the photo-z probability peaks algorithm. *MNRAS*, 410:13–26, Jan. 2011. doi:10.1111/j.1365-2966.2010.17415.x. → pages 30, 46
- M. D. Gladders and H. K. C. Yee. A New Method For Galaxy Cluster Detection. I. The Algorithm. *AJ*, 120: 2148–2162, Oct. 2000. doi:10.1086/301557. → pages 45
- T. Hamana, M. Ouchi, K. Shimasaku, I. Kayo, and Y. Suto. Properties of host haloes of Lyman-break galaxies and Lyman  $\alpha$  emitters from their number densities and angular clustering. *MNRAS*, 347:813–823, Jan. 2004. doi:10.1111/j.1365-2966.2004.07253.x. → pages 35, 36
- S. M. Hansen, T. A. McKay, R. H. Wechsler, J. Annis, E. S. Sheldon, and A. Kimball. Measurement of Galaxy Cluster Sizes, Radial Profiles, and Luminosity Functions from SDSS Photometric Data. *ApJ*, 633:122–137, Nov. 2005. doi:10.1086/444554. → pages 65
- J. Hartlap, P. Simon, and P. Schneider. Why your model parameter confidences might be too optimistic. Unbiased estimation of the inverse covariance matrix. *A&A*, 464:399–404, Mar. 2007. doi:10.1051/0004-6361:20066170. → pages 24, 35
- C. Heymans, L. Van Waerbeke, D. Bacon, J. Berge, G. Bernstein, E. Bertin, S. Bridle, M. L. Brown, D. Clowe, H. Dahle, T. Erben, M. Gray, M. Hetterscheidt, H. Hoekstra, P. Hudelot, M. Jarvis, K. Kuijken, V. Margoniner, R. Massey, Y. Mellier, R. Nakajima, A. Refregier, J. Rhodes, T. Schrabback, and D. Wittman. The Shear Testing Programme - I. Weak lensing analysis of simulated ground-based observations. *MNRAS*, 368:1323–1339, May 2006. doi:10.1111/j.1365-2966.2006.10198.x. → pages 17
- C. Heymans, L. Van Waerbeke, L. Miller, T. Erben, H. Hildebrandt, H. Hoekstra, T. D. Kitching, Y. Mellier, P. Simon, C. Bonnett, J. Coupon, L. Fu, J. Harnois Déraps, M. J. Hudson, M. Kilbinger, K. Kuijken, B. Rowe, T. Schrabback, E. Semboloni, E. van Uitert, S. Vafaei, and M. Velander. CFHTLenS: the Canada-France-Hawaii Telescope Lensing Survey. *MNRAS*, 427:146–166, Nov. 2012. doi:10.1111/j.1365-2966.2012.21952.x. → pages 47
- C. Heymans, E. Grocutt, A. Heavens, M. Kilbinger, T. D. Kitching, F. Simpson, J. Benjamin, T. Erben, H. Hildebrandt, H. Hoekstra, Y. Mellier, L. Miller, L. Van Waerbeke, M. L. Brown, J. Coupon, L. Fu, J. Harnois-Déraps, M. J. Hudson, K. Kuijken, B. Rowe, T. Schrabback, E. Semboloni, S. Vafaei, and M. Velander. CFHTLenS tomographic weak lensing cosmological parameter constraints: Mitigating the impact of intrinsic galaxy alignments. *MNRAS*, 432:2433–2453, July 2013. doi:10.1093/mnras/stt601. → pages 9
- H. Hildebrandt, J. Pielorz, T. Erben, L. van Waerbeke, P. Simon, and P. Capak. CARS: the CFHTLS-Archive-Research Survey. II. Weighing dark matter halos of Lyman-break galaxies at  $z = 3-5$ . *A&A*, 498:725–736, May 2009a. doi:10.1051/0004-6361/200811042. → pages 20, 32, 46
- H. Hildebrandt, L. van Waerbeke, and T. Erben. CARS: The CFHTLS-Archive-Research Survey. III. First detection of cosmic magnification in samples of normal high- $z$  galaxies. *A&A*, 507:683–691, Nov. 2009b. doi:10.1051/0004-6361/200912655. → pages 15, 17, 20, 21, 22, 28, 32, 35, 46
- H. Hildebrandt, A. Muzzin, T. Erben, H. Hoekstra, K. Kuijken, J. Surace, L. van Waerbeke, G. Wilson, and H. K. C. Yee. Lensing Magnification: A Novel Method to Weigh High-redshift Clusters and its Application to SpARCS. *ApJ*, 733:L30, June 2011. doi:10.1088/2041-8205/733/2/L30. → pages 17, 20, 24, 28, 32

- H. Hildebrandt, T. Erben, K. Kuijken, L. van Waerbeke, C. Heymans, J. Coupon, J. Benjamin, C. Bonnett, L. Fu, H. Hoekstra, T. D. Kitching, Y. Mellier, L. Miller, M. Velander, M. J. Hudson, B. T. P. Rowe, T. Schrabback, E. Semboloni, and N. Benítez. CFHTLenS: improving the quality of photometric redshifts with precision photometry. *MNRAS*, 421:2355–2367, Apr. 2012. doi:10.1111/j.1365-2966.2012.20468.x. → pages 28, 35, 46
- H. Hildebrandt, L. van Waerbeke, D. Scott, M. Béthermin, J. Bock, D. Clements, A. Conley, A. Cooray, J. S. Dunlop, S. Eales, T. Erben, D. Farrah, A. Franceschini, J. Glenn, M. Halpern, S. Heinis, R. J. Ivison, G. Marsden, S. J. Oliver, M. J. Page, I. Pérez-Fournon, A. J. Smith, M. Rowan-Robinson, I. Valtchanov, R. F. J. van der Burg, J. D. Vieira, M. Viero, and L. Wang. Inferring the mass of submillimetre galaxies by exploiting their gravitational magnification of background galaxies. *MNRAS*, 429:3230–3237, Mar. 2013. doi:10.1093/mnras/sts585. → pages 16, 28, 35, 46
- G. Hinshaw, D. Larson, E. Komatsu, D. N. Spergel, C. L. Bennett, J. Dunkley, M. R. Nolta, M. Halpern, R. S. Hill, N. Odegard, L. Page, K. M. Smith, J. L. Weiland, B. Gold, N. Jarosik, A. Kogut, M. Limon, S. S. Meyer, G. S. Tucker, E. Wollack, and E. L. Wright. Nine-year Wilkinson Microwave Anisotropy Probe (WMAP) Observations: Cosmological Parameter Results. *ApJS*, 208:19, Oct. 2013. doi:10.1088/0067-0049/208/2/19. → pages 2
- C. M. Hirata and U. Seljak. Intrinsic alignment-lensing interference as a contaminant of cosmic shear. *Phys. Rev. D*, 70(6):063526, Sept. 2004. doi:10.1103/PhysRevD.70.063526. → pages 9
- H. Hoekstra. A comparison of weak-lensing masses and X-ray properties of galaxy clusters. *MNRAS*, 379: 317–330, July 2007. doi:10.1111/j.1365-2966.2007.11951.x. → pages 46
- H. Hoekstra, A. Mahdavi, A. Babul, and C. Bildfell. The Canadian Cluster Comparison Project: weak lensing masses and SZ scaling relations. *MNRAS*, 427:1298–1311, Dec. 2012. doi:10.1111/j.1365-2966.2012.22072.x. → pages 46
- H. Hoekstra, M. Bartelmann, H. Dahle, H. Israel, M. Limousin, and M. Meneghetti. Masses of Galaxy Clusters from Gravitational Lensing. *Space Sci. Rev.*, 177:75–118, Aug. 2013. doi:10.1007/s11214-013-9978-5. → pages 46
- E. Hubble. A Relation between Distance and Radial Velocity among Extra-Galactic Nebulae. *Proceedings of the National Academy of Science*, 15:168–173, Mar. 1929. doi:10.1073/pnas.15.3.168. → pages 2
- E. M. Huff and G. J. Graves. Magnificent Magnification: Exploiting the Other Half of the Lensing Signal. *ApJ*, 780:L16, Jan. 2014. doi:10.1088/2041-8205/780/2/L16. → pages 28, 66
- D. E. Johnston, E. S. Sheldon, R. H. Wechsler, E. Rozo, B. P. Koester, J. A. Frieman, T. A. McKay, A. E. Evrard, M. R. Becker, and J. Annis. Cross-correlation Weak Lensing of SDSS galaxy Clusters II: Cluster Density Profiles and the Mass–Richness Relation. *ArXiv e-prints, astro-ph/0709.1159*, Sept. 2007. → pages 30, 34, 38, 39, 46, 52, 53, 54, 55, 65
- N. Kaiser and G. Squires. Mapping the dark matter with weak gravitational lensing. *ApJ*, 404:441–450, Feb. 1993. doi:10.1086/172297. → pages 14
- M. Kerscher, I. Szapudi, and A. S. Szalay. A Comparison of Estimators for the Two-Point Correlation Function. *ApJ*, 535:L13–L16, May 2000. doi:10.1086/312702. → pages 21
- T. Kitching, S. Balan, G. Bernstein, M. Bethge, S. Bridle, F. Courbin, M. Gentile, A. Heavens, M. Hirsch, R. Hosseini, A. Kiessling, A. Amara, D. Kirk, K. Kuijken, R. Mandelbaum, B. Moghaddam, G. Nurbaeva, S. Paulin-Henriksson, A. Rassat, J. Rhodes, B. Schölkopf, J. Shawe-Taylor, M. Gill, M. Shmakova, A. Taylor, M. Velander, L. van Waerbeke, D. Witherick, D. Wittman, S. Harmeling, C. Heymans, R. Massey, B. Rowe, T. Schrabback, and L. Voigt. Gravitational Lensing Accuracy Testing 2010 (GREAT10) Challenge Handbook. *ArXiv e-prints, astro-ph/1009.0779*, Sept. 2010. → pages 17

- M. G. Kitzbichler and S. D. M. White. The high-redshift galaxy population in hierarchical galaxy formation models. *MNRAS*, 376:2–12, Mar. 2007. doi:10.1111/j.1365-2966.2007.11458.x. → pages 30
- B. P. Koester, T. A. McKay, J. Annis, R. H. Wechsler, A. E. Evrard, E. Rozo, L. Bleem, E. S. Sheldon, and D. Johnston. MaxBCG: A Red-Sequence Galaxy Cluster Finder. *ApJ*, 660:221–238, May 2007. doi:10.1086/512092. → pages 63
- S. D. Landy and A. S. Szalay. Bias and variance of angular correlation functions. *ApJ*, 412:64–71, July 1993. doi:10.1086/172900. → pages 20, 22
- D. Larson, J. Dunkley, G. Hinshaw, E. Komatsu, M. R.olta, C. L. Bennett, B. Gold, M. Halpern, R. S. Hill, N. Jarosik, A. Kogut, M. Limon, S. S. Meyer, N. Odegard, L. Page, K. M. Smith, D. N. Spergel, G. S. Tucker, J. L. Weiland, E. Wollack, and E. L. Wright. Seven-year Wilkinson Microwave Anisotropy Probe (WMAP) Observations: Power Spectra and WMAP-derived Parameters. *ApJS*, 192:16, Feb. 2011. doi:10.1088/0067-0049/192/2/16. → pages 18
- A. Leauthaud, A. Finoguenov, J.-P. Kneib, J. E. Taylor, R. Massey, J. Rhodes, O. Ilbert, K. Bundy, J. Tinker, M. R. George, P. Capak, A. M. Koekemoer, D. E. Johnston, Y.-Y. Zhang, N. Cappelluti, R. S. Ellis, M. Elvis, S. Giodini, C. Heymans, O. Le Fèvre, S. Lilly, H. J. McCracken, Y. Mellier, A. Réfrégier, M. Salvato, N. Scoville, G. Smoot, M. Tanaka, L. Van Waerbeke, and M. Wolk. A Weak Lensing Study of X-ray Groups in the Cosmos Survey: Form and Evolution of the Mass-Luminosity Relation. *ApJ*, 709:97–114, Jan. 2010. doi:10.1088/0004-637X/709/1/97. → pages 19, 46, 53
- R. Lynds and V. Petrosian. Giant Luminous Arcs in Galaxy Clusters. In *Bulletin of the American Astronomical Society*, volume 18 of *Bulletin of the American Astronomical Society*, page 1014, Sept. 1986. → pages 8
- R. Mandelbaum, U. Seljak, R. J. Cool, M. Blanton, C. M. Hirata, and J. Brinkmann. Density profiles of galaxy groups and clusters from SDSS galaxy-galaxy weak lensing. *MNRAS*, 372:758–776, Oct. 2006. doi:10.1111/j.1365-2966.2006.10906.x. → pages 52
- R. Mandelbaum, U. Seljak, and C. M. Hirata. A halo mass–concentration relation from weak lensing. *J. Cosmology Astropart. Phys.*, 8:006, Aug. 2008a. doi:10.1088/1475-7516/2008/08/006. → pages 30, 38
- R. Mandelbaum, U. Seljak, C. M. Hirata, S. Bardelli, M. Bolzonella, A. Bongiorno, M. Carollo, T. Contini, C. E. Cunha, B. Garilli, A. Iovino, P. Kampczyk, J.-P. Kneib, C. Knobel, D. C. Koo, F. Lamareille, O. Le Fèvre, J.-F. Le Borgne, S. J. Lilly, C. Maier, V. Mainieri, M. Mignoli, J. A. Newman, P. A. Oesch, E. Perez-Montero, E. Ricciardelli, M. Scodeggio, J. Silverman, and L. Tasca. Precision photometric redshift calibration for galaxy-galaxy weak lensing. *MNRAS*, 386:781–806, May 2008b. doi:10.1111/j.1365-2966.2008.12947.x. → pages 51
- S. Mao and P. Schneider. Evidence for substructure in lens galaxies? *MNRAS*, 295:587, Apr. 1998. doi:10.1046/j.1365-8711.1998.01319.x. → pages 8
- R. Massey, C. Heymans, J. Bergé, G. Bernstein, S. Bridle, D. Clowe, H. Dahle, R. Ellis, T. Erben, M. Hetterscheidt, F. W. High, C. Hirata, H. Hoekstra, P. Hudelot, M. Jarvis, D. Johnston, K. Kuijken, V. Margoniner, R. Mandelbaum, Y. Mellier, R. Nakajima, S. Paulin-Henriksson, M. Peebles, C. Roat, A. Refregier, J. Rhodes, T. Schrabback, M. Schirmer, U. Seljak, E. Semboloni, and L. van Waerbeke. The Shear Testing Programme 2: Factors affecting high-precision weak-lensing analyses. *MNRAS*, 376:13–38, Mar. 2007a. doi:10.1111/j.1365-2966.2006.11315.x. → pages 17, 47
- R. Massey, J. Rhodes, R. Ellis, N. Scoville, A. Leauthaud, A. Finoguenov, P. Capak, D. Bacon, H. Aussel, J.-P. Kneib, A. Koekemoer, H. McCracken, B. Mobasher, S. Pires, A. Refregier, S. Sasaki, J.-L. Starck, Y. Taniguchi, A. Taylor, and J. Taylor. Dark matter maps reveal cosmic scaffolding. *Nature*, 445:286–290, Jan. 2007b. doi:10.1038/nature05497. → pages 27

- A. Mazure, C. Adami, M. Pierre, O. Le Fèvre, S. Arnouts, P. A. Duc, O. Ilbert, V. Lebrun, B. Meneux, F. Pacaud, J. Surdej, and I. Valtchanov. Structure detection in the D1 CFHTLS deep field using accurate photometric redshifts: a benchmark. *A&A*, 467:49–62, May 2007. doi:10.1051/0004-6361:20066379. → pages 64
- B. Ménard, T. Hamana, M. Bartelmann, and N. Yoshida. Improving the accuracy of cosmic magnification statistics. *A&A*, 403:817–828, June 2003. doi:10.1051/0004-6361:20030406. → pages 22, 32
- B. Ménard, R. Scranton, M. Fukugita, and G. Richards. Measuring the galaxy-mass and galaxy-dust correlations through magnification and reddening. *MNRAS*, 405:1025–1039, June 2010. doi:10.1111/j.1365-2966.2010.16486.x. → pages 26
- J. Merten, M. Meneghetti, M. Postman, K. Umetsu, A. Zitrin, E. Medezinski, M. Nonino, A. Koekemoer, P. Melchior, D. Gruen, L. A. Moustakas, M. Bartelmann, O. Host, M. Donahue, D. Coe, A. Molino, S. Jouvel, A. Monna, S. Seitz, N. Czakon, D. Lemze, J. Sayers, I. Balestra, P. Rosati, N. Benítez, A. Biviano, R. Bouwens, L. Bradley, T. Broadhurst, M. Carrasco, H. Ford, C. Grillo, L. Infante, D. Kelson, O. Lahav, R. Massey, J. Moustakas, E. Rasia, J. Rhodes, J. Vega, and W. Zheng. CLASH: The Concentration-Mass Relation of Galaxy Clusters. *ArXiv e-prints, astro-ph/1404.1376*, Apr. 2014. → pages 67
- M. Milkeraitis. *Optical galaxy cluster detection and weak lensing derived galaxy cluster mass functions: the development of a new algorithm and its application to the Millenium Simulation, CFHTLS-Deep, and CFHTLS-Wide surveys*. PhD thesis, University of British Columbia, 2011. → pages 31, 48, 49
- M. Milkeraitis, L. van Waerbeke, C. Heymans, H. Hildebrandt, J. P. Dietrich, and T. Erben. 3D-Matched-Filter galaxy cluster finder - I. Selection functions and CFHTLS Deep clusters. *MNRAS*, 406:673–688, July 2010. doi:10.1111/j.1365-2966.2010.16720.x. → pages 27, 28, 29, 30, 33, 46, 47, 48, 53
- L. Miller, C. Heymans, T. D. Kitching, L. van Waerbeke, T. Erben, H. Hildebrandt, H. Hoekstra, Y. Mellier, B. T. P. Rowe, J. Coupon, J. P. Dietrich, L. Fu, J. Harnois-Déraps, M. J. Hudson, M. Kilbinger, K. Kuijken, T. Schrabback, E. Semboloni, S. Vafaei, and M. Velander. Bayesian galaxy shape measurement for weak lensing surveys - III. Application to the Canada-France-Hawaii Telescope Lensing Survey. *MNRAS*, 429: 2858–2880, Mar. 2013. doi:10.1093/mnras/sts454. → pages 47, 51
- H. J. Mo and S. D. M. White. An analytic model for the spatial clustering of dark matter haloes. *MNRAS*, 282: 347–361, Sept. 1996. → pages 55
- C. B. Morrison, R. Scranton, B. Ménard, S. J. Schmidt, J. A. Tyson, R. Ryan, A. Choi, and D. M. Wittman. Tomographic magnification of Lyman-break galaxies in the Deep Lens Survey. *MNRAS*, 426:2489–2499, Nov. 2012. doi:10.1111/j.1365-2966.2012.21826.x. → pages 28, 32, 46
- R. Narayan. Gravitational lensing and quasar-galaxy correlations. *ApJ*, 339:L53–L56, Apr. 1989. doi:10.1086/185418. → pages 13, 14, 18, 19, 32
- R. Narayan and M. Bartelmann. Lectures on Gravitational Lensing. *ArXiv Astrophysics e-prints*, June 1996. → pages 9, 12
- J. F. Navarro, C. S. Frenk, and S. D. M. White. A Universal Density Profile from Hierarchical Clustering. *ApJ*, 490:493, Dec. 1997. doi:10.1086/304888. → pages 23, 33, 52
- J. A. Newman. Calibrating Redshift Distributions beyond Spectroscopic Limits with Cross-Correlations. *ApJ*, 684:88–101, Sept. 2008. doi:10.1086/589982. → pages 35
- M. Oguri. A cluster finding algorithm based on the multiband identification of red sequence galaxies. *MNRAS*, 444:147–161, Oct. 2014. doi:10.1093/mnras/stu1446. → pages 46, 54

- M. Ouchi, K. Shimasaku, S. Okamura, H. Furusawa, N. Kashikawa, K. Ota, M. Doi, M. Hamabe, M. Kimura, Y. Komiyama, M. Miyazaki, S. Miyazaki, F. Nakata, M. Sekiguchi, M. Yagi, and N. Yasuda. Subaru Deep Survey. V. A Census of Lyman Break Galaxies at  $z=4$  and 5 in the Subaru Deep Fields: Photometric Properties. *ApJ*, 611:660–684, Aug. 2004. doi:10.1086/422207. → pages 20
- B. Paczynski. Gravitational Microlensing in the Local Group. *ARA&A*, 34:419–460, 1996. doi:10.1146/annurev.astro.34.1.419. → pages 9
- A. A. Penzias and R. W. Wilson. A Measurement of Excess Antenna Temperature at 4080 Mc/s. *ApJ*, 142: 419–421, July 1965. doi:10.1086/148307. → pages 2
- S. Perlmutter, G. Aldering, G. Goldhaber, R. A. Knop, P. Nugent, P. G. Castro, S. Deustua, S. Fabbro, A. Goobar, D. E. Groom, I. M. Hook, A. G. Kim, M. Y. Kim, J. C. Lee, N. J. Nunes, R. Pain, C. R. Pennypacker, R. Quimby, C. Lidman, R. S. Ellis, M. Irwin, R. G. McMahon, P. Ruiz-Lapuente, N. Walton, B. Schaefer, B. J. Boyle, A. V. Filippenko, T. Matheson, A. S. Fruchter, N. Panagia, H. J. M. Newberg, W. J. Couch, and T. S. C. Project. Measurements of  $\Omega$  and  $\Lambda$  from 42 High-Redshift Supernovae. *ApJ*, 517: 565–586, June 1999. doi:10.1086/307221. → pages 4
- Planck Collaboration, P. A. R. Ade, N. Aghanim, C. Armitage-Caplan, M. Arnaud, M. Ashdown, F. Atrio-Barandela, J. Aumont, C. Baccigalupi, A. J. Banday, and et al. Planck 2013 results. XVI. Cosmological parameters. *A&A*, 571:A16, Nov. 2014. doi:10.1051/0004-6361/201321591. → pages 2, 4, 5, 6
- M. Postman, L. M. Lubin, J. E. Gunn, J. B. Oke, J. G. Hoessel, D. P. Schneider, and J. A. Christensen. The Palomar Distant Clusters Survey. I. The Cluster Catalog. *AJ*, 111:615, Feb. 1996. doi:10.1086/117811. → pages 45, 47
- F. Prada, A. A. Klypin, A. J. Cuesta, J. E. Betancort-Rijo, and J. Primack. Halo concentrations in the standard  $\Lambda$  cold dark matter cosmology. *MNRAS*, 423:3018–3030, July 2012. doi:10.1111/j.1365-2966.2012.21007.x. → pages 33, 55, 66
- A. G. Riess, A. V. Filippenko, P. Challis, A. Clocchiatti, A. Diercks, P. M. Garnavich, R. L. Gilliland, C. J. Hogan, S. Jha, R. P. Kirshner, B. Leibundgut, M. M. Phillips, D. Reiss, B. P. Schmidt, R. A. Schommer, R. C. Smith, J. Spyromilio, C. Stubbs, N. B. Suntzeff, and J. Tonry. Observational Evidence from Supernovae for an Accelerating Universe and a Cosmological Constant. *AJ*, 116:1009–1038, Sept. 1998. doi:10.1086/300499. → pages 4
- E. Rozo and F. Schmidt. Weak Lensing Mass Calibration with Shear and Magnification. *ArXiv e-prints*, astro-ph/1009.5735, Sept. 2010. → pages 15, 18, 25
- E. Rozo, E. S. Rykoff, A. Evrard, M. Becker, T. McKay, R. H. Wechsler, B. P. Koester, J. Hao, S. Hansen, E. Sheldon, D. Johnston, J. Annis, and J. Frieman. Constraining the Scatter in the Mass-richness Relation of maxBCG Clusters with Weak Lensing and X-ray Data. *ApJ*, 699:768–781, July 2009a. doi:10.1088/0004-637X/699/1/768. → pages 61
- E. Rozo, E. S. Rykoff, B. P. Koester, T. McKay, J. Hao, A. Evrard, R. H. Wechsler, S. Hansen, E. Sheldon, D. Johnston, M. Becker, J. Annis, L. Bleem, and R. Scranton. Improvement of the Richness Estimates of maxBCG Clusters. *ApJ*, 703:601–613, Sept. 2009b. doi:10.1088/0004-637X/703/1/601. → pages 65
- B. Ryden. *Introduction to cosmology*. 2003. → pages 1, 2, 3, 4, 5, 6, 7, 13
- E. S. Rykoff, E. Rozo, M. T. Busha, C. E. Cunha, A. Finoguenov, A. Evrard, J. Hao, B. P. Koester, A. Leauthaud, B. Nord, M. Pierre, R. Reddick, T. Sadibekova, E. S. Sheldon, and R. H. Wechsler. redMaPPer. I. Algorithm and SDSS DR8 Catalog. *ApJ*, 785:104, Apr. 2014. doi:10.1088/0004-637X/785/2/104. → pages 45

- C. Sagan. *Cosmos*. 1980. → pages 1
- M. Sawicki and D. Thompson. Keck Deep Fields. II. The Ultraviolet Galaxy Luminosity Function at  $z \sim 4$ , 3, and 2. *ApJ*, 642:653–672, May 2006. doi:10.1086/500999. → pages 22, 23
- P. Schechter. An analytic expression for the luminosity function for galaxies. *ApJ*, 203:297–306, Jan. 1976. doi:10.1086/154079. → pages 22, 33
- F. Schmidt, A. Leauthaud, R. Massey, J. Rhodes, M. R. George, A. M. Koekemoer, A. Finoguenov, and M. Tanaka. A Detection of Weak-lensing Magnification Using Galaxy Sizes and Magnitudes. *ApJ*, 744:L22, Jan. 2012. doi:10.1088/2041-8205/744/2/L22. → pages 18, 24, 28
- P. Schneider. Part 1: Introduction to gravitational lensing and cosmology. In G. Meylan, P. Jetzer, P. North, P. Schneider, C. S. Kochanek, and J. Wambsganss, editors, *Saas-Fee Advanced Course 33: Gravitational Lensing: Strong, Weak and Micro*, pages 1–89, 2006a. → pages 10, 12
- P. Schneider. Part 3: Weak gravitational lensing. In G. Meylan, P. Jetzer, P. North, P. Schneider, C. S. Kochanek, and J. Wambsganss, editors, *Saas-Fee Advanced Course 33: Gravitational Lensing: Strong, Weak and Micro*, pages 269–451, 2006b. → pages 7, 11, 12, 13
- P. Schneider, L. King, and T. Erben. Cluster mass profiles from weak lensing: constraints from shear and magnification information. *A&A*, 353:41–56, Jan. 2000. → pages 15
- R. Scranton, B. Ménard, G. T. Richards, R. C. Nichol, A. D. Myers, B. Jain, A. Gray, M. Bartelmann, R. J. Brunner, A. J. Connolly, J. E. Gunn, R. K. Sheth, N. A. Bahcall, J. Brinkman, J. Loveday, D. P. Schneider, A. Thakar, and D. G. York. Detection of Cosmic Magnification with the Sloan Digital Sky Survey. *ApJ*, 633: 589–602, Nov. 2005. doi:10.1086/431358. → pages 14, 15, 17, 19, 22, 23, 28, 46
- N. Sehgal, G. Addison, N. Battaglia, E. S. Battistelli, J. R. Bond, S. Das, M. J. Devlin, J. Dunkley, R. Dünner, M. Gralla, A. Hajian, M. Halpern, M. Hasselfield, M. Hilton, A. D. Hincks, R. Hlozek, J. P. Hughes, A. Kosowsky, Y.-T. Lin, T. Louis, T. A. Marriage, D. Marsden, F. Menanteau, K. Moodley, M. D. Niemack, L. A. Page, B. Partridge, E. D. Reese, B. D. Sherwin, J. Sievers, C. Sifón, D. N. Spergel, S. T. Staggs, D. S. Swetz, E. R. Switzer, and E. Wollack. The Atacama Cosmology Telescope: Relation between Galaxy Cluster Optical Richness and Sunyaev-Zel’dovich Effect. *ApJ*, 767:38, Apr. 2013. doi:10.1088/0004-637X/767/1/38. → pages 54
- U. Seljak and M. S. Warren. Large-scale bias and stochasticity of haloes and dark matter. *MNRAS*, 355: 129–136, Nov. 2004. doi:10.1111/j.1365-2966.2004.08297.x. → pages 34, 36, 55
- H. Shan, J.-P. Kneib, C. Tao, Z. Fan, M. Jauzac, M. Limousin, R. Massey, J. Rhodes, K. Thanjavur, and H. J. McCracken. Weak Lensing Measurement of Galaxy Clusters in the CFHTLS-Wide Survey. *ApJ*, 748:56, Mar. 2012. doi:10.1088/0004-637X/748/1/56. → pages 64
- R. K. Sheth and G. Tormen. Large-scale bias and the peak background split. *MNRAS*, 308:119–126, Sept. 1999. doi:10.1046/j.1365-8711.1999.02692.x. → pages 55
- M. Simet and R. Mandelbaum. Background sky obscuration by cluster galaxies as a source of systematic error for weak lensing. *ArXiv e-prints, astro-ph/1406.4908*, June 2014. → pages 68
- G. Soucail, B. Fort, Y. Mellier, and J. P. Picat. A blue ring-like structure, in the center of the A 370 cluster of galaxies. *A&A*, 172:L14–L16, Jan. 1987. → pages 8
- G. Soucail, Y. Mellier, B. Fort, G. Mathez, and M. Cailloux. The giant arc in A 370 - Spectroscopic evidence for gravitational lensing from a source at  $Z = 0.724$ . *A&A*, 191:L19–L21, Feb. 1988. → pages 8



- V. Springel, S. D. M. White, A. Jenkins, C. S. Frenk, N. Yoshida, L. Gao, J. Navarro, R. Thacker, D. Croton, J. Helly, J. A. Peacock, S. Cole, P. Thomas, H. Couchman, A. Evrard, J. Colberg, and F. Pearce. Simulations of the formation, evolution and clustering of galaxies and quasars. *Nature*, 435:629–636, June 2005. doi:10.1038/nature03597. → pages 30
- C. C. Steidel, K. L. Adelberger, M. Dickinson, M. Giavalisco, and M. Pettini. Lyman Break Galaxies at  $z \sim 3$  and Beyond. *ArXiv e-prints, astro-ph/9812167*, Dec. 1998. → pages 32
- T. Sumi, D. P. Bennett, I. A. Bond, F. Abe, C. S. Botzler, A. Fukui, K. Furusawa, Y. Itow, C. H. Ling, K. Masuda, Y. Matsubara, Y. Muraki, K. Ohnishi, N. Rattenbury, T. Saito, D. J. Sullivan, D. Suzuki, W. L. Sweatman, P. J. Tristram, K. Wada, P. C. M. Yock, and T. MOA Collaboratoin. The Microlensing Event Rate and Optical Depth toward the Galactic Bulge from MOA-II. *ApJ*, 778:150, Dec. 2013. doi:10.1088/0004-637X/778/2/150. → pages 9
- M. Takada. Subaru Hyper Suprime-Cam Project. In N. Kawai and S. Nagataki, editors, *American Institute of Physics Conference Series*, volume 1279 of *American Institute of Physics Conference Series*, pages 120–127, Oct. 2010. doi:10.1063/1.3509247. → pages 69
- The Dark Energy Survey Collaboration. The Dark Energy Survey. *ArXiv e-prints, astro-ph/0510346*, Oct. 2005. → pages 69
- J. L. Tinker, B. E. Robertson, A. V. Kravtsov, A. Klypin, M. S. Warren, G. Yepes, and S. Gottlöber. The Large-scale Bias of Dark Matter Halos: Numerical Calibration and Model Tests. *ApJ*, 724:878–886, Dec. 2010. doi:10.1088/0004-637X/724/2/878. → pages 55
- J. A. Tyson, F. Valdes, J. F. Jarvis, and A. P. Mills, Jr. Galaxy mass distribution from gravitational light deflection. *ApJ*, 281:L59–L62, June 1984. doi:10.1086/184285. → pages 14
- K. Umetsu. Model-free Multi-probe Lensing Reconstruction of Cluster Mass Profiles. *ApJ*, 769:13, May 2013. doi:10.1088/0004-637X/769/1/13. → pages 66
- K. Umetsu, T. Broadhurst, A. Zitrin, E. Medezinski, and L.-Y. Hsu. Cluster Mass Profiles from a Bayesian Analysis of Weak-lensing Distortion and Magnification Measurements: Applications to Subaru Data. *ApJ*, 729:127, Mar. 2011. doi:10.1088/0004-637X/729/2/127. → pages 15, 17, 18, 46, 66
- K. Umetsu, E. Medezinski, M. Nonino, J. Merten, M. Postman, M. Meneghetti, M. Donahue, N. Czakon, A. Molino, S. Seitz, D. Gruen, D. Lemze, I. Balestra, N. Benítez, A. Biviano, T. Broadhurst, H. Ford, C. Grillo, A. Koekemoer, P. Melchior, A. Mercurio, J. Moustakas, P. Rosati, and A. Zitrin. CLASH: Weak-lensing Shear-and-magnification Analysis of 20 Galaxy Clusters. *ApJ*, 795:163, Nov. 2014. doi:10.1088/0004-637X/795/2/163. → pages 46, 66
- S. van den Bergh. The Early History of Dark Matter. *PASP*, 111:657–660, June 1999. doi:10.1086/316369. → pages 3
- R. F. J. van der Burg, H. Hildebrandt, and T. Erben. The UV galaxy luminosity function at  $z = 3$ –5 from the CFHT Legacy Survey Deep fields. *A&A*, 523:A74, Nov. 2010. doi:10.1051/0004-6361/200913812. → pages 22, 23, 33
- E. van Uitert. *Weak gravitational lensing in the red-sequence cluster survey 2 (RCS2)*. PhD thesis, Leiden University, 2012. → pages 63
- L. van Waerbeke. Shear and magnification: cosmic complementarity. *MNRAS*, 401:2093–2100, Jan. 2010. doi:10.1111/j.1365-2966.2009.15809.x. → pages 14, 15, 18, 26
- L. Van Waerbeke, H. Hildebrandt, J. Ford, and M. Milkeraitis. Magnification as a Probe of Dark Matter Halos at High Redshifts. *ApJ*, 723:L13–L16, Nov. 2010. doi:10.1088/2041-8205/723/1/L13. → pages 17, 28

- L. Van Waerbeke, J. Benjamin, T. Erben, C. Heymans, H. Hildebrandt, H. Hoekstra, T. D. Kitching, Y. Mellier, L. Miller, J. Coupon, J. Harnois-Déraps, L. Fu, M. Hudson, M. Kilbinger, K. Kuijken, B. Rowe, T. Schrabback, E. Semboloni, S. Vafaei, E. van Uitert, and M. Velander. CFHTLenS: mapping the large-scale structure with gravitational lensing. *MNRAS*, 433:3373–3388, Aug. 2013. doi:10.1093/mnras/stt971. → pages 27
- M. Velander, E. van Uitert, H. Hoekstra, J. Coupon, T. Erben, C. Heymans, H. Hildebrandt, T. D. Kitching, Y. Mellier, L. Miller, L. Van Waerbeke, C. Bonnett, L. Fu, S. Giodini, M. J. Hudson, K. Kuijken, B. Rowe, T. Schrabback, and E. Semboloni. CFHTLenS: the relation between galaxy dark matter haloes and baryons from weak gravitational lensing. *MNRAS*, 437:2111–2136, Jan. 2014. doi:10.1093/mnras/stt2013. → pages 50, 51, 61
- G. M. Voit. Tracing cosmic evolution with clusters of galaxies. *Reviews of Modern Physics*, 77:207–258, Apr. 2005. doi:10.1103/RevModPhys.77.207. → pages 45
- D. Walsh, R. F. Carswell, and R. J. Weymann. 0957 + 561 A, B - Twin quasistellar objects or gravitational lens. *Nature*, 279:381–384, May 1979. doi:10.1038/279381a0. → pages 8
- Z. L. Wen, J. L. Han, and F. S. Liu. Galaxy Clusters Identified from the SDSS DR6 and Their Properties. *ApJS*, 183:197–213, Aug. 2009. doi:10.1088/0067-0049/183/2/197. → pages 64
- Z. L. Wen, J. L. Han, and F. S. Liu. A Catalog of 132,684 Clusters of Galaxies Identified from Sloan Digital Sky Survey III. *ApJS*, 199:34, Apr. 2012. doi:10.1088/0067-0049/199/2/34. → pages 64
- C. O. Wright and T. G. Brainerd. Gravitational Lensing by NFW Halos. *ApJ*, 534:34–40, May 2000. doi:10.1086/308744. → pages 9, 12, 34, 52
- L. Wyrzykowski, J. Skowron, S. Kozłowski, A. Udalski, M. K. Szymański, M. Kubiak, G. Pietrzyński, I. Soszyński, O. Szewczyk, K. Ulaczyk, R. Poleski, and P. Tisserand. The OGLE view of microlensing towards the Magellanic Clouds - IV. OGLE-III SMC data and final conclusions on MACHOs. *MNRAS*, 416:2949–2961, Oct. 2011. doi:10.1111/j.1365-2966.2011.19243.x. → pages 9
- X. Yang, H. J. Mo, F. C. van den Bosch, Y. P. Jing, S. M. Weinmann, and M. Meneghetti. Weak lensing by galaxies in groups and clusters - I. Theoretical expectations. *MNRAS*, 373:1159–1172, Dec. 2006. doi:10.1111/j.1365-2966.2006.11091.x. → pages 34, 54
- I. Zehavi, Z. Zheng, D. H. Weinberg, M. R. Blanton, N. A. Bahcall, A. A. Berlind, J. Brinkmann, J. A. Frieman, J. E. Gunn, R. H. Lupton, R. C. Nichol, W. J. Percival, D. P. Schneider, R. A. Skibba, M. A. Strauss, M. Tegmark, and D. G. York. Galaxy Clustering in the Completed SDSS Redshift Survey: The Dependence on Color and Luminosity. *ApJ*, 736:59, July 2011. doi:10.1088/0004-637X/736/1/59. → pages 36
- F. Zwicky. Die Rotverschiebung von extragalaktischen Nebeln. *Helvetica Physica Acta*, 6:110–127, 1933. → pages 3
- F. Zwicky. On the Masses of Nebulae and of Clusters of Nebulae. *ApJ*, 86:217, Oct. 1937. doi:10.1086/143864. → pages 3

## **Appendix A**

# **Supporting Materials**

This would be any supporting material not central to the dissertation. For example:

- Authorizations from Research Ethics Boards for the various experiments conducted during the course of research.
- Copies of questionnaires and survey instruments.